Materials Development and Architecture Engineering for High Efficiency Organic Solar Cells

by

Bing Cao

A thesis submitted in partial fulfillment of the requirements for the degree of

Doctor of Philosophy

Department of Chemistry

University of Alberta

Abstract

The growing population and world economy has led to the rise in both the demand for energy and its production. Use of fossil fuels and abusive mining contribute to environmental pollution and the depletion of natural resources. In order to meet future energy demands and control CO_2 emissions, low-carbon, renewable energy sources must be developed. Solar energy is of particular interest since just one-hour of sunlight could power the entire world for a year. An attractive method for harvesting solar energy is the use of photovoltaic devices, which directly convert solar energy into electricity. Organic semiconductor solar cells have emerged as a promising candidate because of their low-cost, lightweight, freedom in shape, ease of processing, and low environmental impact. The focus of this dissertation is to investigate mechanisms limiting polymer solar cell performance and ways to improve device efficiency. These approaches include developing photoactive and interfacial materials, as well as interface and device engineering.

First, two isostructural low-band-gap conjugated small molecules were synthesized with one-atom substitution, S, and Se for the use as photon-absorbing

material in organic solar cells (OSCs). The two molecules were based on the benzo[1,2-b:4,5-b′]dithiophene electron-rich unit and the sulfur-containing electron-deficient benzothiadiazole (BT) unit following the donor-acceptor concept. The investigation into the photovoltaic properties showed that one-atom substitution could engender substantial differences in the solubility, which then influenced the crystal orientations of the small molecules within this thin layer, resulting a higher power conversion efficiency (2.6%) for the Se-containing molecules. Second, we introduced interfacial layers to improve the OSC performance. A thin, low-band-gap polymer interfacial layer called PBDTTPD-COOH was synthesized and applied on the commonly used ITO/PEDOT:PSS electrode to modify the interface between ITO/PEDOT:PSS and bulk heterojunction (BHJ). The use of this modifier layer improved the polymer conversion efficiency for the PCDTBT- and PBDTTPD-based solar cell from 6.2% to 7.0% and from 6.3% to 7.3%, respectively, but had little effect on the PTB7-based solar cells. The investigation on the energy level alignment, phase segregation, and the local composition of the BHJ suggested that phase separation near the interface caused by the surface energy change was the key to efficiency improvement. A guideline for matching an interfacial layer and a BHJ with regard to the energy level pinning and phase segregation was proposed. Finally, we carried out an overall device engineering in novel structure to improve the charge extraction in solar cell devices. A nanostructured ITO electrode was deposited and used in a high-hole-mobility polymer:PCBM solar cell to achieve balanced charge extraction and collection. The ITO nanotree electrodes with a

range of heights were fabricated into solar cells, and photovoltaic performance was characterized. The optimized efficiency was obtained at ITO nanoelectrode height of 75 nm. Investigation on the effect of the ITO indicated that shortening the electron extraction pathway, altering the potential distribution throughout the BHJ, and trapping light for photon harvesting contributed simultaneously to affect the photovoltaic performance.

Preface

Chapter 1 provides an overview of emerging solar cell technologies, with an emphasis on organic solar cells.

Chapter 2 is based on the publication, 'Donor–Acceptor Small Molecules for Organic Photovoltaics: Single-Atom Substitution (Se or S)', in *ACS Applied Materials & Interfaces*, **2015**, volume 7, issue 15, pages 8188-8199, with authors Xiaoming He, Bing Cao, Tate C. Hauger, Minkyu Kang, Sergey Gusarov, Erik J. Luber, and Jillian M. Buriak. Please note that Dr. Xiaoming He and myself are co-first authors. I performed the fabrication of the solar cells, data collection and analysis. Dr. Xiaoming He synthesized the molecules, and Minkyu Kang participated in part of the synthesis. Dr. Sergey Gusarov carried out the theoretical analysis for the electronic structure of the molecules. Tate Hauger assisted with AFM imaging. Dr. Erik Luber helped with the data analysis and manuscript writing, and Dr. Jillian Buriak was the supervisor and assisted with manuscript writing.

Chapter 3 is based on the publication, 'Role of Interfacial Layers in Organic

Solar Cells: Energy Level Pinning versus Phase Segregation', in *ACS Appl. Mater. Interfaces*, **2016**, volume 8, issue 28, pages 18238–18248, with author Bing Cao, Xiaoming He, Christopher Fetterly, Brian C. Olsen, Erik J. Luber and Jillian M. Buriak. I performed characterization of the polymer and solar cell device fabrication and testing, and wrote the manuscript. Dr. Xiaoming He synthesized the PBDTTPD-COOH polymer. Chris Fetterly and Dr. Erik Luber helped with the surface energy measurement and calculations. Dr. Erik Luber also helped with the data analysis and manuscript writing. Brian Olsen wrote the code to generate the average-shifted-histogram plots, and he drew the ToC figures. Dr. Jillian Buriak was the supervisor and assisted with manuscript writing.

Chapter 4 was also written as an article with co-authors. I performed the solar cell device fabrication, data collection, analysis, and writing. The GLAD nanotree electrodes were grown in Dr. Michael Brett group by several people including Dr. Allan Beaudry, Mr. Al Lalany, and Dr. Jason Sorge. Dr. Afsha, Mr. Kaveh Ahadi, and Dr. Triratna Muneshwar Amir from Dr. Ken Cadien's group performed the atomic layer deposition. Peng Li facilitated the TEM and EDX imaging. Dr. Xiaoming He and Dr. Hosnay Mobrok synthesized the polymer. Dr. Erik Luber assisted with the manuscript writing.

Chapter 5 summarizes the findings of this thesis and proposes future directions for the ongoing development of this research.

Acknowledgements

First of all, I would like to express my deepest sense of gratitude to my supervisor, Dr. Jillian M. Buriak, who has continuously offered her support, encouragement, and guidance over the past five years. She has also influenced me, consciously and unconsciously, to keep the natural passion and self-motivated attitude to pursue a career in science. She set a model for me of how a female scientist could change the world.

I would like to thank my committee members, Dr. Richard McCreery, Dr. Steven Bergens, Dr. Xihua Wang, and Dr. Eric Rivard for their advice and guidance throughout my degree, and Dr. Ye Tao for agreeing to be my external examiner. I am also grateful to my collaborators for their generous help and support to my projects, including Dr. Ken Cadien from Department of Chemical and Materials Engineering, Dr. Michael Brett from Department of Electrical and Computer Engineering at the University of Alberta, and Dr. Mario Leclerc from Department of Chemistry at Université Laval.

I thank my fellow lab mates in Buriak group for their assistance and friendship. In particular, I would like to thank Dr. Erik Luber, Dr. Xiaoming He, Dr. Hosnay Mobrok, Dr. Brian Wolfolk, Mr. Tate Hauger and Mr. Brian Olsen for generously offering specific

knowledge that assisted with this dissertation. I would also like to thank my other labmates including Dr. Jeremy Bau, Mr. Fenglin Liu, Sharon Chen, Dr. Jeffrey Murphy, Mr. Cong Jin, Ms. Jennifer Ozdoba (Bruce), Ms. Kelli Luber, Dr. Gang He, Mr. Chris Fetterly, Dr. Binbin Yu, Ms. Minjia Hu, Mr. Hezhen Xie, Mr. Chengcheng Rao for making my experience in graduate school exciting and full of fun.

Fellow students from collaborators' labs contributed to various projects related to this dissertation: Dr. Jason Sorge, Dr. Al Lalany, and Dr. Allan Beaudry, Mr. Amir Afsha, Mr. Kaveh Ahadi, and Dr. Triratna Muneshwar. I also obtained enormous help from the staff of the Department of Chemistry, NINT, and the University of Alberta NanoFab including Dr. Anqiang He, Dr. Peng Li, and Dr. Shihong Xu.

Finally, I would also like to thank my family for the support through my entire life and in particular, I must acknowledge my fiancé, Jing Li, without whose love, encouragement, and editing assistance I would not have finished this thesis.

Contents

List of Figures

List of Tables

List of Abbreviations

Abbreviation	Meaning
AFM	Atomic force microscopy
ALD	Atomic layer deposition
ASH	Average shifted histogram
BCP	Bathocuproine
BHJ	Bulk heterojunction
BIPV	Building integrated photovoltaic
CB	Chlorobeneze
CIGS	$Cu(In,Ga)(Se,S)_2$
CuPc	Copper phthalocyanine
D-A	Donor-acceptor
DFT	Density functional theory
DIO	1,8-diiodooctane
DMF	Dimethylformamide
DMSO	Dimethyl sulfoxide
DPP	Diketopyrrolopyrrole
DSC	Differential scanning calorimetry
DSSC	Dye sensitized solar cell
FF	Fill factor
FIB	Focused ion beam
GIXRD	Grazing incidence X-ray diffraction
GIXS	Grazing incidence X-ray scattering
GLAD	Glancing angle deposition
GPC	Gel permeation chromatography

GT	Gigatonnes
HOMO	Heighest occupied molecular orbital
HRMS	High-resolution mass spectroscopy
IPA	Isopropyl alcohol
ITO	Indium tin oxide
J_{SC}	Short circuit current density
J-V	Current density - voltage
LUMO	Lowest unoccupied molecular orbital
MEH-PPV	Poly[2-methoxy-5-(2'-ethylhexyloxy)]-1,4-phenylenevinylene
NMR	Nuclear magnetic resonance
NT	Nanotree
o-DCB	ortho-dichlorobezene
OPV	Organic photovoltaic
OSC	Organic solar cell
P3HT	Poly(3-hexylthiophene)
PBDTTPD	Poly2,6′-4,8-di(5-ethylhexylthienyl)benzo[1,2-b;3,4-b]dithiophene-alt-5-dibutyloctyl-3,6-bis(5-bromothiophen-2-yl)pyrrolo[3,4-c]pyrrole-1,4-dione
PCDTBT	Poly[N-9′-heptadecanyl-2,7-carbazole-alt-5,5-(4′,7′-di-2-thienyl-2′,1′,3′-benzothiadiazole)]
PCE	Power conversion efficiency
PEDOT:PSS	Poly(3,4-ethylenedioxythiophene):poly(*p*-styrenesulfonate)
PFN	Poly [(9,9-bis(3'-(N,N-dimethylamino)propyl)-2,7-fluorene)-alt-2,7-(9,9–dioctylfluorene)]

PTB7	Poly[(4,8-bis-(2-ethylhexyloxy)-benzo(1,2-b:4,5-b′)dithiophene)-2,6-diyl-alt-(4-(2-ethylhexyl)-3-fluorothieno[3,4-b]thiophene-)-2-carboxylate-2-6-diyl)]
SAM	Self-assembled monolayer
SCLC	Space charge limited current
SCLP	Space-charge-limited photocurrent
SEM	Scanning electron microscopy
TALD	Thermal atomic layer deposition
TEM	Transmission electron microscopy
TGA	Thermogravimetric analysis
THF	Tetrahydrofuran
ToF-SIMS	Time of flight secondary ion mass spectroscopy
UPS	Ultraviolet photoelectron spectroscopy
UV-vis	Ultraviolet and visible
V_{OC}	Open circuit voltage
XRD	X-ray diffraction

1

Introduction to Organic Solar Cells

1.1 Overview

The goal of this thesis is to investigate approaches to improve organic solar cell (OSC) performance. Three research projects based on photoactive material synthesis, interfacial material synthesis and interface engineering, and novel solar cell architecture engineering are reported.

Chapter 1 provides a brief introduction of organic solar cells research, including the history, operation principles, and key components that determine solar cell performance. This introductory chapter is followed by three chapters

that individually discuss photoactive material development, interfacial layer engineering, and novel solar cell structure design. Chapter 2 provides a synthetic approach for conjugated small molecules for use as photoactive material in organic solar cells . Chapter 3 describes an interfacial material that is used between the photoactive layer and the electrode. Chapter 4 investigates electrode design, interface engineering, and device engineering methods to build a novel structured solar cell using a nanostructured ITO electrode and a high-hole-mobility polymer. The comprehensive effect of the high-surface-area electrode and the high-hole-mobility polymer was also investigated. Finally, Chapter 5 summarizes the findings of this thesis and proposes future directions for the ongoing development of this research.

1.2 Why Organic Solar Cells?

1.2.1 Clean Energy Demand

With the growth in world population and economy, world energy demand has increased. According to the International Energy Agency's 2015 Energy and Climate Report, the world's total energy demands are predicted to reach 16000 Mtoe (million tonne of oil equivalent) in 2030,[19] as shown in Figure 1.1. In 2013, fossil fuels, including gas, coal, and oil, were the main sources of energy, accounting for more than 80% of total primary energy demand, and will continue to account for more than 75% of the total energy demand through 2030. These fossil fuels

contribute tremendous amount of CO_2 by combustion. According to the report, the total volume of global energy sector CO_2 emissions over the past 27 years matched the total level of CO_2 in all previous years. The trend is even more apparent over the previous two decades: since 1990, global CO_2 emissions increased by more than 50% from 20 GT/year to ~30 GT/year, as shown in Figure 1.2. Moreover, CO_2 is the primary greenhouse gas that contributes to anthropogenic climate change.[20]

In order to meet future energy demands and control CO_2 emissions, low-carbon, renewable energy production must be developed. Wind, sun, and biomass are three main renewable energy sources. Among them, solar power generation has emerged as one of the most rapidly growing renewable sources of electricity, since it has the capability to meet the world's large and growing energy demand. For example, the solar energy that strikes the surface of the earth in one hour can provide enough energy to power the entire world for a whole year.[21] Solar cells, or photovoltaic cells, are designed to turn light into electrical power. Harvesting solar energy directly from sunlight using photovoltaic devices is an essential component of future global energy production.

1.2.2 Development of Photovoltaic Cells

The development of photovoltaic devices can be traced back to 1839, when A. E. Becquerel created the world's first photovoltaic cell while experimenting with an electrolytic cell made up of two metal electrodes.[22] The first practical solar cell was announced in 1954 by Bell Labs using silicon, resulting in a device with 6%

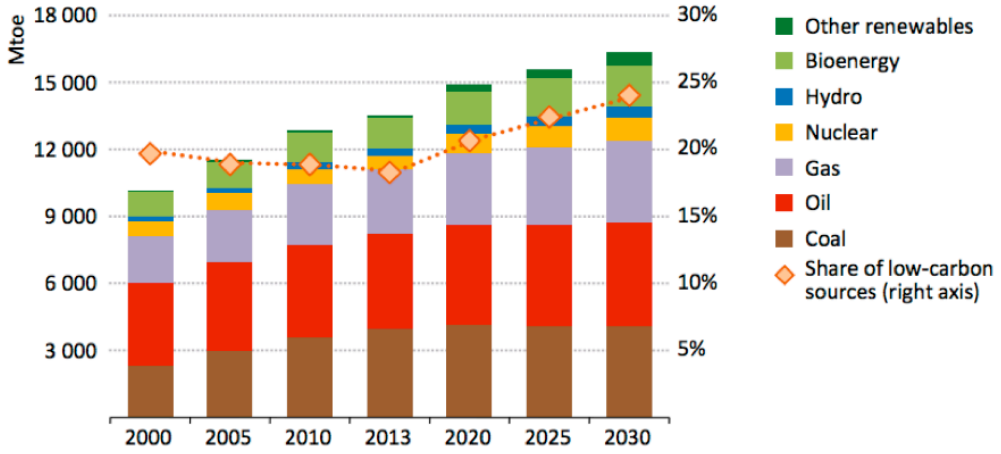

Figure 1.1: Global primary energy demand by type. Reprinted with permission from IEA Publishing. Copyright © OECD/IEA 2015 World Energy Outlook Special Report on Energy and Climate Change, IEA Publishing.

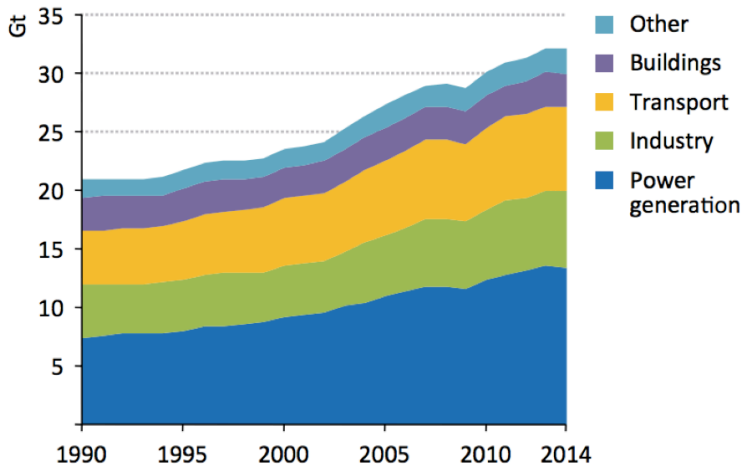

Figure 1.2: Global CO_2 emissions by sector. Reprinted with permission from IEA Publishing. Copyright © OECD/IEA 2015 World Energy Outlook Special Report on Energy and Climate Change, IEA Publishing.

efficiency.[23] For many years, the main application of solar cell technology was in the space industry.[24] By the 1960s, solar cells were the main power source for satellite applications. Later in the 1970s, investigation of photovoltaics was promoted as a means of generating terrestrial power due to the world oil crisis. Over the subsequent decades, tremendous effort has been devoted to the exploration of new, inexpensive, high efficiency and stable solar cells for both space and terrestrial applications.[25] Nowadays, solar cells are divided into four generations: The first generation is wafer-based crystalline silicon solar cells, which nowadays demonstrate efficiencies above 20%.[26] These types of solar cells dominate the world photovoltaic market, with a total market share of >90%.[27] The benefits of silicon solar cells lie in their good performance and high stability, and the typical commercial silicon solar cells last 20 years in the field.[25,28] However, this type of solar cell is rigid and heavy, and the production of crystalline silicon is energy-intensive. Second generation solar cells, also called thin film solar cells, are based on thin film materials such as GaAs, CdTe, and $Cu(In,Ga)(Se,S)_2$ (CIGS).[27] These materials have high optical absorption coefficients so that a relatively small cell thickness can harvest a large portion of the solar spectrum. Thin film solar cells are known to achieve efficiencies above 20%, but suffer from material instability, scarcity and toxicity. For example, the record efficiency of GaAs solar cells is 27.6%, but As is a toxic material that requires recycling.[26,29] The scarcity of elements such as In and Te is also a big concern for this type of solar cell.[27] Furthermore, this type of solar cell is usually grown epitaxially, using chemical

vapor deposition for the thin film growth, which is a relatively energy-intensive process.[27]

Emerging third generation photovoltaics are aimed at using inexpensive, environmentally friendly, and robust materials to achieve less expensive production and efficient light harvesting.[27] The emerging third generation includes organic solar cells (OSCs) (also called organic photovoltaics (OPVs)),[30,31] dye-sensitized solar cells (DSSCs),[32] and quantum dot solar cells (QDSCs)[33]. This generation uses conjugated molecules, organic dyes, and quantum dots to harvest light and convert it into electricity. Compared to the first two generations, the third generation has relatively low efficiency - the record efficiencies of OSCs, DSSCs, and QDSCs are 10.8%,[34–36]11.9%[26], and 9.9%[37] respectively. Among third generation solar cells, OSCs use organic semiconducting organic materials such as small molecules and polymers, which offer a wide choice of materials for application where flexibility and color are important.[31,38] Solution processed OSCs have distinct features and advantages: relative ease of processing, nontoxicity (not contaning toxic elements such as As, Cd, Pb.), low weight, potential for low cost, and the possibility of forming flexible modules of many different shapes, colors, and transparencies.[31,39,40] Therefore, OSCs can potentially be used in applications that may not be achievable with other solar cells that have much higher efficiency.

Over the last 6 years, a new class of perovskite solar cells, mixed organic–inorganic halide perovskites ABX_3 (A = CH_3NH_3 or NH_2CHNH_2, B = Pb or Sn, X = Cl, Br, I or mixed halides), have attracted a great deal of attention.[41]

The efficiency has increased rapidly from the 3.8% of the pioneer work to record efficiencies beyond 20%.[42–47]. The structure of a perovskite solar cell device is similar to that of an OSC device. The ABX_3 perovskite absorbs photons with energies larger than the bandgap to generate excitons. Charge carriers are then selectively transported to the appropriate electrode, and collected by the respective cathode/anode.[42] The tunable band gap, high absorption coefficient, long charge carrier diffusion length, and solution processability of the organic-inorganic halide pervoskite make it a promising candidate for next generation low-cost and high-effiicency solar cells.[48,49]

The topics of Pb alternatives, large-scale processing and long term stability enhancement remain a challenge for future industrialization.[50–52] Intense research efforts are attracted to device engineering for high efficiency,[47,53] study of the charge carrier transport[54–56] and light absorption properties.[57–59]

1.2.3 Advantages of Organic Solar Cells

OSCs win over first and second generation solar cells in several technological advantages, such as low material cost, mechanical flexibility, and the potential in large scale roll-to-roll production.[60,61] OSCs are based on organic semiconducting materials, so the weight of corresponding solar panels can be much lighter compared to inorganic silicon solar cells. Since most organic materials can be dissolved in certain solvents and processed by solvent casting, OSCs have the potential to employ well-established printing techniques such as roll-to-roll processing and

spray-casting.[62,63] Flexible plastic substrates are available for making flexible thin solar cells.[64] The possibility of using flexible plastic substrates in an easily scalable, high-speed printing process potentailly allows for OSCs to be manufactured at low cost.[65,66] These lightweight and flexible substrates may find applications in wearable consumer electronics. Moreover, the material can be recycled with low environmental impact.[67] In addition, the potential to tune the color and transparency of organic solar cells allows for applications in building-integrated light collecting, decoration, and outdoor recreation. From an investment perspective, OSCs have a much shorter energy payback time compared to other counterparts, as shown in Figure 1.3. Energy payback time is defined as the time required to produce the energy invested during its life cycle.[68] Compared to the first two generations, energy payback time for OSCs are shorter than the first two generations for current (1-5 years), short-term (5-10 years) as well as long-term (>10 years), making OSCs competitive.[1,69]

In summary, organic materials bear the potential to develop a long-term technology that is economically viable for large-scale power generation based on environmentally safe materials.

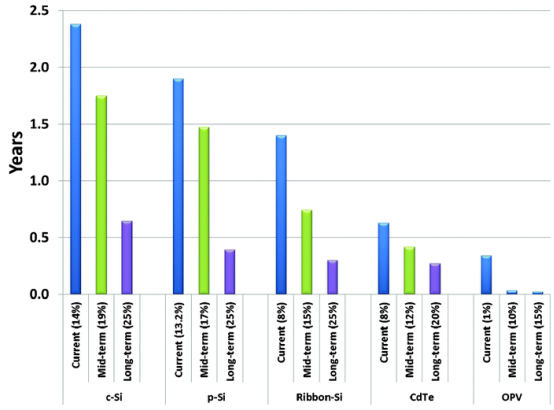

Figure 1.3: Energy payback time for silicon, CdTe, and OSC modules for current, mid-term, and long-term future scenarios. Reprinted with permission from reference.[1] Copyright 2013 by The Royal Society of Chemistry.

1.3 Basic Solar Cell Concept and Photovoltaic Parameters

In order to study and compare solar cell performance, standard photovoltaic characterization is used to test and report efficiency. J_{SC}, V_{OC}, FF, and PCE are photovoltaic parameters to report solar cell performance, and the definition will be explained in the following.

When no light is present, a solar cell behaves like a diode, allowing current to move in one direction with far greater ease than in the other. When light shines on the solar cell, photocurrent will be generated: a solar cell works as a current source in parallel with a diode.[70] In an ideal cell, the total current I equals the photocurrent I_L minus the diode current. The equation is expressed as:

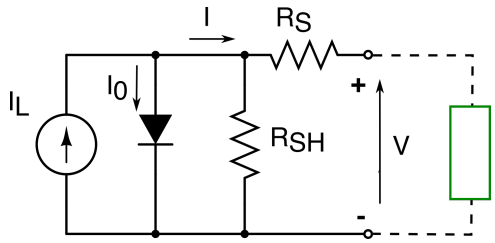

Figure 1.4: Simplified equivalent circuit model for a photovoltaic cell.

$$I = I_L - I_0(e^{\frac{qV}{kT}} - 1) \tag{1.3.1}$$

where I_0 is the saturation current of the diode; q is the elementary charge of 1.6×10^{-19} Coulombs; k is a constant of value 1.38×10^{-23} J/K; T is the cell temperature; and V is the measured cell voltage. In practice, internal resistances are present in a solar cell.[71,72] The most common parasitic resistances are the shunt resistance (R_{SH}) and series resistance (R_S). A solar cell can be modeled as depicted in Figure 1.4 when the shunt and series resistance are included.[73] The equation of the generated current can be described by:

$$I = I_L - I_0(e^{\frac{q(V+I\cdot R_S}{n\cdot k\cdot T}} - 1) - \frac{V + I\cdot R_S}{R_{SH}} \tag{1.3.2}$$

where n is the diode ideality factor; the smaller the diode ideality factor is, the more closely a diode follows the ideal diode equation.[71,74]

A current density-voltage (J-V) could be obtained to characterize the photovoltaic performance. Solar cells are electrically characterized in the dark and under simulated solar light conditions. A J-V curve is obtained by scanning

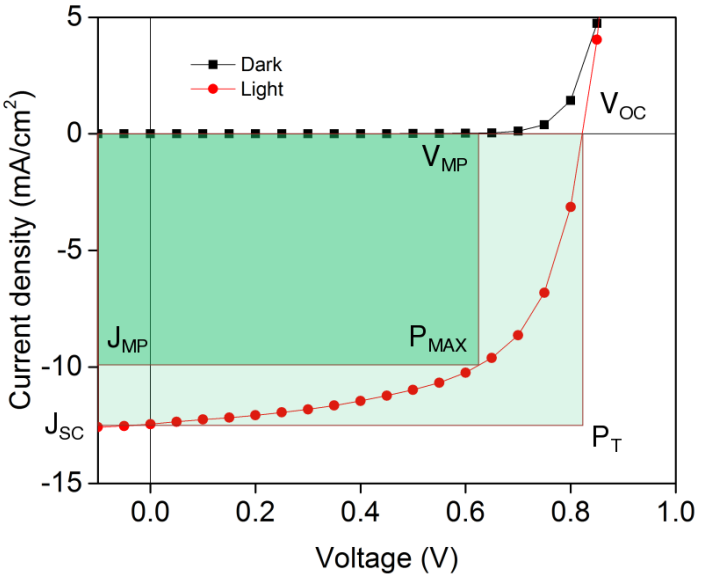

Figure 1.5: Example J-V curve of a solar cell.

an applied voltage across the solar cell and measuring the current response of the solar cell. The standard simulation condition is air mass 1.5 global (AM1.5). This represents light travelling through 1.5×air mass at a solar zenith angle of 48.2°, and is equivalent to an integrated power of 100 mW/cm^2 at 25 °C. J_{SC}, V_{OC}, FF and PCE can be extracted from the J-V curve as shown in Figure 1.5. J_{SC} corresponds to the short circuit current density that occurs when the voltage equals 0 V. In an ideal cell, the value of J_{SC} is the total current produced in the device by photon excitation.[75] V_{OC} corresponds to the open circuit voltage that occurs when no current is passing through the cell.[75] FF stands for fill factor, which measures the solar cell quality.[75] FF is defined as the ratio of the maximum power from the solar cell to the theoretical

power (P_T) that would be generated by the V_{OC} and J_{SC} values,[75] as described as:

$$FF = \frac{P_{MAX}}{P_T} = \frac{J_{MP} \cdot V_{MP}}{J_{SC} \cdot V_{OC}} \tag{1.3.3}$$

Graphically, FF is the largest possible rectangle area which could fit in the J-V curve. The power conversion efficiency (PCE, or η) of a solar cell is determined as the ratio of solar cell-generated electricity to the incident light energy, which is defined as:

$$\eta = \frac{P_{MAX}}{P_{in}} = \frac{J_{SC} \cdot V_{OC} \cdot FF}{P_{in}} \tag{1.3.4}$$

where P_{in} is the incident light power. From the J-V curve, R_S and R_{SH} are the inverse slope of the J-V curve at V_{OC} and J_{SC}, respectively. Ideally, large R_{SH} and zero R_S would define an ideal photovoltaic cell with FF equal to 1.[75] These photovoltaic parameters, J_{SC}, V_{OC}, FF, PCE, R_S and R_{SH} will be used throughout the thesis when discussing and comparing the the OSC device performance.

1.4 Structure and Operation of Organic Solar Cells

1.4.1 Operation of Organic Solar Cells

Photoactive materials, interfaces, and electrodes are the three essential parts of a typical solar cell. Modern OPV devices typically employ a bulk heterojunction (BHJ) structure.[72,76] A BHJ OSC consists of a photoactive layer and two electrodes

as shown in Figure 1.6. The photoactive layer is the core of a solar cell, which absorbs photons and convert photon energy to electron/hole charge carriers.[72] The photoactive layer usually includes a semiconducting donor polymer (or small molecule) and a fullerene acceptor. Donor materials in OSCs are generally π-conjugated semiconducting polymers or small molecules, while acceptor materials are often fullerene derivatives, such as phenyl-C61-butyric acid methyl ester (PC_{61} BM) or phenyl-C71-butyric acid methyl ester (PC_{71} BM). The donor and acceptor materials are mixed with each other, forming a three-dimensional matrix with percolating pathways for charge carrier transportation. The photovoltaic process in an OSC device is depicted in Figure 1.7 and can be divided into four steps. (1) When absorbed, a photon with energy that exceeds the donor material's bandgap excites an electron from the valence band to the conduction band, leaving a hole in the valence band. This Coulombic force-bonded electron-hole pair is called an exicton.[30,77,78] (2) Subsequently, the exciton then diffuses to the donor/acceptor interface, and separates into an electron and a hole as free charge carriers. (3) The electron is then transferred from the donor to the acceptor and further transported to the cathode through the BHJ, while the hole remains in the donor phase and further travels to the anode through the BHJ. (4) Each charge carrier is then collected by the corresponding electrodes, and a full circuit can be formed through the external load.[72,77–79]

In order to allow light to be absorbed by the photoactive layer, a transparent electrode is required. Indium-tin-oxide (ITO) is a popular material for this task

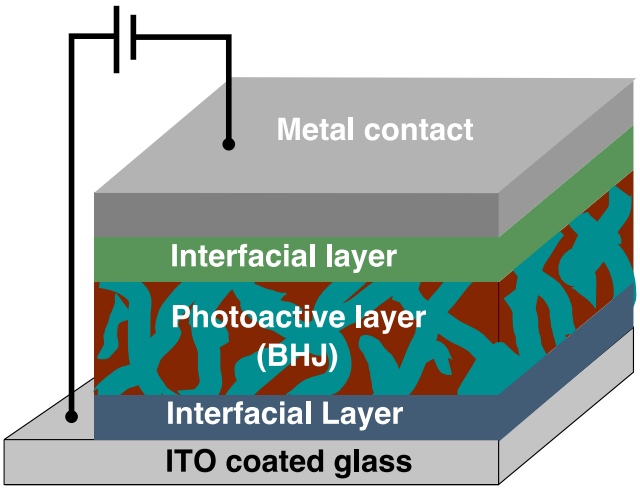

Figure 1.6: A typical BHJ solar cell structure.

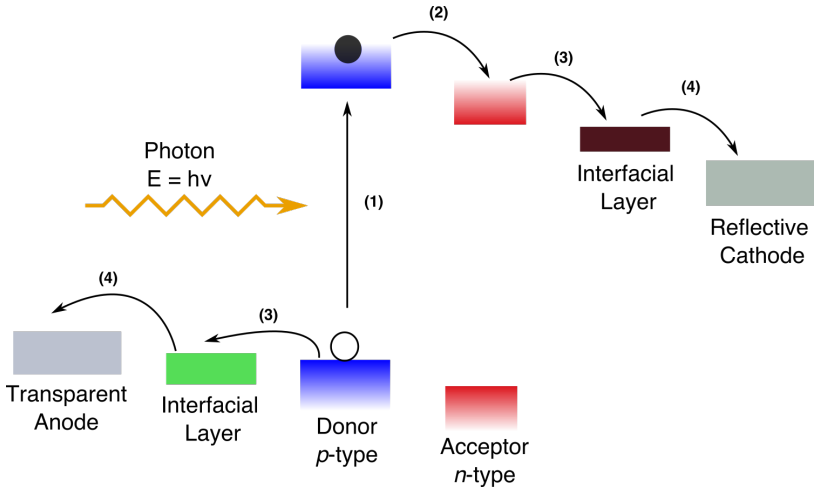

Figure 1.7: Photovoltaic process in an OSC device: (1) photon absorption, exciton generation; (2) exciton dissociation; (3) Transport of electron/hole to the interfacial layer; (4) electron/hole collection at electrode.

since it has good optical transparency in the near IR-visible region, stability, and the proper energy levels.[75] On the other side, a reflective metal electrode is usually selected to make top contact, and Al, Ag, Au are commonly used materials.[80]

At the BHJ and electrode interfaces, interfacial materials are necessary to enable effective charge collection.[81] Interfacial materials play multiple roles including making good physical and chemical contact with both the electrode and photoactive layer, acting as an optical spacer,[10] and determining the polarity of devices[82].

The overall goal of OSC research is to use an integrated approach to combining material development, interface engineering, and device engineering to fabricate high performance solution-processed organic solar cells. The work in this thesis includes each of these fields.

1.4.2 Photoactive Materials

Semiconducting organic materials that can absorb photons and convert photovoltaic energy are the key to organic solar cells.[83,84] The conductivity of semiconducting organic materials are fulfilled by the conjugated system, where π-electrons are delocalized on alternating single- and double- bonds.[85] Conjugated polymers and conjugated small molecules are both well-studied as OSC absorber materials.[85,86]

Conjugated Polymers

In the year 2000, the Nobel Prize in Chemistry was jointly awarded to Alan J. Heeger, Alan G. MacDiarmid and Hideki Shirakawa 'for the discovery and development of conductive polymers'.[87] The conductivity of conductive polymers is achieved by the conjugated systems, where the π-electrons are delocalized on the backbone chain which consists of alternating double- and single-bonds.[88] Conjugated polymers are now widely used and are the key in solar cells as photon-absorbing donor materials.

Even the early stages of OSC research were mainly based on small molecule materials, such as copper phthalocyanine (CuPc),[89] research on conjugated polymers as donors in organic solar cells has attracted intense research interest and impressive progress has been made since the 1990s.[90] The first group of well-studied semiconducting polymers were poly(phenylenevinylene) (PPV) derivatives.[91] In 1992, Sariciftci and coworkers observed that the conjugated polymer poly[2-methoxy-5-(2-ethylhexyloxy)]-1,4-phenylenevinylene (MEH-PPV) had ultrafast electron transfer to fullerene (C_{60}), which suggested the use of conjugated polymers as electron donors and fullerene derivatives as electron acceptors in OSCs.[92,93] In 1995, the concept of a BHJ was introduced, in which donor (MEH-PPV) and acceptor (C_{60}) materials are mixed to form a bicontinuous interpenetrating network with large interfacial areas for efficient exciton dissociation.[94,95] Since then, conjugated polymer and fullerene systems have been established and the concept of the BHJ has been introduced, which marked a milestone in the area.[90]

The second well-studied conjugated polymer system was polythiophene derivatives, mainly poly(3-hexylthiophene-2,5-diyl) (P3HT).[96,97] P3HT is the benchmark material for OSC studies with intesive research done with regard to understanding the structure-property relationships, processing control, and device engineering methods for high-performance polymer solar cells. Research showed that morphological control of P3HT:PCBM BHJs is the key to solar cell performance, and tremendous efforts have been done with regard to it.[1] 5% efficiency was demonstrated by the P3HT:$PC_{61}BM$-based solar cells.[98] Critical factors that could lead to desired morphology for high-performance have been studied and understood. This includes increasing regioregularity of the polymer,[99] architecture design,[99], addition of processing additives,[100,101] as well as post-deposition annealing.[98,102]

Further efficiency enhancement of P3HT:$PC_{61}BM$ OSCs is limited by the V_{OC}. In OSCs, V_{OC} is determined by the difference between the lowest unoccupied molecular orbital (LUMO) of the acceptor and the highest occupied molecular orbital (HOMO) of the donor. P3HT has a relatively large bandgap ($\sim$1.9 eV), and the energy difference between the LUMO energy level of PCBM and the HOMO energy level of P3HT is small. This leads to low V_{OC} of $\sim$0.6 V.[7] Approaches such as the development of new fullerene acceptors with higher LUMOs have been reported.[86] For example, an indene-C_{60} bisadduct (ICBA) was synthesized and used with P3HT, resulting a V_{OC} of 0.84 eV and a PCE of 6.4%.[12,103]

The third group of conjugated polymers studied was low bandgap polymers.

Table 1.1: PCDTBT:$PC_{71}BM$ solar cells processed with and without DMF solvent additive.

Cast solvent	J_{SC} (mA/cm^2)	V_{OC} (V)	FF	PCE (%)
DCB	12.44	0.88	0.57	6.23
DCB + 4% DMF	12.09	0.92	0.65	7.25

Ideally, a narrow band gap and deep HOMO level could enhance light harvesting and make a good electron donor.[7] Designing low bandgap polymers follows the concept of donor−acceptor (D−A) (in some cases named as "push−pull") copolymers, which has one electron-rich moiety (donor unit), and one electron-deficient moiety (acceptor unit).[104–109] By altering the donor and acceptor units separately, the HOMO and LUMO can be tuned accordingly.[108,110] Several high-efficiency low band gap polymers have been synthesized with high efficiency, for example, PCDTBT[111], PBDTTPD[112], and PTB7[100,109]. (Figure 1.8) 6% - 9% PCE is consistantly reported using these low bandgap polymers. With proper device engineering, 9.2% PCE is obtained using PTB7:$PC_{71}BM$.[113] An example given here is the forward PCDTBT:$PC_{71}BM$ solar cell (Figure 1.9). The PCE is 6.2%, with proper processing conditions, which can be further enhanced by using dimethylformamide (DMF) as a processing additive to bring the PCE to 7.2% (J-V curve is shown in 1.10, photovoltaic parameters are summarized in Table 1.1).

The charge carrier mobility is critical in an OSC device as, unlike silicon, the organic material usually has very low mobility, typically on the order of 10^{-3} to 10^{-4} cm^2/(V·s).[114,115] Recently, a group of polymers with diketopyrrolopyrrole (DPP) unit was developed and showed high hole mobility.[116,117] For example, PDPP-TT-

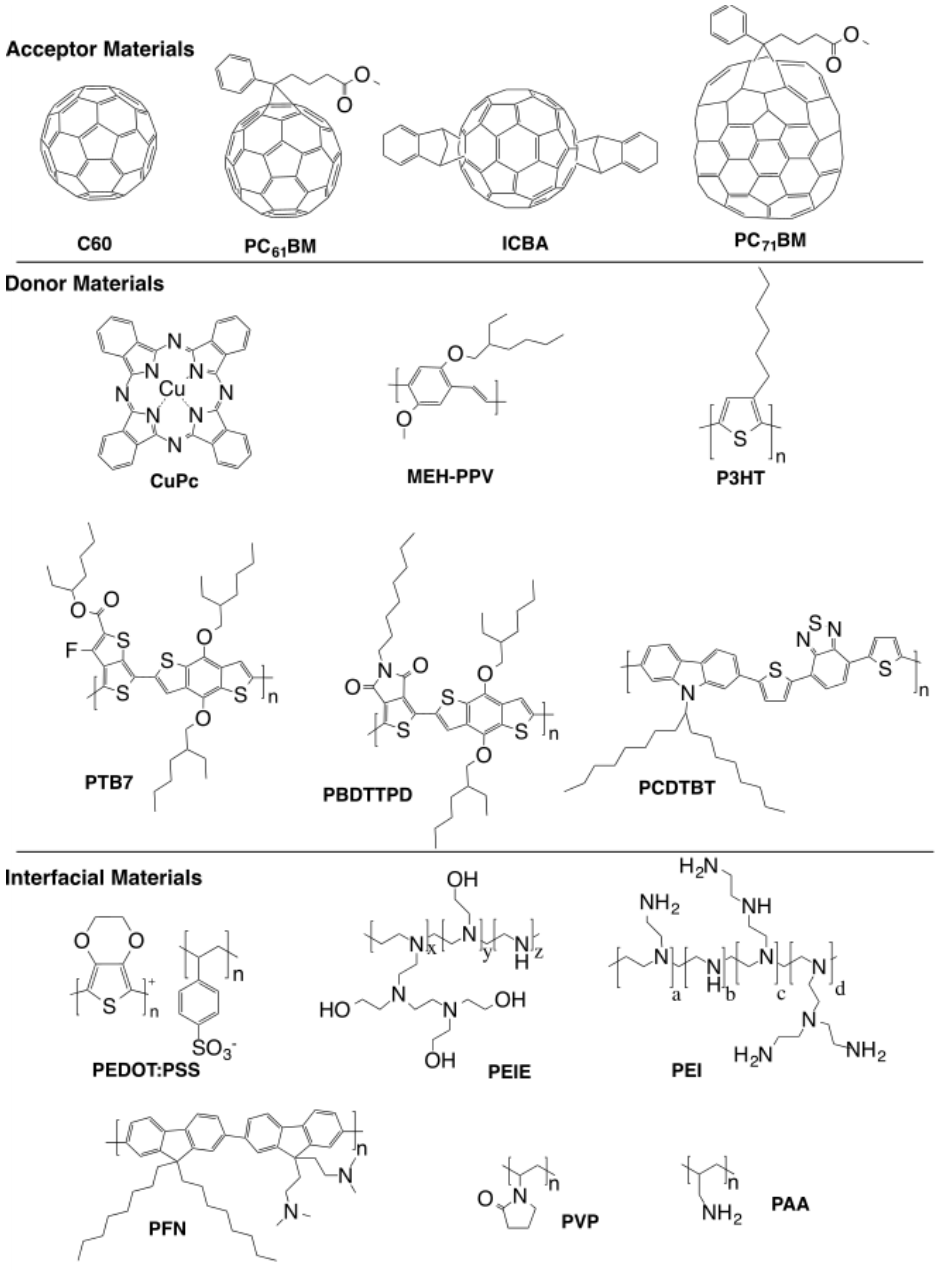

Figure 1.8: Chemical structures of common donor, acceptor, and interfacial materials.

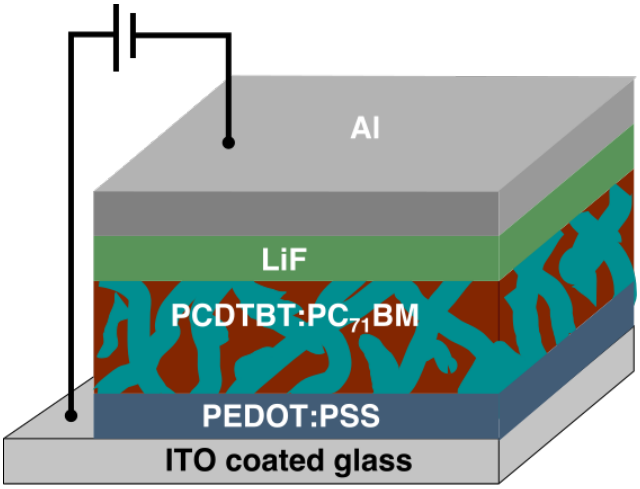

Figure 1.9: Forward PCDTBT:PC_{71}BM solar cell device structure.

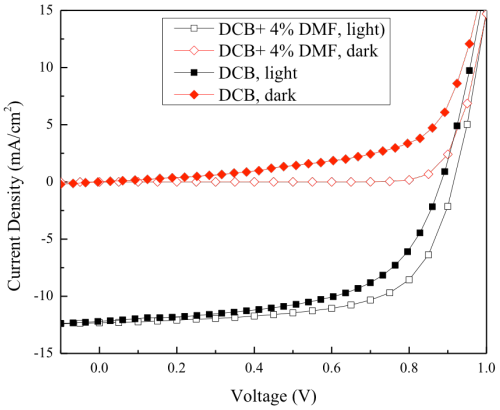

Figure 1.10: J-V curve of an forward solar cell, composed of PCDTBT:PC_{71}BM..

T-TT has a hole mobility of 1.42 $cm^2/(V \cdot s)$.[118] These polymers have hole mobilities that are several orders of magnitude greater than commonly used P3HT, and have shown great potential in achieving high J_{SC} and PCE. The record efficiency held by the a low bandgap polymer PDPPT4T-2-OD when paired with $PC_{71}BM$, is 10.5% with a J_{SC} of 18.8 mA/cm^2 .

Even though high efficiency solar cell performance using low bandgap polymers has been reported, the polymers have their own drawbacks. First, the synthesis of polymers is usually a long process, taking multiple (>10) steps to get the final product.[119] It is not only timeconsuming but also results in low yield. Second, polymers have a polydisperse molecular weight, resulting in poor control over molecular weight and often batch-to-batch variation.[120] Polymer properties regarding solar cell fabrication, such as solubility, mixing, and nanoscale phase segregation, can be affected by subtle differences in the molecular weight, polydispersity, and crystallinity, so the variation from batch-to-batch can have a profound influence on the final morphology of the BHJ, and hence on the resulting device performance.[120]

Conjugated Small Molecules

To overcome the drawbacks of the polymer donor, conjugated small molecules are promising alternatives.[121,122] Small molecule/fullerene solar cells showing efficiencies of 6-9% have been reported in recent years.[3,6,8,123,124] The first use of small molecules in solar cells can be traced back to 1986, when CuPc was first

used as a donor material in bilayer heterojunction OPV by Tang, and the device showed a PCE value of 1%.[89] Inspired by this pioneering contribution, Pc has been commonly applied in vacuum-deposited OSC devices for many years in a bilayer structure.[121,125–128] PCEs of 3.6% for bilayer devices of the architecture ITO/CuPc/C_{60}/BCP/Al were obtained by Peumans and coworkers in 2001.[129,130] Oligothiophenes, soluble acenes, triphenylamine derivatives, perylene diimides have all been extensively studied.[121,122,124,125,131–133] Modern solution processable small molecule OSCs adopt the conjugated small molecule/fullerene BHJ structure. Similar to conjugated polymers, the donor (D)-acceptor (A) concept was introduced and used for synthesis of conjugated small molecule donors. Since 2004, a class of photofunctional molecules based on electron donor (D)-acceptor (A) combinations was developed with high efficiencies.[131,134]. Zhang and coworkers reported over 9% PCE using organic small molecules.[4] Bazan and coworkers designed a series of conjugated D-A small molecules that produced PCEs as high as 8.9%.[9,10,135,136]

Compared to polymers, small molecules have several advantages: they are relatively easy to synthesize, the structure of pure small molecule is well-defined, and the molecular weight is completely monodisperse, leading to no batch-to-batch variation.[8] There are, however, fewer high-performance conjugated small molecule donors than conjugated polymers. There are several reasons: since the conjugated backbone is shorter in small molecules, the design of a conjugated structure is more difficult as compared to a polymer. Also, morphological control of BHJ is more difficult in small molecule/PCBM solar cells, since the small molecule

donor phase and (small molecule) PCBM both have nanocrystalline domains.

1.4.3 Interfaces

The interfacial layer that exists between the light-harvesting photoactive layer and the charge-collecting electrode plays an important role in determining the photon-to-electricity conversion. Proper choice of an interfacial material can optimize the electronic and electrical properties of the BHJ/electrode interfaces and improve the performance of organic solar cells.[137] A proper interfacial layer should meet several requirements: (1) it should be transparent to visible-near-IR range light to minimize optical loss; (2) it should have appropriate energy levels to enable ohmic contact; (3) it should be able to enable selective charge transport; (4) it should have good conductivity to reduce resistive losses; (5) it should be stable to prevent undesired degradation; (6) for the ease of processing, it should be soluble at low temperature; (7) have good film-forming properties; and finally, (8) be of low cost.[137,138] Choosing interfacial materials should follow these requirements as guideline.

Forming an ohmic contact is critical in OSCs, since only when ohmic contact forms between the photoactive layer and both the cathode and the anode is the energy barrier at the interface minimized, hence the V_{OC} can reach its maximum (which is determined by the difference between the LUMO of acceptor and the HOMO of donor.) The mostly widely used energy level alignment theory for OPV interface is the integer change transfer model (ICT). Ideally, at the anode side the electrode's

workfunction should be higher than the ICT^+ of the donor, while the cathode electrode's workfunction should be lower than the ICT^- of the acceptor.[139,140]

Determining device polarity is one of the most important roles of interfacial material. The interfacial layer can selectively transport a certain charge carrier and block the other so that only the electron or the hole can be extracted, while blocking the other to minimize recombination at the electrodes. In this way, the polarity of the device can be manipulated and either forward solar cells or inverted solar cells can be fabricated, depending on improved selectivity towards one charge carrier in purpose. This allows feasibility of device structure engineering.[138]

In a conventional structure, holes are extracted by the transparent conducting electrode, usually indium tin oxide (ITO).[75] In the inverted structure, electrons are extracted at the ITO electrode while holes are extracted by the metal electrode. Based on the energy level relative to polymer donor and PCBM acceptor, the interfacial material can be electron-selective (hole-blocking) or hole-selective (electron-blocking).

An example given here is the inverted design of PCDTBT:PC_{71}BM solar cells by using a hole-blocking ZnO interfacial layer for electron selection. In the previous text, a forward PCDTBT:PC_{71}BM solar cell structure was discussed. Here, an inverted PCDTBT:PC_{71}BM solar cell design is depicted in Figure 1.11. The overall performance is shown in J-V curve in Figure 1.12 and photovoltaic parameters are summarized in Table 1.2. Compared to the forward cell as mentioned above (Figure 1.10), in the inverted cell, electrons are collected at ITO cathode, while holes are

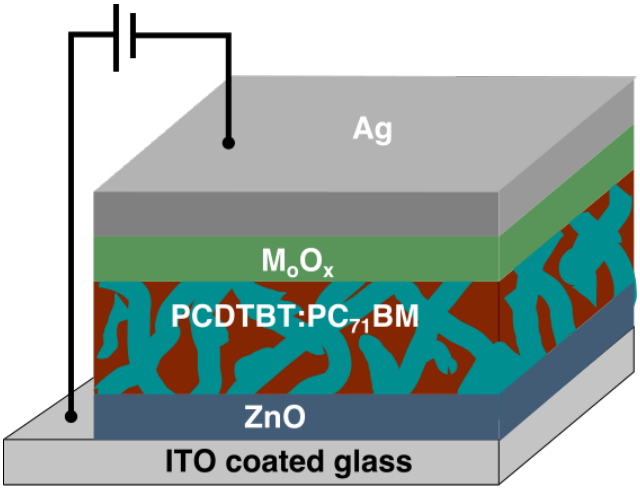

Figure 1.11: Inverted PCDTBT:PC_{71}BM solar cell device structure.

Table 1.2: Performance of an example of an inverted PCDTBT:PC_{71}BM solar cell.

Cast solvent	J_{SC} (mA/cm^2)	V_{OC} (V)	FF	PCE (%)
DCB	11.43	0.89	0.60	6.0

collected at the silver anode. Even through the PCE is slightly lower than the forward cells (1.1), the stability of cells is dramatically improved because the acidic PEDOT:PSS is not used. The acidic and hydrophilic nature of PEDOT:PSS wasily absorb water and casue solar cell degradation. The use of ZnO as a hole-blocking layer fullfil the inverted solar cell achetecture design so that electrons are collected by the ITO electrode. Proper choice of interfacial material provides the freedom of archtecture design that satisfy a variety of functions and will be disscussed in the following.[141]

Tremendous work has been done with regard to designing cathode (hole-blocking) interfacial layers and anode (electron-blocking) interfacial layers to

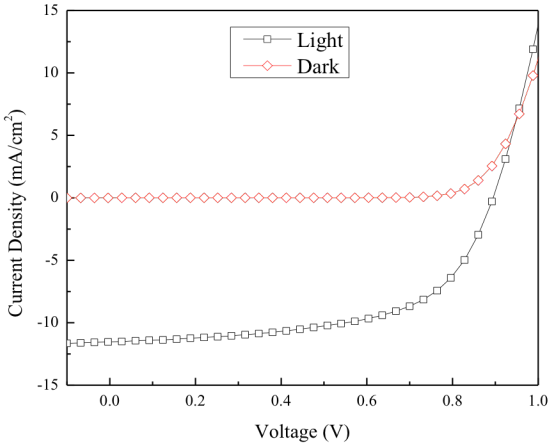

Figure 1.12: J-V curve of an inverted solar cell, composed of PCDTBT:$PC_{71}BM$.

satisfy the designs for different configurations.

Transition metal oxides with good carrier transport/extraction and superior stability such as ZnO,[142–147] TiO_2,[148,149] and CsO_x [150–153] have been developed as electron-transporting layers for OSC device,[154] Especially for ZnO, atomic layer deposited thin films, sol-gel derived thin film, and solution-processed nanoparticle films have been tested as electron-transporting layers in inverted OSC devices. Another approach for good cathode electron-transporting layers are water/alcohol-soluble polyelectrolytes. The interfacial polyelectrolytes could form dipoles on the electrode surface to reduce the workfunction. These include inexpensive nonconjugated polyelectrolytes such as poly(ethylenimine)-ethoxylated (PEIE),[155] poly(vinylpyrrolidone) (PVP),[156] polyethylenimine (PEI), and polyallylamine (PAA).[157] Conjugated polymers can be used as electron-selective layers as well, such as poly[(9,9-bis(3′-(N,N-dimethylamino)- propyl)-2,7-fluorene)-alt-2,7-(9,9-

dioctylfluorene)] (PFN)[113] and its derivatives[158–162]. Cao and coworkers used PFN as electron-selective layer in an inverted PTB7:$PC_{71}BM$ and obtained 9.2% PCE. Fullerene-based electron-selective materials provide another option, such as fullerene with functional groups of phosphoric esters,[163] amines,[164] cationic ammonium,[165] and carboxylic acids.[166,167] It is noticeable that the organic interfacial modifier can be used directly on the ITO electrode as well as in combination with the inorganic electron-selective layer. For example, Jen and coworkers developed a series of fullerene derivatives with different functional groups and applied them to the ZnO-coated ITO surface, which improved the PCE.[167]

For the anode, poly(3,4-ethylenedioxythiophene) (PEDOT:PSS) is a popular hole transporting interfacial layer that is applied to ITO.[168–172] However, PEDOT:PSS is acidic and hydrophilic, which could impair the stability of OSC device.[173–175] Replacing PEDOT:PSS has become an important topic in making stable solar cells.[176–180] Several classes of interfacial materials have been developed, including p-type transition inorganic metal oxides (NiO,[181–183] V_2O_5,[184,185] CrO_x[186]), conjugated polymer,[186] cross-linkable charge-transporting materials,[14] and graphene oxide (GO).[187–189] An alternative way is to modify the PEDOT:PSS surface instead of replacing it. In order to migrate the disadvantages, this approach commonly adopts a thin modifer on top of the PEDOT:PSS while keeping the favorable properties of the ITO/PEDOT:PSS.[12–14] Examples and works are presented and discussed in Chapter 3 in detail.

1.4.4 Electrodes

The electrodes collect electrons and holes to complete the photon-to-electricity conversion. Organic solar cells usually use ITO as the transparent electrode for light to pass through, and a metal as the reflective electrode.[190] The development of ITO electrodes can be classified into two groups. One approach aims to replace the expensive and rigid ITO with flexible, inexpensive and solution processed materials.[40,64] The other approach aims at engineering the structure of the ITO electrode to achieve high performance, such as the use of a nanostructured electrode.[191]

Although crystalline ITO has been widely adopted as a transparent electrode in solar cells, production of ITO electrodes is usually conducted under high vacuum, and the scarcity of indium will result in high production costs in the furture.[40,64] More importantly, ITO is rigid and hard, which limits the potential for flexible applications and further increases the production and transport costs in large scale production. Efforts have been made to find suitable, flexible alternative materials.[39] Composite flexible films with metal nanowires,[192–194] graphene,[195–198] carbon nanotubes,[199,200] and conducting polymers[201,202] have been extensively investigated as alternatives to ITO. Among these, silver nanowires and graphene are the two most studied. Transparent electrodes composed of random silver nanowire networks can be readily achieved by a simple and scalable process, and can be combined with metal oxides such as ZnO and TiO_2.[203] Graphene has the unique structure and excellent electronic properties for high electron transport

and chemical stability, making it a competitive electron-accepting material in OSC applications.[197]

Electrode engineering is an important research topic to improve the performance of OSCs. A nanostructured thin film made of vertical nanopillars or other three-dimensional strucutres provides a higher interfacial area for light harvesting and a direct pathway for charge transport.[204–206] Early studies of nanostructured anode electrodes are mainly considered to make hybrid solar cells, in which the nanostructured electrode is only embedded in donor polymer without the fullerene acceptor. For example, P3HT donor polymer with ZnO nanofibers results in a PCE about 0.53%.[207] ITO,[206,208,209] ZnO,[204,205,210–212] TiO_2[213] are popular materials for making one-dimensional electrodes, such as nanofibers, nanopillars, and nanorods.

In addition to inorganic materials, organic nanowires have been developed for organic solar cell electrodes as well.[214] Yoon and coworkers synthesized copper hexadecafluorophthalocyanine (F_{16}CuPc) and used it in both inverted P3HT:PC_{61}BM and PTB7:PC_{71}BM cells. Improvement was observed from 3.0% to 3.6%, and 8.1% to 8.6%, respectively.

Progress has been made with the nanostructured electrode. However, since OSCs contain solid state BHJ structures, the mechanism and effect of nanostructured electrodes on the BHJs are still not fully investigated and understood.[215] Critical issues such as light trapping, charge carrier transport and recombination still need to be considered and investigated.[215] Nanostructure geometries still need to be

improved to better meet the exciton diffusion length in polymer:fullerene BHJs to render a percolating pathway for charge transport. Further optimization of the organic-inorganic interfaces is also necessary to guarantee efficient charge separation. In summary, the electrode material, charge-selective material, interface modification, and nanostructure geometry design need to be considered, all of which further complicate device engineering.

Chapter 4 demonstrates a complete device engineering approach for high-surface-area electrodes in a polymer:fullerene solar cell, and discusses the mechanism behind the observed effects on performance.

1.5 Scope of the Thesis

This thesis is focused on developing high performance economical solar cells based on new photovoltaic material development, interfacial design, and electrode geometry design. The comprehensive idea of architecture engineering is demonstrated by considering multiple aspects of the above. Chapter 1 is a general introduction of the basic operating principles, basic concepts, characterization parameters, components of organic solar cells, the challenge of the field, and the motivation of the research topic. Chapter 2 discusses the development of a small molecule donor for OSCs. Chapter 3 discusses the role of an interfacial material and its versatile application of a variety of polymers. Chapter 4 studies the role and consequent effect of a high-surface-area electrode to improve the solar cell

performance. Chapter 5 summarizes the thesis and proposes future work.

Chapter 2 and 3 were reproduced with permission from the American Chemical Society:

He, X.‡; Cao, B.‡; Hauger, T. C.; Kang, M.; Gusarov, S.; S. M. I. Al-Rafia; Luber, E. J.; Buriak, J. M*. Donor-Acceptor Small Molecules for Organic Photovoltaics: Single Atom Substitution (Se, S). *ACS Appl. Mater. Interfaces*, **2015**, 7, 8188-8199.(‡ authors contributed equally.)

Cao, B.; He, X.; Fetterly, C.; Olsen, B. C.; Luber, E. J.*; Buriak, J. M*. Role of Interfacial Layers in Organic Solar Cells: Energy Level Pinning versus Phase Segregation. *ACS Appl. Mater. Interfaces*, **2016**, 8, 18238–18248.

2

Small Molecules for Organic Photovoltaics: The Effect of a Single Atom Substitution (Se and S)

2.1 Introduction

Conjugated small molecules represent an intriguing alternative to the widely studied polymer-based donors in OPVs due to their well-defined and uniform nature because, in a pure form, they are entirely monodisperse (polydispersity index of 1.0).[2,3,5,6,8–10,83,123,124,133,135,136,216–220] A number of examples of PCEs as high

as 8–9% have been reported, comparable to those of low-band-gap polymers, but there are far fewer examples.[2–10,83,123,124,135,136,217] Figure 2.1 and Table 2.1 show examples of the high performance small molecules. The shorter conjugated backbone, when compared with a polymer, renders the design of a low-band-gap material difficult. In addition, the generation of a nanoscale phase-segregated BHJ with a small-molecule donor and a (small-molecule) fullerene acceptor, which should contain nanocrystalline domains of both materials, is problematic because of the mutual miscibility of these two compounds; morphological control is therefore difficult. To tackle the challenge of designing a small molecule with a suitable band gap, the electronic characteristics can be manipulated via control of the intramolecular D–A combination. From a synthetic standpoint, small molecules are typically more easily synthesized than polymers, and one can therefore incorporate a range of different donor and acceptor units in a specific sequence, thus providing a precise approach to fine-tuning the optoelectronic properties. Recently, Bazan and co-workers reported a class of small molecules with multiple alternating D–A (D1–A–D2–A–D1) chromophores;[9,10,135,136] one representative example is *p*−DTS(FBTTh$_2$)$_2$ (as shown in molecule **15** in Figure 2.1 and Figure 2.2a), which when coupled with PC$_{71}$BM, achieved a high PCE of 8.9%.[10,135] Further studies by the same group led to the development of new small-molecule donor materials through replacement of the central donor constituent with a silaindacenodithiophene unit, which resulted in PCEs of 4–6%, when paired with PC$_{71}$BM.[9] Another related study, by Chabinyc and co-workers, showed that a very subtle change of a single

bridging atom, from Si to C, in the central donor unit led to a significant loss of PCE (less than 1%).[136] These results demonstrate that the multiple D1–A–D2–A–D1 chromophore configuration is a versatile framework and that systematic tuning of the different donor and/or acceptor fragments and configurations can have a dramatic effect on the resulting OPV performance. In addition, the identity of the central donor unit (D2) has been shown to be of great importance with respect to the optoelectronic properties as well as the device performance[9,10,135,136] but has been explored only cursorily; the relationship between the electron acceptor (A) unit and the photovoltaic performance remains ill-defined but is worth surveying further.

The S-containing benzothiadiazole (BT) unit (shown in figure 2.1, structure **16**) is a well-known electron-acceptor unit that has been widely used in polymer-based high-efficiency OPVs.[218,222–225] Substitution of the S atom with heavier chalcogenides (e.g., Se, Te) in π-conjugated materials has created a promising route forward for expanding the repertoire of conjugated subunits because of their very unique structural (i.e., bonding) and electronic properties.[226–234] Replacement of thiophene with selenophene in a polymer backbone generally results in a lowering of the polymer band gap, and some of these selenophene-containing polymers exhibit higher photovoltaic efficiency.[226–234] Following the same trend with respect to the Se analogue of BT (benzoselenadiazole, BS), several research groups have shown that BS-containing polymers exhibit a red-shifted absorption spectrum relative to their BT-containing counterparts when combined with the same electron-donating moiety.[235–239] Another example of interesting research

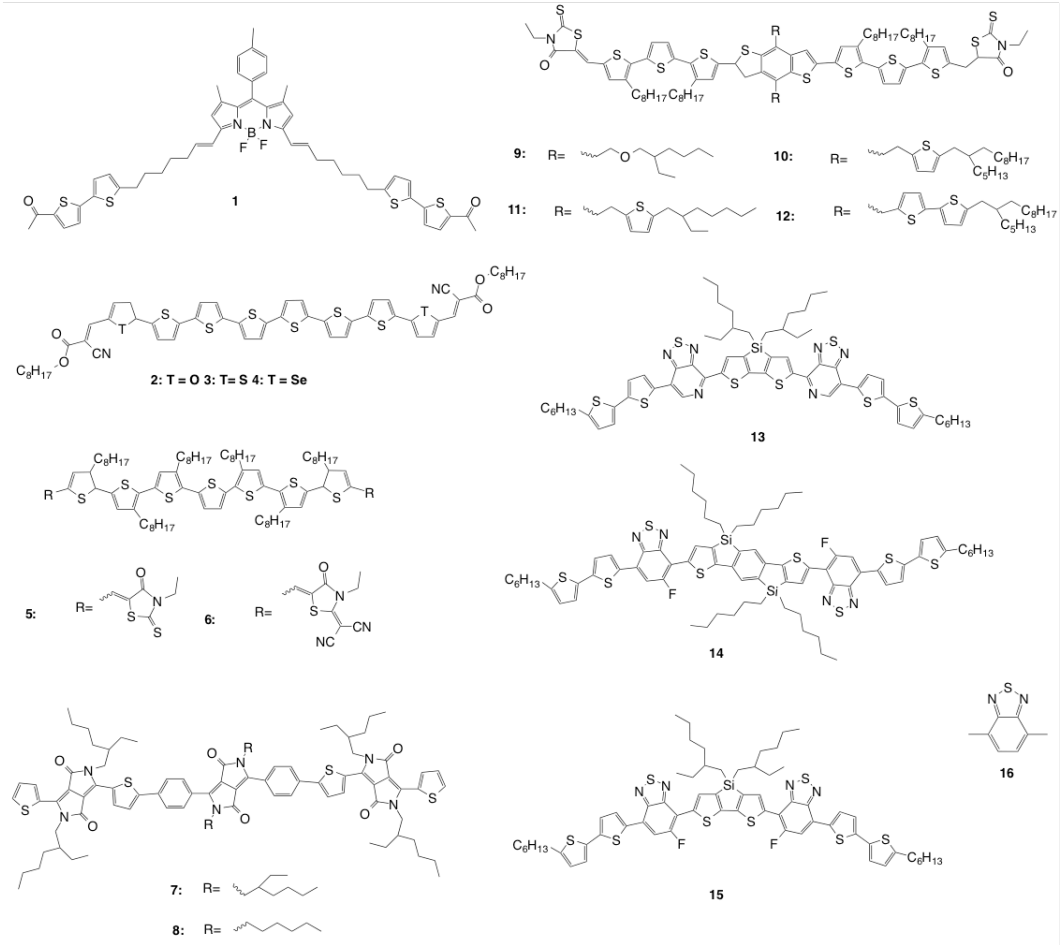

Figure 2.1: Chemical structured of the high-performance conjugated small molecules: **1**,[2] **2-4**,[3] **5-6**,[4] **7-8**,[5] **9-12**,[6,7] **13**,[8] **14**,[9] **15**,[10] and **16**, the benzothiadiazole (BT) unit.

Table 2.1: Photovoltaic performance of molecules.**1-15**

Molecule	Blend ratio (to $PC_{71}BM$)	Additives	J_{SC} (mA/cm^2)	V_{OC} (V)	PCE (%)	FF
1[2]	1:0.5	–	14.3	0.70	4.5	0.47
2[3]	1:1.2	–	6.34	0.78	3.18	0.64
3[3]	1:1.2	–	7.43	0.85	4.52	0.72
4[3]	1:1.2	0.1mg/mL PDMS[a]	10.79	0.85	6.15	0.67
5[4]	1:0.5	–	14.87	0.91	9.30	0.678
6[4]	1:0.5	–	9.49	0.89	4.35	0.516
7[5]	1:1	1%DIO[b]	8.98	0.89	4.8	0.606
8[5]	4:6	1%CN [c]	10.40	0.86	5.5	0.617
9[6,7]	1:0.8	0.2 mg/mL PDMS	12.21	0.93	7.38	0.650
10[6,7]	1:0.8	0.2 mg/mL PDMS	13.17	0.93	8.12	0.63
11[6,7]	1:0.8	0.2 mg/mL PDMS	11.92	0.96	6.79	0.594
12[6,7]	1:0.8	0.2 mg/mL PDMS	12.09	0.92	8.02	0.721
13[8]	0.7:0.3	0.25% DIO	14.4	0.78	6.70	0.593
14[9]	1:1	0.4%DIO	11.0	0.91	6.4	0.65
15[10,221]	0.6:0.4	0.4%DIO	15.5	0.799	8.94	0.565

[a] PDMS, polydimethylsiloxane; [b] DIO, 1,8-Diiodooctane; [c] CN, 1-chloronaphthalene.

has revealed that benzoselenodiazole-containing small molecules assemble to form head-to-head dimers in the solid state because of a tendency to form intermolecular Se–N interactions.[240] Therefore, utilization of these two isostructural electron-acceptor units, BT and BS, in a small-molecule design is expected to affect the optical properties, molecular packing, and ultimately the photovoltaic performance.

Herein, we report two isostructural small molecules, 7,7′-[4,8-bis(2-ethylhexyloxy)benzo[1,2-b:4,5-b′]dithiophene]bis[6-fluoro-4-(5′-hexyl-2,2′-bithiophen-5-yl)benzo[c][1,2,5]thiadiazole] (**1**) and its selenium analogue 7,7′-[4,8-bis(2-ethylhexyloxy)benzo[1,2-b:4,5-b′]dithiophene]bis[6-fluoro-4-(5′-hexyl-2,2′-bithiophen-5-yl)benzo[c][1,2,5]selenodiazole] (**2**), shown in Figure 2.2a. The architecture of these two materials is based on a D1–A–D2–A–D1 chromophore configuration, with the electron-rich benzo[1,2-b:4,5-b′]dithiophene (BDT) as the central donor unit (D2) and bithiophene end-capping donor units (D1). BDT was chosen as the central core because it is a well-known electron-donating unit and has been widely utilized as a key building block in low-band-gap polymers and small molecules for efficient solar cells.[112,241,242] The main aim of this work was to investigate the effect of one-atom substitution of S with Se in the acceptor unit (A) on the optoelectronic properties and photovoltaic performance of devices incorporating these small molecules.

2.2 Results and Discussion

2.2.1 Synthesis and Physical Properties of 1 and 2

The synthetic routes for **1** and **2**, as well as several key intermediates, **S3**, **S5**, and **S6**, are summarized in Figure 2.2. 4,7-Dibromo-5-fluorobenzo[c][1,2,5]thiadiazole (**S1**) was prepared according to a reported procedure.[135] The Se analogue **S3** was synthesized from **S1** in high yield (56% overall yield in two steps). Reduction of **S1** using excess $NaBH_4$ led to the diamine intermediate **S2**, followed by reoxidation with SeO_2 to form the Se-containing molecule, **S3**. Subsequently, the asymmetric dibromo species (**S1** or **S3**) was then selectively reacted with 5′-hexyl-2,2′-bithiophene-5-boronic acid pinacol ester (**S4**) via Suzuki coupling to afford **S5** and **S6** in modest yield (30–45%). **S5** and **S6** were then coupled with the BDT donor unit **S7** through a Stille coupling to afford **1** and **2** in high yield (80–90%). These two final products were fully characterized by multinuclear NMR (^{1}H, ^{13}C, and ^{19}F) spectroscopy, high-resolution mass spectrometry (HRMS), and elemental analysis. The solubility of **1** (*ca.* 20 mg/mL) in chlorobenzene (CB) at room temperature is substantially lower than that of **2** (*ca.* 40 mg/mL). The difference in the solubility is contrary to the expectations of intermolecular Se–Se bonding in the solid state, which should decrease the solubility. In the case of these small molecules, however, π–π stacking and pendant alkyl chain interactions dominate (*vide infra*); because Se has a larger atomic radius than S, the interplane distance for π–π stacking would be expected to increase,[243] thus leading to a weakening of the

strength of this interaction in the solid state. The thermal stability was evaluated by thermogravimetric analysis (TGA), and the decomposition temperatures (T_d, defined as the temperature corresponding to >5% mass loss) for **1** and **2** were determined to be 335 and 310 °C, respectively, indicating high thermal stability (Figure 2.3). The melting temperatures (T_m) for **1** and **2**, determined by differential scanning calorimetry (DSC), are 243 and 237 °C, respectively.

2.2.2 Optoelectronic Properties

Figure 2.4 and Table 2.1 show the UV–vis absorption spectra of **1** and **2** in solution and as films on a glass substrate and the corresponding photophysical data (Table 2.4). In a $CHCl_3$ solution, **1** displays absorption maxima at λ_{max} = 369 (ϵ = 4450) and 550 nm (ϵ = 5440), while the absorption maxima of **2** are located at λ_{max} = 351 (ϵ = 6990), 382 (ϵ = 7120), and 581 nm (ϵ = 5920); the absorption profile of the Se-containing **2** is red-shifted ∼30 nm compared to that of **1** and has higher extinction coefficients. A similar red shift was also observed upon comparison of the two molecules in film form, with the films of **1** and **2** appearing purple and aqua, respectively (maxima: for **1**, λ_{max} = 378 and 589 nm; for **2**, λ_{max} = 390, 621, and 665 nm). Such red shifting of the absorption maxima upon moving from S to Se is most likely due to the lower ionization potential of the larger atom (Se), which, in turn, leads to a shallow highest occupied molecular orbital (HOMO) level and a smaller band gap.[244] Moreover, the absorption profiles of thin films of both compounds exhibit vibronic structuring in the 500–700 nm region, with a significant

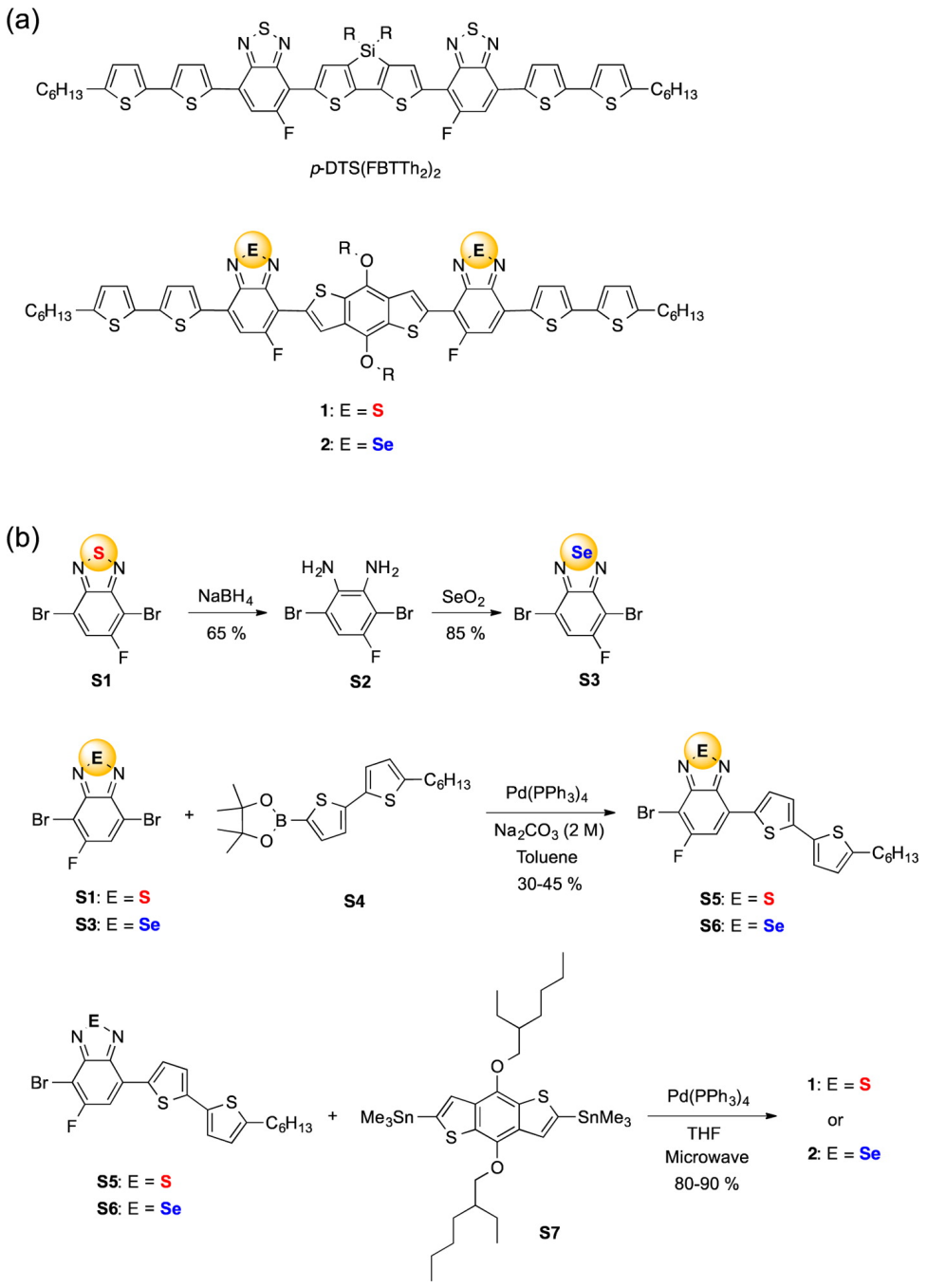

Figure 2.2: (a) Molecular structures of $p-\mathrm{DTS(FBTTh_2)_2}$, **1**, and **2** and (b) synthetic routes toward **1** and **2**. Reprinted with permission from reference.[11] Copyright 2015 by American Chemical Society.

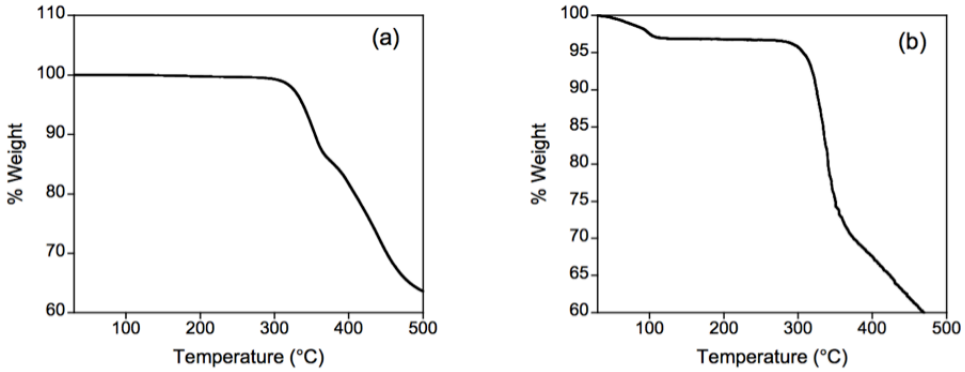

Figure 2.3: TGA analysis of (a) **1** and (b) **2**.

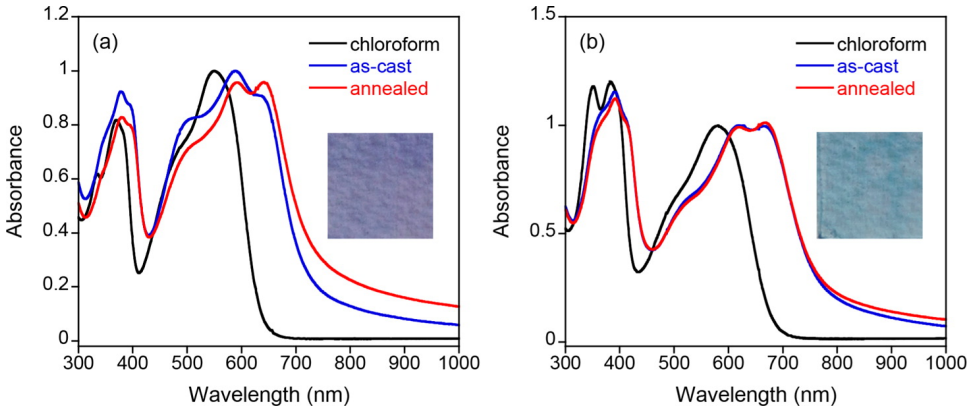

Figure 2.4: Normalized UV–vis absorption of (a) **1** and (b) **2** under different conditions. The black trace refers to a solution in $CHCl_3$ (1×10^{-5} M), the blue trace to a film spin-coated from a chlorobenzene solution (**1** was spin-coated at 80 °C, and **2** was spin-coated at room temperature), and the red trace to the spin-coated film after annealing for 2 min at 80 °C in N_2. Insets show the colors of thin films of **1** and **2** on glass. Reprinted with permission from reference.[11] Copyright 2015 by American Chemical Society.

Table 2.2: Optoelectronic properties of **1** and **2**.

Compound	λ_{abs} (ϵ[a]) in $CHCl_3$		λ_{abs} in film		E_{HOMO}[b] [eV] (Calculated)[c]	E_{LUMO} [eV] (Calculated)	E_g[d] [eV] (Calculated)
	λ_{abs}	λ_{onset}	λ_{max}	λ_{onset}			
1/1'	369 (4450), 550 (5440)	651	378, 589	735	-5.4 (-5.08)	-3.7 (-3.13)	1.7 (1.96)
2/2'	351 (6990), 382 (7120), 581 (5920)	694	390, 621, 665	784	-5.2 (-5.03)	-3.6 (-3.18)	1.6 (1.85)

[a] Molar extinction coefficient ([$dm^3mol^{-1}cm^{-1}$]); [b] Measured by UPS; [c] DFT calculations based on (B3LYP/6-31+G(d,p) level of theory for **1'** and **2'**; [d] Determined from the onset of films as taken by UV-vis. E_{LUMO} was calculated as per $E_{LUMO} = E_{HOMO} + E_g$.

red shift compared to that of the solution, which is typical of a more ordered structure in the film state.[3,5,245] Upon brief thermal annealing (80 °C for 2 min, under N_2), the film absorbance of **1** undergoes a small red shift of approximately 5 nm, with a slightly enhanced peak intensity ratio of A_{640}/ A_{585}, suggestive of increased molecular order.[9,246,247] No obvious red shift, akin to that seen upon annealing films of **1**, was observed for **2**, perhaps because of prior aggregation at room temperature before annealing, as suggested by X-ray diffraction (XRD; *vide infra*).

From the onset of film absorption (for **1**, λ_{onset} = 735 nm; for **2**, λ_{onset} = 784 nm), the optical band gaps of **1** and **2** were estimated to be 1.7 and 1.6 eV, respectively. A smaller band gap for Se-containing compounds, when compared to their S-containing congeners, has been observed in many other conjugated systems.[222,224–233,235–239,244] Ultraviolet photoelectron spectroscopy (UPS) was employed to determine the HOMO levels of **1** and **2** (Figure 2.5 and Table 2.4), and they were calculated to be −5.4 and −5.2 eV, respectively. The deeper HOMO level of **1** is consistent with the higher ionization potential of S than Se.[243,244]

Table 2.3: Physical properties of **1** and **2**.

Compound	T_m[a] [°C]	T_m[a] [°C]	Solubility[c] [mg/mL]
1	243	335	20
2	237	310	40

[a] Melting temperature (T_m) determined by differential scanning calorimentry (DSC); [b] Decomposition temperature (T_d) determined by thermogravimetric analysis (TGA); [c] In chlorobenzene, at 21 °C.

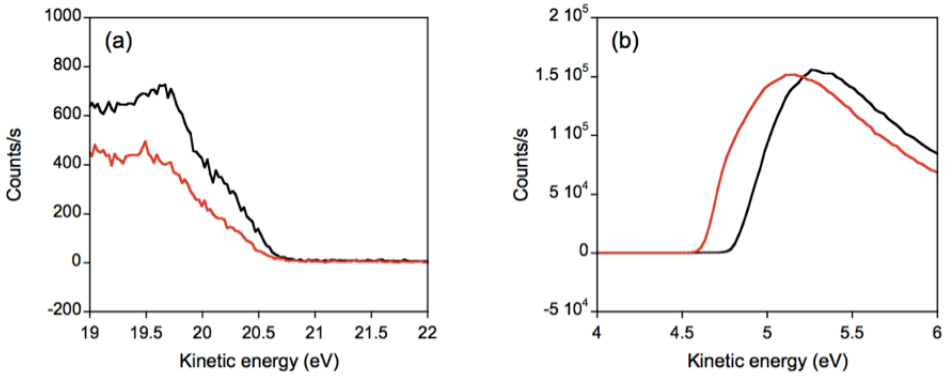

Figure 2.5: UPS spectra of (a) the valence band and (b) the secondary electron cutoff region of **1** (black line) and **2**. Reprinted with permission from reference.[11] Copyright 2015 by American Chemical Society.

Table 2.4: Determination of HOMO energy level of **1** and **2** based on UPS spectra.

Compound	$E_{HOMO,onset}$ (eV)	E_{cutoff} (eV)	E_{HOMO} (eV)
1	20.63	4.80	5.39 (rounded to 5.4 eV)
2	20.60	4.62	5.24 (rounded to 5.2 eV)

$E_{HOMO} = 21.2eV - E_{HOMO,onset} + E_{cutoff}$.

2.2.3 Theoretical Analysis

To better understand the optical and electronic characteristics of these two molecules, density functional theory (DFT) calculations [B3LYP/6-31+G(d,p) level of theory][248] were performed on **1** and **2**. For simplicity, the ethylhexyl and hexyl groups were replaced by methyl substituents; these compounds were labeled **1′** and **2′**. Both compounds adopt a highly planar structure in the optimized structure, suggesting extended π-conjugation along the length of the molecule. The HOMO and lowest unoccupied molecular orbital (LUMO) energy isosurfaces and energy levels are shown in Figure 2.6 and Table 2.2 and appear quite similar for **1′** and **2′**. The HOMOs of both small molecules are extensively delocalized, while the LUMOs are located mainly on the electron-accepting BT (for **1′**) or BS (for **2′**) units. Interestingly, with respect to the BT and BS units, the HOMO has no contribution from the heteroatoms (S or Se), while the LUMO is affected significantly by the presence of these heteroatoms. The calculated HOMO and LUMO energies of **1′** are $E_{HOMO} = -5.08$ eV and $E_{LUMO} = -3.13$ eV, with a calculated energy gap of $\Delta E = 1.95$ eV. **2′** has a higher HOMO level ($E_{HOMO} = -5.03$ eV), a lower LUMO level ($E_{LUMO} = -3.18$ eV), and a smaller band gap ($\Delta E = 1.85$ eV), as summarized in Table 1. These trends are consistent with the experimental data derived from UV–vis and UPS spectroscopy for **1** and **2**.

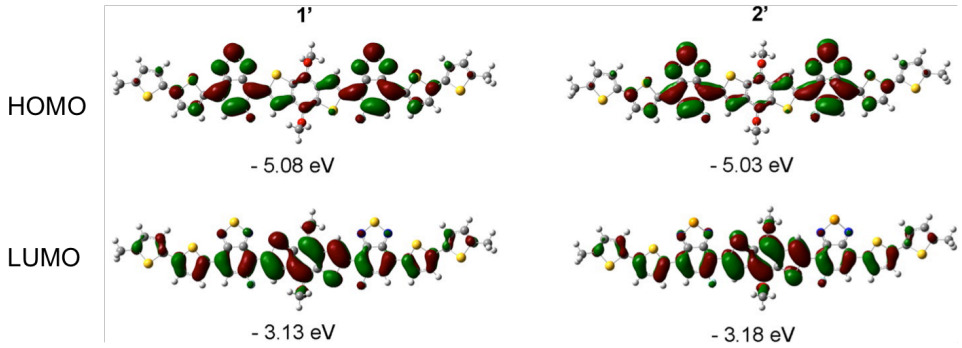

Figure 2.6: Frontier molecular orbital isosurfaces and energy levels using DFT calculations based on the B3LYP/6-31+G(d,p) level of theory for **1′** and **2′**. Reprinted with permission from reference.[11] Copyright 2015 by American Chemical Society.

2.2.4 Device Performance

Thin-film BHJ solar cells were fabricated with the architecture ITO/PEDOT:PSS/[**1** or **2**]:$PC_{71}BM$/LiF/Al/Mg and tested under one sun illumination (AM 1.5G, 100 mW/cm^2). Mg was chosen so that substrate temperatures do not exceed 60 °C during deposition and confound the studies on the annealing temperature, thanks to the low sublimation temperature of this element. The active layer was spin-coated from a chlorobenzene solution at 80 °C (this elevated temperature is required because of the poor solubility of **1** at room temperature). All solution processing was carried out in air. As a starting point, the reported optimal conditions for devices based on the small-molecule $p-DTS(FBTTh_2)_2$ (2.2a),[135] where the $p-DTS(FBTTh_2)_2/PC_{71}BM$ ratio was 1.5:1 (*w/w*), were used. Table 2.5 summarizes the device performance. First, when the devices were compared based on [**1** or **2**]/$PC_{71}BM$ prepared from solutions heated to 80 °C, the PCEs were 1.0 ± 0.1% and 1.7 ± 0.1%, respectively, with the most obvious difference observed

Table 2.5: Photovoltaic characteristics of BHJ solar cells with active layers of **1** or **2** and $PC_{71}BM$, at different ratios.

Compound	Blend ratio[a]	Thermal anneal[b]	J_{SC} (mA/cm^2)	V_{OC} (V)	FF	Average PCE (%)
1[c]	1.5:1	N	3.6 ± 0.2	0.64 ± 0.01	0.46 ± 0.10	1.0 ± 0.1
	1.5:1	Y	3.6 ± 0.1	0.66 ± 0.10	0.46 ± 0.01	1.0 ± 0.1
2[c]	1.5:1	N	7.2 ± 0.1	0.66 ± 0.10	0.35 ± 0.10	1.7 ± 0.1
	1.5:1	Y	7.0 ± 0.2	0.68 ± 0.10	0.35 ± 0.10	1.7 ± 0.1
2[d]	1.5:1	N	5.3 ± 0.3	0.62 ± 0.05	0.33 ± 0.01	1.0 ± 0.1
	1:1	Y	6.5 ± 0.5	0.71 ± 0.10	0.40 ± 0.01	1.8 ± 0.2
	1.5:1	Y	8.9 ± 0.2	0.71 ± 0.10	0.40 ± 0.01	2.6 ± 0.1
	1:1	Y	8.2 ± 0.5	0.72 ± 0.01	0.44 ± 0.03	2.5 ± 0.1

[a] 30 mg/mL in chlorobenzene, spin-coated at 1500 rpm for 1 min; [b] Active layer thermally annealed at 80 °C for 2 min; [c] spin-coated at 80 °C; [d] spin-coated at room temperature.

with J_{SC}; the J_{SC} value of **2**/$PC_{71}BM$ was twice as high as that of **1**/$PC_{71}BM$. In both cases, subsequent thermal annealing had no effect on the PCE, and the parameters (J_{SC}, V_{OC}, and FF) were largely unchanged. However, when devices based on **2**/$PC_{71}BM$ were prepared at room temperature (PCE = 1.0 ± 0.1%) and then thermally annealed, the PCE improved significantly, to 2.6 ± 0.1%, with increases in J_{SC} (to 8.9 ± 0.2 mA/cm^2), Voc (to 0.71 ± 0.10 V), and FF (to 0.40 ± 0.01). It is noted that devices of **1**/$PC_{71}BM$ could not be prepared at room temperature because of the low solubility of **1** at room temperature. Figure 2.7 shows the current density–voltage (J–V) curves of devices based on the BHJs of **1**/$PC_{71}BM$ (prepared at 80 °C) and **2**/$PC_{71}BM$ (prepared at 80 °C and room temperature), without and with thermal annealing, under **1** sun illumination (AM 1.5G, 100 mW/cm^2).

Because of the promising increase in the PCE observed with the BHJ based

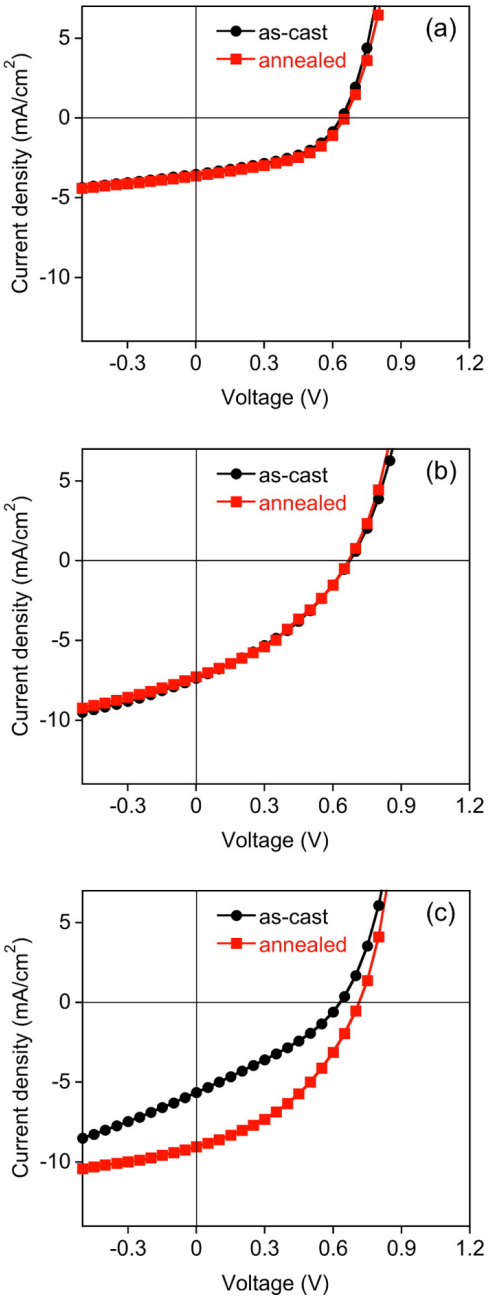

Figure 2.7: Typical J–V curves of (a) **1**/$PC_{71}BM$ spin-coated at 80 °C; (b) **2**/$PC_{71}BM$ spin-coated 80 °C; (c) **2**/$PC_{71}BM$ spin-coated at room temperature. The ratio of [**1** or **2**]/$PC_{71}BM$ was 1.5:1 (*w/w*). Reprinted with permission from reference.[11] Copyright 2015 by American Chemical Society.

on **2**/$PC_{71}BM$, further optimization was carried out on this combination, with the results summarized in Tables 3 and 4. Variation of the thermal annealing times under nitrogen (1, 2, and 5 min) and temperatures (80, 100, and 120 °C) was also investigated (Tables 2.6 and 2.7. A total of 2 min of thermal annealing was found to be marginally better than 1 min, but with 5 min of annealing, V_{OC} was lowered, leading to a drop of the PCE to below 2%, and thus all thermal annealing was carried out for 2 min. Increasing the **2**/$PC_{71}BM$ ratio from 1.5:1 to 2:1 gave a similar PCE of 2.5 ± 0.1%, while a lower ratio of **2**/$PC_{71}BM$ of 1:1 resulted in a lower PCE of 1.8 ± 0.2%. The lowering of the PCE, with a higher loading of $PC_{71}BM$, could be ascribed to the inherent tendency of fullerene to aggregate under elevated temperatures, forming larger aggregates.[249,250] The effects of the addition of 1,8-diiodooctane (DIO), a commonly used high-boiling-point solvent additive that has improved the device performance in OPV devices, were examined, and unlike the system of $p-DTS(FBTTh_2)_2$:$PC_{71}BM$, reported by Bazan and co-workers,[5,10,135] the addition of DIO (0.5, 1.0, and 1.5%) to **2**/$PC_{71}BM$ did not enhance the PCE. Another aspect that is critical to the OPV performance is the thickness of the BHJ, and Table 2.8 summarizes the relationship between the spin-coating conditions and the organic film thickness, as well as the device performance, using a **2**/$PC_{71}BM$ (1.5:1, 30 mg/mL) blend. When the acceleration rate constant was kept at 900 rpm/s, changing the spin rate from 600 to 2000 rpm led to different film thicknesses ranging from 181 ± 10 to 89 ± 5 nm. The optimized spin rate was determined to be 1500 rpm, which gave a ∼109-nm-thick film, resulting in the reported average PCE of

Table 2.6: The effect of annealing temperature on the performance **2**:$PC_{71}BM$ solar cells.

Annealing temperature (°C)	J_{SC} (mA/cm^2)	V_{OC} (V)	PCE (%)	FF
80	6.34 ± 0.61	0.67 ± 0.06	1.68 ± 0.24	0.38 ± 0.01
100	5.98 ± 0.91	0.58 ± 0.17	1.33 ± 0.41	0.39 ± 0.08
120	2.19 ± 0.39	0.53 ± 0.02	0.38 ± 0.08	0.32 ± 0.00

2:$PC_{71}BM$ (1.5:1, 30 mg/ml total concentration), spin-cast at 1200 rpm at room temperature, annealed under N_2 for 5 min.

Table 2.7: The effect of annealing time on the performance **2**:$PC_{71}BM$ solar cells.

Annealing time (min)	J_{SC} (mA/cm^2)	V_{OC} (V)	PCE (%)	FF
5	8.27 ± 0.52	0.58 ± 0.22	1.89 ± 0.86	0.36 ± 0.05
2	8.74 ± 0.18	0.71 ± 0.00	2.47 ± 0.49	0.39 ± 0.01
1	8.85 ± 0.25	0.69 ± 0.02	2.28 ± 0.19	0.38 ± 0.02

2:$PC_{71}BM$ (1.5:1, 30 mg/ml total concentration), spin-cast at 1500 rpm at room temperature, annealed at 80°C.

2.6 ± 0.1%.

2.2.5 Device Characterization

In order to gain insight into the effects of annealing and the difference in performances between devices fabricated from **1** and **2**, UV–vis, grazing-incidence X-ray diffraction (GIXRD), and atomic force microscopy (AFM) characterization of these devices was performed. Shown in Figure 2.8 are the UV–vis spectra of the as-cast devices (room temperature and 80 °C) and the annealed devices (annealing conditions: 80 °C, 2 min under nitrogen). In all cases, we see that there is a similar increase in absorbance in the visible spectrum. Similar increases of absorbance of

Table 2.8: Effect of the film thickness on the device performance using **2**:$PC_{71}BM$ (ratio = 1.5:1, 30 mg/mL, spin-coated at room temperature).

Spin rate (rpm)	Acceleration rate (rpm/s)	Film thickness (nm)	PCE (%)
600	900	181 ± 10	0.8 ± 0.1
1000	900	153 ± 5	1.1 ± 0.1
1200	900	133 ± 7	1.8 ± 0.2
1500	900	109 ± 3	2.6 ± 0.1
2000	900	89 ± 5	1.7 ± 0.2

small-molecule-based OPV devices upon thermal annealing have been attributed to better packing of the molecules in the film.[4] Given that all device configurations demonstrate similar as-cast UV–vis absorption profiles and increases in absorbance upon annealing, it is unlikely that these structural changes are responsible for the resulting differences in the device performance. Specifically, there does not appear to be any correlation between the changes in the device performance with an increase in UV–vis absorption. Devices cast at 80 °C have no change in their performance after annealing, while those cast at room temperature experience a significant increase in their performance, despite all devices having similar increases in UV–vis absorbance.

Also shown in Figure 2.8 are the corresponding GIXRD spectra of all device configurations before and after annealing at 80 °C. Upon inspection of the GIXRD spectra of **1**/$PC_{71}BM$ and **2**/$PC_{71}BM$ cast at 80 °C, we see that a single reflection at 2θ = 6.8° is present, corresponding to a d spacing of 13.0 Å. Interestingly, the

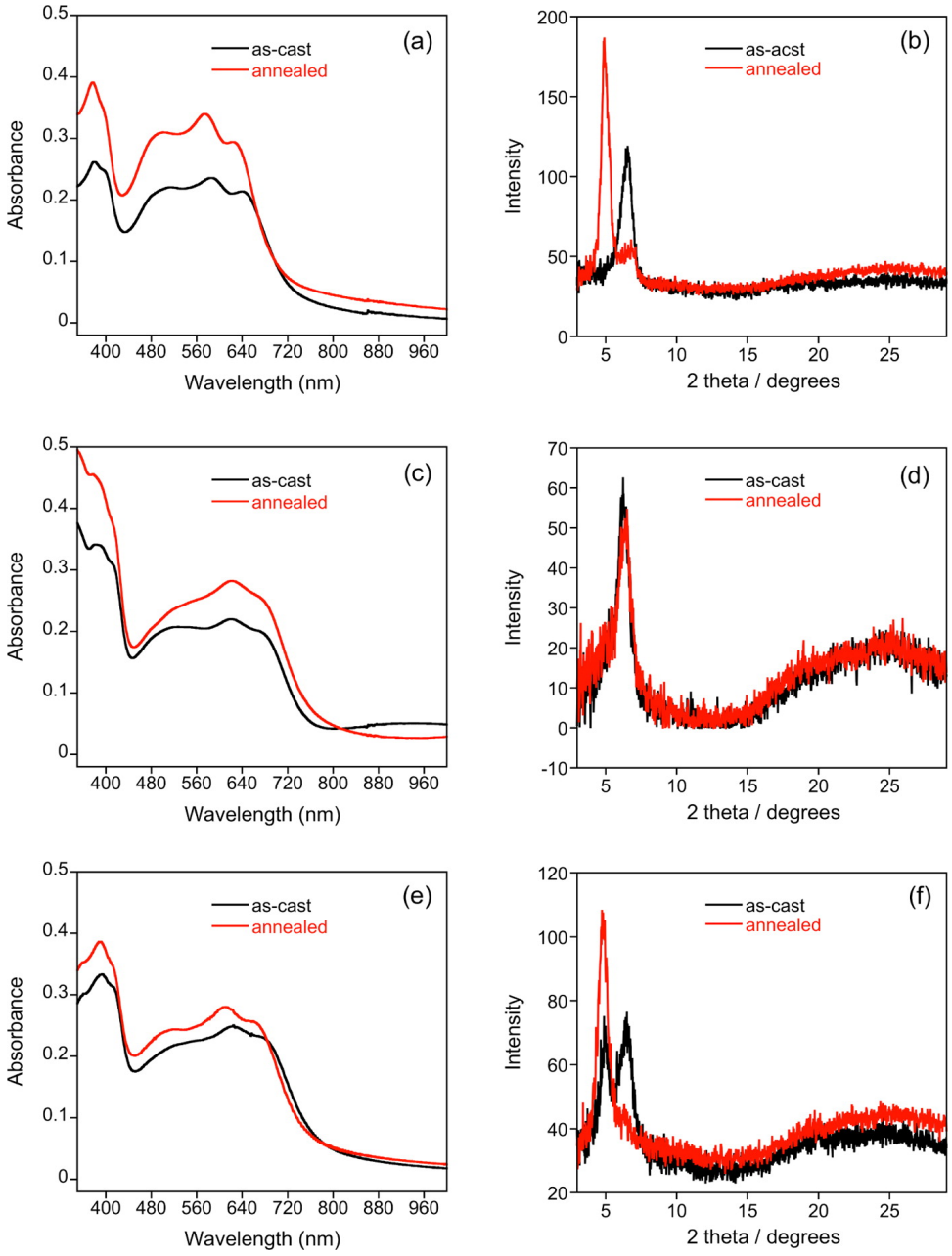

Figure 2.8: UV–vis and GIXRD spectra: (a and b) **1**/$PC_{71}BM$, spin-coated at 80 °C; (c and d) **2**/$PC_{71}BM$, spin-coated 80 °C; (e and f) **2**/$PC_{71}BM$ spin-coated at room temperature. The ratio of [**1** or **2**]/$PC_{71}BM$ is 1.5:1 (*w/w*). For the XRD samples, films were spin-coated on PEDOT:PSS/ITO substrates, and for the UV–vis spectra, films were spin-coated on glass. Reprinted with permission from reference.[11] Copyright 2015 by American Chemical Society.

GIXRD spectra of annealed devices of **1**/$PC_{71}BM$ cast at 80 °C show significant changes, while the GIXRD spectra of annealed devices of **2**/$PC_{71}BM$ cast at 80 °C remain essentially unchanged. Specifically, a new reflection at 2θ = 4.8° appears in **1**/$PC_{71}BM$ (corresponding to a d spacing of 18.4 Å). It is possible that these two different d spacings correspond to the primary reflections from crystalline polymorphs of the small molecule. In this case, we would expect the more energetically stable, more compact (smaller lattice parameter) crystal structure to remain after annealing. However, the opposite trend is observed, which strongly suggests that the different d spacings do not correspond to different crystal structures. A likely explanation for the observed change in the GIXRD spectra is related to the relative orientations of the crystalline grains, which rotate to more energetically favorable configurations upon annealing.[251,252] As such, the measured 13.0 and 18.4 Å *d* spacings likely correspond to two different in-plane lattice spacings. A proposed structure is shown in Figure 2.9a, where the 13.0 Å spacing corresponds to ethylhexyl chain packing and the 18.4 Å spacing to hexyl chain packing. We see that the molecular backbone packing distance of 18.4 Å is less than the length of the molecule along the alkyl side-chain direction, which is unsurprising given that an interdigitated configuration is expected to be energetically more stable because the small molecules would be efficiently packed.[253] Unfortunately, many attempts to grow single crystals of these two compounds for XRD failed.

The proposed reorientation of the small-molecule crystal grains upon annealing

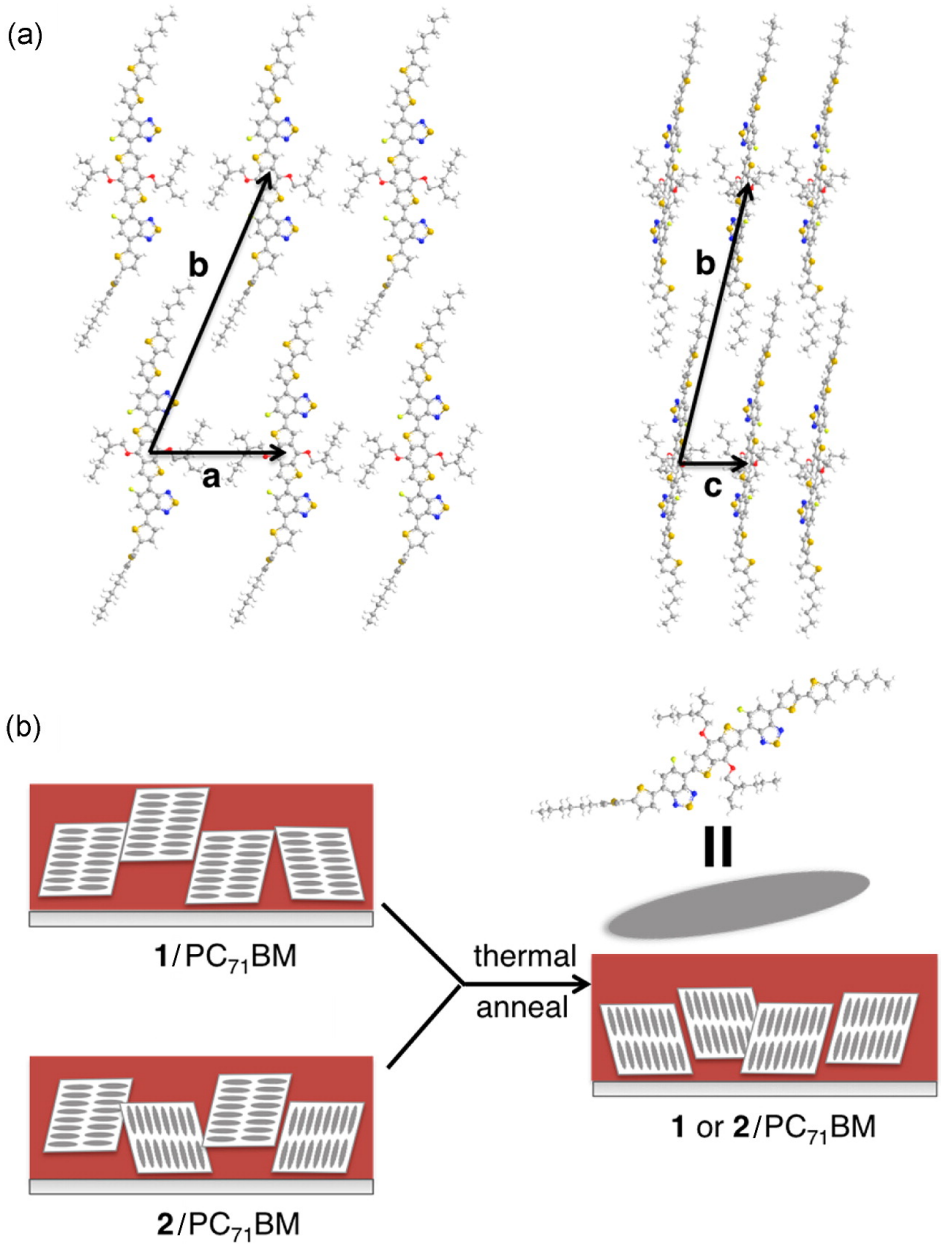

Figure 2.9: (a) Illustration showing the proposed crystal packing of the small molecules **1** and **2** in the BHJ. The unit cell is described by the lattice vectors a–c: a, ethylhexyl chain-packing direction, *d* spacing 13.0 Å; b, hexyl chain-packing direction; *d* spacing 18.4 Å; c, π–π stacking. (b) Proposed reorientation of the small-molecule crystal grains, in the BHJ, upon annealing. Reprinted with permission from reference.[11] Copyright 2015 by American Chemical Society.

is depicted schematically in Figure 2.9b. In the case of **1**/$PC_{71}BM$, before annealing (as-cast), the conjugated backbone of **1** is parallel to the substrate and the incident X-rays, which explains why the feature corresponding to a *d* spacing of 18.4 Å is not observed by GIXRD (Figure 2.9b). Upon thermal annealing, almost all of the grains reorient such that the interdigitated planes of the crystallites of 1 are parallel to the substrate, with the molecular backbones close to perpendicular, and hence the feature at 18.4 Å dominates the GIXRD spectrum. A possible driving force for this observed reorientation of the crystal grains is a lower surface energy of the interdigitated orientation at the buried PEDOT:PSS/ITO interface.[17,102,254] For devices of **2**/$PC_{71}BM$ cast at room temperature, we see that the GIXRD spectra contain both reflections at 13.0 and 18.4 Å, which suggests that both grain orientations are present.[102] Similar to the **1**/$PC_{71}BM$ devices cast at 80 °C, after annealing most of the grains reorient such that the hexyl chains are packed parallel to the substrate. It is noted that the GIXRD data are consistent with the UV–vis absorption data, where films that underwent crystal reorientation upon annealing (**1**/$PC_{71}BM$ spin-coated at 80 °C and **2**/$PC_{71}BM$ spin-coated at room temperature) show a small blue shift (Figure 2.8a,e), which could be due to H-aggregation.(60) Conversely, films that did not undergo crystal reorientation (**2**/$PC_{71}BM$ spin-coated from 80 °C) showed no shift in the UV–vis spectrum (Figure 2.8c). Much like the UV–vis data, we see that there is little correlation between the GIXRD spectra and the device performance; devices of **1**/$PC_{71}BM$ and **2**/$PC_{71}BM$ spin-coated at 80 °C have similar GIXRD spectra, but the **2**/$PC_{71}BM$ devices have nearly double

the PCE. Following annealing, **1**/$PC_{71}BM$ exhibits a significant change in the grain reorientation, with no corresponding change in the device performance. Conversely, annealing of **2**/$PC_{71}BM$ cast at 80 °C displays no change in the GIXRD spectrum and no change in the device performance. Last, devices of **2**/$PC_{71}BM$ cast at room temperature have grains in both orientations, which reorient to the hexyl chain configuration after annealing, where a substantial increase in the PCE is observed.

Another possible mechanism to explain the GIXRD spectrum is depicted in Figure 2.10. The two *d* spacing observed correspond two possible lamellar packing distances differentiated by the status of molecule side chain. In the case of **1**:$PC_{71}BM$, before annealing, the side chains of the molecules are not fully relaxed, instead deforming and freezing in the crystallite domain, resulting a smaller *d* spacing of 13.0 Å. Upon thermal annealing, the molecule side chains undergo relaxation, reaching a more thermal stable status, hence the feature at 18.4 Å dominates the spectrum. A similar phenomenon is observed for **2**:$PC_{71}BM$ spin-casted at room temperature, the difference is that before annealing both status of side chain are present in the BHJ. Upon thermal annealing, all the side chains stretched out into a low energy configuration, so that the feature corresponding to 13.0 Å disappeared. The meta-stable status with squeezed side chains is seen dominating in the high-temperature processed samples, which can be explained by the fact that high temperature results in faster solvent evaporation, hence shorter time for the molecules to reach thermal-stable status.

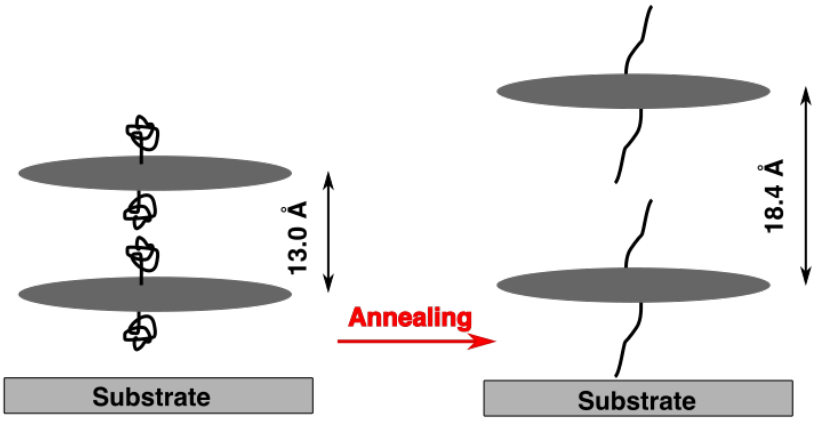

Figure 2.10: Possible mechanism of lamellar stacking in the as-casted and annealed BHJ.

From these UV–vis and GIXRD data, we see that the observed changes in the local structure (optical properties, crystallinity, and orientation) have little impact on the device performance. This suggests that the morphology of the BHJ (i.e., the spatial distribution of the small-molecule and $PC_{71}BM$ phases) plays an important role in the device performance. Shown in Figure 2.11 are the AFM micrographs of the as-cast devices (room temperature and 80 °C) and the annealed devices (80 °C). As-cast devices of **1**/$PC_{71}BM$ have a coarse surface morphology (micron-scale domains) with a root-mean-square (rms) roughness of 2.6 nm, with minimal further coarsening of the features upon thermal annealing at 80 °C for 2 min (rms roughness of 4.0 nm). As-cast devices of **2**/$PC_{71}BM$ at 80 °C appear to have a less coarse morphology than the **1**/$PC_{71}BM$ devices and also exhibit minimal coarsening with annealing. This more idealized distribution of phases within the BHJ morphology is

a likely causative factor for the superior performance of the **2**/$PC_{71}BM$ devices cast at 80 °C. Last, we see that the devices of **2**/$PC_{71}BM$ cast at room temperature have a very fine morphology (rms roughness of 1.3 nm) but undergo significant coarsening of domain sizes after annealing, which are on the order of ~10–20 nm. Given that these domain sizes are ideal for exciton diffusion and dissociation in BHJs, this is likely the origin of the improved efficiency upon annealing of the room temperature cast **2**/$PC_{71}BM$ devices.

Taking all of the above characterization results into consideration, we see that the most profound influence on the device performance of single-atom substitution is the change in the small-molecule solubility. Despite subtle differences in the optical properties and energy levels (the typical parameters considered in the design of new small molecules or polymers for OPV devices), there are large differences in the device performance, which we propose is a result of the different BHJ morphologies. These differences in morphology (despite identical processing conditions) are likely a result of large differences in solubility between **1** and **2**. Given that **1** has a much lower solubility than **2**, we would expect a much coarser and poorly distributed morphology because the small molecules will solidify much sooner than $PC_{71}BM$. In addition, the greater solubility of **2** allows for a greater range of processing parameters (i.e., casting temperature), which ultimately results in improved device performance as result of the increased morphological control.

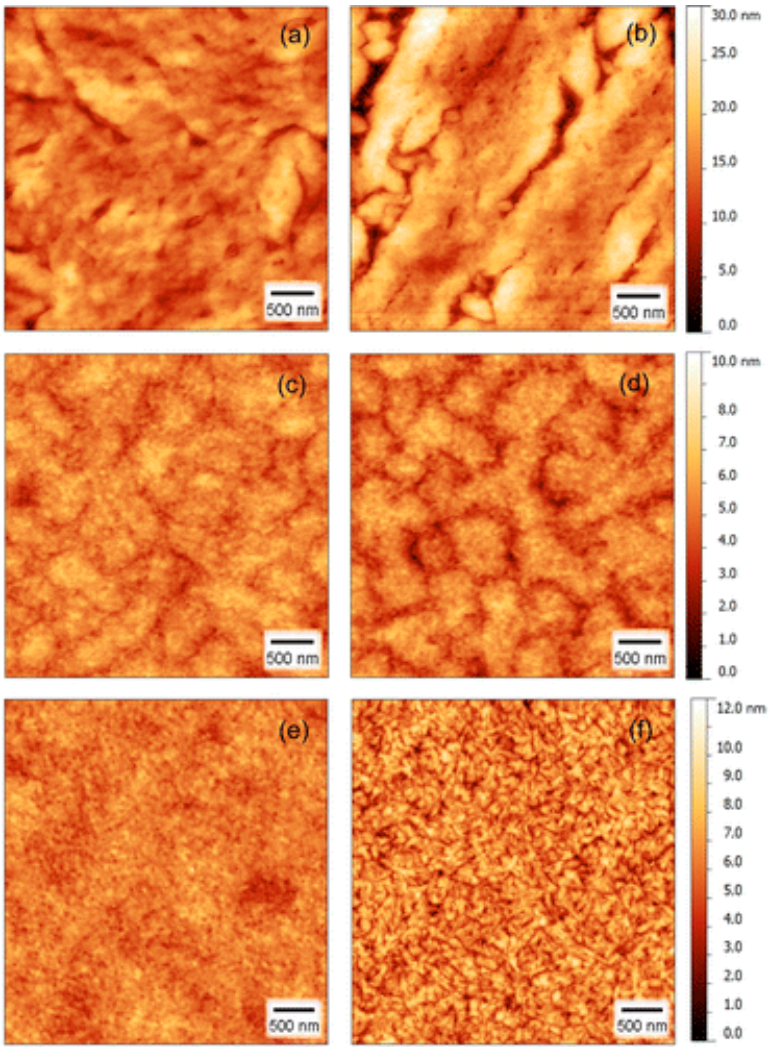

Figure 2.11: AFM topographic images: (a and b) **1**/$PC_{71}BM$, spin-coated at 80 °C; (c and d) **2**/$PC_{71}BM$, spin-coated 80 °C; (e and f) **2**/$PC_{71}BM$ spin-coated at room temperature. Images on the left (a, c, and e) correspond to the as-cast films and those on the right (b, d, and f) to the thermally annealed samples (80 °C for 2 min). Scan size: 4 × 4 μm^2. The ratio of [**1** or **2**]/$PC_{71}BM$ is 1.5:1 (*w/w*), and films were spin-coated on PEDOT:PSS/ITO substrates. Reprinted with permission from reference.[11] Copyright 2015 by American Chemical Society.

2.3 Conclusions

In conclusion, two low-band-gap conjugated small molecules, **1** (E_g = 1.7 eV) and **2** (E_g = 1.6 eV), were synthesized, characterized, and incorporated into OPV devices. While the one-atom variation, S for Se, in these two small molecules did result in small changes with respect to electronics (i.e., band structure, band gap), the observed differences in the OPV device performance were shown to be far more dependent upon morphological differences in the resulting BHJ film when paired with $PC_{71}BM$. Overall, while the current research in heteroatom engineering is an effective and important approach toward the development of higher-efficiency organic solar cells, attention needs to be paid to seemingly mundane but critical details, such as the solubility, solid-state crystallization, and packing, and the resulting morphology within the device and not simply electronic considerations.

2.4 Experimental Section

2.4.1 Materials and Methods

S1,[135] **S5**,[135] and **S7**[237] were prepared according to reported procedures. Detailed synthetic procedures for **S2**, **S3**, and **S6** are described below. Tetrahydrofuran (THF) and toluene were purified using a pure solvent purification system prior to use. All other reagents were used as received. All reactions were carried out under an inert atmosphere using standard Schlenk techniques or in a glovebox. ^{1}H,

^{13}C, and ^{19}F NMR spectra were recorded on a Varian Inova-400 or VNMRS-500 spectrometer. Mass spectra were obtained on an Agilent 6220 spectrometer. Mass spectra were obtained on an Agilent 6220 spectrometer or Bruker Ultraflextreme MALDI TOF/TOF system (Bruker Daltonics, Bremen, GmbH). Elemental analyses were performed by the Analytical and Instrumentation Laboratory at the University of Alberta.

UV–vis measurements were performed using Varian Cary 300 Scan and PerkinElmer Lambda 1050 spectrophotometers. TGA and DSC were carried out on PerkinElmer instrument under a nitrogen flow at a heating rate of 10 °C min^{-1}. GIXRD was performed using a Bruker D8 Discover instrument with a Cu Ka beam (40 kV, 40 mA; λ = 1.541784 Å, angle of incidence = 0.3°). Theoretical calculations were carried out at the B3LYP/6-31G(d) level using the Gaussian 03 suite of programs.[248] AFM was performed in tapping mode on a Digital Instruments/Veeco multimode tapping atomic force microscope, and the collected data were analyzed using the open source software Gwyddion.

2.4.2 OPV Device Fabrication and Testing

OPV devices consisted of the following architecture: ITO/PEDOT:PSS/active layer/ LiF/Al/Mg, where the photoactive layer consists of a BHJ formed from either **1**/$PC_{71}BM$ or **2**/$PC_{71}BM$. ITO-coated glass substrates were cleaned via sequential 10 min ultrasonication in methylene chloride, distilled water, and isopropyl alcohol, followed by a 10 min air plasma with a Harrick plasma cleaner (0.1 Torr, PDC 32G,

18 W). PEDOT:PSS (Heraeus Clevios PVP AI 4083) was filtered with a 0.2 μm cellulose acetate filter directly onto the freshly cleaned ITO substrates and spin-coated at 3000 rpm for 1 min to form a ∼30-nm-thick layer, which was annealed in air for 10 min at 120 °C. The active layer was spin-coated from a CB solution in air. The **2**/$PC_{71}BM$ blend was filtered through a 0.2 μm polytetrafluoroethylene filter before spin coating directly onto the freshly annealed PEDOT:PSS layer (on ITO). The **1**/$PC_{71}BM$ blend was spin-coated at 80 °C because of its lower solubility; 80 °C refers to the temperature of the solution, and the underlying substrate is at room temperature. The top Al (20 nm) and Mg (60 nm) cathodes were deposited by thermal evaporation under high-vacuum conditions ($\sim 5 \times 10^{-6}$ Pa) at rates of ∼2 and 2.5 Å/s, respectively. The device area was 0.155 ± 0.008 cm^2. After thermal deposition of the top contacts (Al and Mg), the cells were loaded into vials in a nitrogen-filed glovebox (one set of five devices per vial), sealed, and then immediately removed from the glovebox for testing. Devices were taken out of the nitrogen-filled vials one set at a time, then rapidly loaded onto the testing platform, and inserted into a custom-made environmental chamber, with an environment consisting of room temperature, dry flowing nitrogen (air exposure <5 s total during this process). The photovoltaic characteristics of the OPV devices were characterized under simulated AM 1.5G conditions (xenon source from Oriel 91191, 1000 W), equipped with a custom-made water filter and calibrated to a certified Si reference cell with a KG-5 filter (PV Measurements, PVM624). The light intensity was then subsequently measured immediately preceding any J–V

curve accumulation using a thermopile (XLP12-3S-H2). J–V characteristics were recorded using a computer-controlled Keithley 2400 source meter. A minimum of three separate sets of five devices were averaged for a data point. The plus/minus values represent the standard deviation.

2.4.3 General Synthesis for 1 and 2

Synthesis of 1,2-diamino-3,6-dibromo-4-fluorobenzene (S2).

Compound S1 (2.00 g, 6.41 mmol) and ethanol (50 mL) were added to a three-necked round-bottom flask and cooled to 0 °C. After addition of $NaBH_4$ (4.6 g, 0.12 mol) was slowly added, the reaction mixture was stirred overnight at room temperature. After removal of the volatiles 100 mL distilled water was added to the reaction mixture and then the mixture was extracted with ether, washed with brine, dried over anhydrous Na_2SO_4. Volatiles were removed from the extract to obtain **s2** as a yellow powder (1.20 g, 66 %). ^{1}H NMR (500 MHz, $CDCl_3$): δ 6.80 (d, 1H, *J* = 7.8 Hz, Ar), 4.14 (s, 2H, NH), 3.62 (s, 2H, NH). ^{13}C (125 MHz, $CDCl_3$): δ 95.7 (d) 108.7 (d), 109.4 (d), 128.8, 135.8, 153.2 (d). ^{19}F NMR (376 MHz, $CDCl_3$): δ -116.1 (d). HRMS (EI) m/z calc. for $C_6H_5N_2BrBrF$ (283.87830); Found 283.8784.

Synthesis of 4,7-dibromo-5-Fluorobenzo[c][1,2,5]seleno-diazole (S3).

A solution of compound **S2** (1.02 g, 3.61 mmol) in 30 mL of ethanol was heated to refluxed in a three-necked round-bottom flask with stirring. Afterwards, a solution

of SeO_2 (0.402 g, 3.62 mmol) in 20 mL of hot water was added dropwise. The resulting reaction mixture was refluxed for overnight to obtain a yellow precipitate over pale brown solution. Then, the reaction was cooled to room temperature and precipitate was filtrated, and washed with 5 × 100 mL of ethanol to obtain **S3** as a golden-yellow powder (1.1 g, 85 %). ^{1}H NMR (400 MHz, $CDCl_3$): δ 7.75 (d, 1H, J = 6.8 Hz, Ar). ^{19}F NMR (376 MHz, $CDCl_3$): δ -102.1 (d). HRMS (EI) m/z calc. for $C_6HN_2BrBrFSe$ (359.76352); Found 359.7637.

Synthesis of 4-bromo-5-fluoro-7-(5′-hexyl-[2,2′-bithiophene]-5-yl)benzo[c] [1,2,5]seleno-diazole (S6).

This was prepared according to a reported procedure for the synthesis of **S5**. A mixture of 30 mL of toluene and 20 mL aqueous solution of Na_2CO_3 (2.0 M) was degassed with nitrogen for 25 min. A Schlenk flask was charged with 4, 7-dibromobenzo[c][1,2,5]seleno-diazole (**S3**) (1.48 g, 4.1 mmol) and 5′-hexyl-2,2′-bithiophene-5-boronic acid pinacol ester (**S4**) (1.6 g, 4.2 mmol), and $Pd(PPh_3)_4$ (0.15 g, 0.14 mmol) in a nitrogen atmosphere. The solvent mixture was then transferred under nitrogen to the Schlenk containing reactants and the resulting mixture was then stirred and degassed for 25 min followed by the addition of 3 drop of Aliquat 336. The reaction mixture was heated to 85 °C overnight to obtain a bright red solution, quenched afterwards with water (15 mL). Organic layer was extracted with dichloromethane (50 mL), dried over Na_2SO_4 and then volatiles were removed under reduced pressure to give dark red solid. This crude product

was loaded on a short silica column and eluted with hexanes to remove unreacted pinacol ester starting materials and Aliquat. After eluting the desired product with dichloromethane followed by removal of solvents yielded red solid which contained **S2** as only remaining impurity. Spectroscopically pure **S5** (0.738 g, 34 %) was obtained by removing **S2** from the product mixture by sublimation (70 °C, 0.03 torr). ^{1}H NMR (500 MHz, $CDCl_3$): δ 7.93 (d, *J* = 4.0 Hz, 1H, CH), 7.64 (d, *J* = 10.0 Hz, 1H, CH), 7.15 (d, *J* = 4.0 Hz, 1H, CH), 7.12 (d, *J* = 4.0 Hz, 1H, CH), 6.73 (d, *J* = 3.5 Hz, 1H, CH), 2.82 (t, *J* = 7.8 Hz, 2H, CH2), 1.70 (m, *J* = 7.5 Hz, 2H, CH_2), 1.40 (br m, 2H, CH_2), 1.34 (br m, 2H, CH_2), 1.30 (br m, 2H, CH_2), 0.99 (t, *J* = 7.2 Hz, 3H, CH_3). ^{19}F NMR (376 MHz, $CDCl_3$): δ -103.1. HRMS (EI) m/z calc. for $C_{20}H_{18}N_2BrFS_2Se$ (529.92350); Found 529.92236.

In a nitrogen-filled glovebox, a 20 mL glass tube was charged with **S5** (200 mg, 0.416 mmol) or **S6** (220 mg, 0.416 mmol), **S7** (150 mg, 0.194 mmol), $Pd(PPh_3)_4$ (20 mg, 0.017 mmol), and THF (10 mL) and sealed with a Teflon cap. The reaction mixture was heated to 150 °C for 70 min using a Biotage microwave reactor. Upon cooling to room temperature, 50 mL of CH_2Cl_2 was added to the reaction mixture and then poured into an aqueous solution of sodium diethyldithiocarbamate (1 g/100 mL) and stirred for 12 h at room temperature. Afterward, the organic layer was separated and the volatiles were reduced to ca. 10 mL, followed by precipitated with 100 mL. The dark solids were washed with MeOH (30 mL × 2) and acetone (30 mL) to obtain the pure product as a metallic purple solid. Yield: ca. 80–90%. The syntheses of the precursors for **1** and **2** are described.

Characterization for 1

^{1}H NMR (C_6D_6, 400 MHz, 60 °C): δ 8.88 (s, 2 H; Ar), 7.71 (d, J = 4.0 Hz, 2 H; Ar), 7.32 (d, J = 13.2 Hz, 2 H; Ar), 6.90 (m, 4 H; Ar), 6.42 (d, J = 4.0 Hz, 2 H; Ar), 4.41 (d, J = 5.2 Hz, 4 H; OCH_2), 2.53 (t, J = 8.0 Hz, 4 H; CH_2), 1.95–1.52 (m, 24 H), 1.20 (m, 16 H), 1.05 (t, J = 7.2 Hz, 6 H; CH_3), 0.83 (t, J = 7.2 Hz, 6 H; CH_3). ^{19}F NMR (C_6D_6, 376 MHz, 60 °C): δ −106.5. ^{13}C NMR (C_6D_6, 100.6 MHz, 60 °C): δ 161.1, 158.5, 153.5 (d), 149.5, 145.9, 144.7, 140.7, 136.0, 134.6, 132.9, 132.3, 130.4, 129.1, 124.7, 123.7, 123.3, 115.4, 115.5, 111.1, 75.8, 41.1, 31.4, 31.2, 30.9, 29.9, 29.5, 28.6, 24.2, 23.2, 22.3, 13.9, 13.6, 11.3. HRMS (MALDI). Calcd for $C_{66}H_{72}F_2N_4O_2S_8$ [M]: *m/z* 1246.3389. Found: *m/z* 1246.3375. Elem anal. Calcd for $C_{66}H_{72}F_2N_4O_2S_8$: C, 63.53; H, 5.82; N, 4.49; S, 20.55. Found: C, 63.58; H, 5.83; N, 4.45; S, 20.65.

Characterization for 2

^{1}H NMR (C_6D_6, 400 MHz, 60 °C): δ 8.89 (s, 2 H; Ar), 7.62 (d, J = 4.0 Hz, 2 H; Ar), 7.32 (d, J = 13.6 Hz, 2 H; Ar), 6.97 (m, 4 H; Ar), 6.45 (d, J = 4.0 Hz, 2 H; Ar), 4.42 (d, J = 5.2 Hz, 4 H; OCH_2), 2.54 (t, J = 8.0 Hz, 4 H; CH_2), 1.90–1.10 (m, 24 H), 0.99 (t, J = 7.2 Hz, 6 H; CH_3), 0.82 (t, J = 6.8 Hz, 6 H; CH_3). ^{19}F NMR (C_6D_6, 376 MHz, 60 °C): δ −106.2. ^{13}C NMR (C_6D_6, 100.6 MHz, 60 °C): δ 161.76, 159.21, 158.30 (d), 155.03, 145.67, 144.62, 141.14, 136.41 (d), 134.88, 133.40 (d), 132.33, 130.55 (d), 128.67, 124.72, 123.90 (d), 123.55, 123.03, 115.75 (d), 111.81 (d), 75.68, 41.06,

31.42, 31.22, 30.90, 29.98, 29.49, 28.67, 24.23, 23.27, 22.43, 14.09, 13.69, 11.43. HRMS (MALDI). Calcd for $C_{66}H_{72}F_2N_4O_2S_6Se_2$ [M]: m/z 1342.2278. Found: m/z 1342.2285. Elem. anal. Calcd. for $C_{66}H_{72}F_2N_4O_2S_6Se_2 \cdot CH_3OH$: C, 58.58; H, 5.58; N, 4.08; S, 14.00. Found: C, 58.81; H, 5.60; N, 4.02; S, 13.88.

3

Carboxylate-Functionalized Donor Polymer as an Interfacial Layer to Improve the Efficiency of Polymer Solar Cells

3.1 Introduction

Organic photovoltaics (OPVs) have attracted a great deal of research interest in recent decades.[255] OPVs are an attractive source of renewable energy because of their potential for inexpensive manufacturing, based upon processes such as roll-to-roll printing and spray-coating.[38,63,95,256–264] OPVs also offer the possibility

of harnessing the versatility of organic, macromolecular, and supramolecular chemistry to tailor the characteristics of each component and layer within the cell.[107,109,112,242,265–273] A typical solar cell architecture consists of a light-absorbing BHJ sandwiched between two electrodes;[257,260] in what is now viewed as a conventional forward solar cell structure, optically transparent indium tin oxide (ITO) collects holes at the anode, and a reflective metal cathode collects the electrons. Interfacial layers are used in various locales within an OPV device where they play a number of essential roles, including matching or alignment of energy levels (for instance between the BHJ and an electrode surface), blocking electrons and/or holes to prevent recombination, adjusting of surface energetics and work function, and influencing the formation of gradients within the BHJ.[132,137,172,176,177,255,274,275]

As an interfacial layer on the transparent ITO electrode, PEDOT:PSS is a widely used material that smooths the rough ITO surface while acting as an electron blocking layer.[168–172] PEDOT:PSS has a number of advantageous features, including its high electrical conductivity, transparency to visible light, and resistance to the organic solvents used for the subsequent deposition and processing of the BHJ.[137,174,276,277] PEDOT:PSS has, however, a number of well-documented problems, including its acidic nature,[278,279] the presence of ions (sodium ions in particular),[280,281] and its intrinsic hydrophilicity,[279,282] which renders it chemically dissimilar from the hydrophobic BHJ.[257,283–286] While some endeavor to replace the PEDOT:PSS entirely,[176–180] another approach that

takes advantage of the favorable properties of the well-studied PEDOT:PSS/ITO electrode while mitigating disadvantages, is to include a thin overlayer on top of the PEDOT:PSS.[12–14] The examples are shown in Figure 3.1. For instance, Meng and co-workers synthesized a phosphonated polymer called PCDTBT-Pho, based upon the widely used low band gap polymer PCDTBT, which they then sandwiched between the PEDOT:PSS and the BHJ that was composed of PCDTBT and $PC_{71}BM$. They observed an increase of power conversion efficiency (PCE) from 5.6% to 6.0%, which was attributed to increased crystallization of the donor polymer and favourable vertical composition profile of the BHJ. No mention was made, however, of an effect related to energy level alignment within the stack.[13] Zhang and co-workers examined the influence of a thin surfactant layer of glycerol monostearate on PEDOT:PSS electrodes (glass only, no ITO) with BHJs that consisted of $PC_{61}BM$ or $PC_{71}BM$, and P3HT, PTB7, or PCDTBT, and noted a large increase of conductivity of the PEDOT:PSS (3 orders of magnitude). The power conversion efficiencies of these ITO-free devices were comparable to that of untreated PEDOT:PSS on ITO.[4]

Modification of the PEDOT:PSS by addition of a thin overlayer would be expected to affect both the energy level alignment relative to the BHJ, as well as resulting phase segregation and possible gradients of the donor polymer and acceptor fullerene within the BHJ, which are in intimate contact with this PEDOT:PSS modifier. Altering the interfacial layer would be expected to affect the energy levels and morphology of the BHJ simultaneously, complicating an

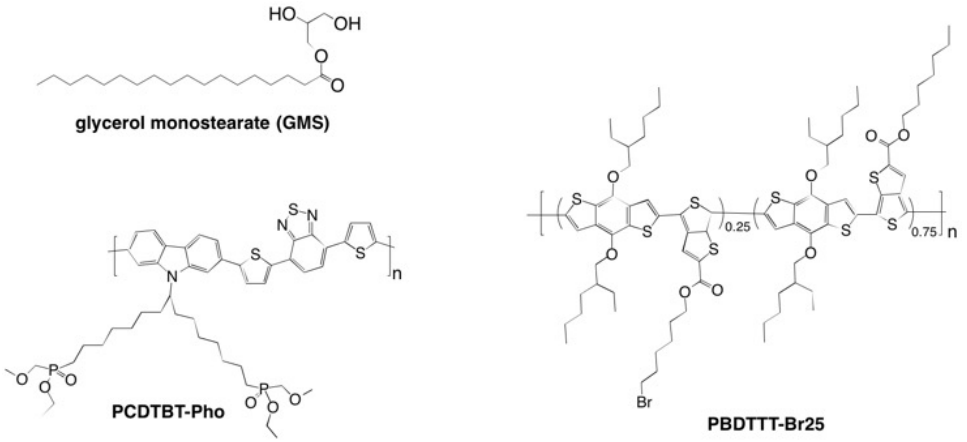

Figure 3.1: Examples of reported surface modifiers on PEDOT:PSS: GMS,[12] PCDTBT-Pho,[13] PBDTTT-Br25.[14] Reprinted with permission from reference.[15] Copyright 2015 by American Chemical Society.

understanding of the underlying factors affecting device performance. In an attempt to deconvolve these two important parameters, we synthesized a low band gap interfacial modifier based upon PBDTTPD with an appended carboxylic acid-based side chain, called PBDTTPD-COOH here (Figure 3.2),[266] to take advantage of the strong interaction of carboxylic acids with the positively charged PEDOT in PEDOT:PSS.[287] Forward devices composed of 3 different types of polymer/fullerene BHJs were prepared with and without the PBDTTPD-COOH on the PEDOT:PSS. Using rigorous statistical analyses of the performance of these organic solar cells, it was found that the PBDTTPD-COOH interfacial layer improved the PCE of two of the polymer/fullerene blends, but not the third. In order to understand the origin of the efficiency enhancement (and lack thereof) of the PBDTTPD-COOH interfacial layer, the electronic energy level alignment between the polymers and the PBDTTPD-COOH layers was determined (using ultraviolet

photoelectron spectroscopy (UPS)), as well as morphologies and composition of the BHJs (atomic force microscopy (AFM), time of flight secondary ion mass spectroscopy (ToF-SIMS) depth profiling, X-ray diffraction (XRD) and contact angle goniometry). From these results it was found that all of the studied polymers had favourable energy level alignment with respect to the interfacial layer,the primary effect of the PBDTTPD-COOH interfacial layer was, however, to modify the surface energy of the anode interface, which resulted in a more favourable vertical composition profile within the BHJ.

3.2 Results

The carboxylic acid-functionalized PBDTTPD polymer, PBDTTPD-COOH, was synthesized as depicted in Figure 3.2. As can be seen from the UV-visible transmission spectrum in Figure 3.3a of PBDTTPD-COOH in both solution and film, there is an absorption maximum centred about 670 nm. The absorption edge of PBDTTPD-COOH at 688 nm suggests a band gap of 1.80 eV, which is very close to the parent PBDTTPD polymer (1.81 eV).[112] Ultraviolet photoelectron spectroscopy allowed for determination of the highest occupied molecular orbital, the HOMO, and thus with the band gap gleaned from the UV-Vis spectra, the HOMO and LUMO levels of PBDTTPD-COOH were calculated to be 5.40 and 3.60 eV, respectively. A solution of PBDTTPD-COOH was spin cast (10:1 $CHCl_3$:DMSO, 0.05 mg/mL, 1000 rpm for 60 s) onto a 30 nm thick layer of PEDOT:PSS on

ITO. Figure 3.3b shows the UV-vis transmission spectrum of this thin layer of PBDTTPD-COOH layer on PEDOT:PSS/ITO, where an absolute decrease of 5-10% transmission was observed between 380-680 nm, corresponding to a 3-4 nm thick layer of PBDTTPD-COOH. The thickness of a single layer PBDTTPD-COOH thickness was calculated by comparing UV-visible spectroscopy of films of known thicknesses. A thick PBDTTPD-COOH film, A, was spin-cast from CHCl3:DMSO (10:1) solution onto glass substrate and annealed at 120°C for 5 min. UV-vis absorption profile was taken on Film A and the thickness is measured to be 30 nm by AFM scratching/ploughing. A single layer of PBDTTPD-COOH, B, was spin-cast from 0.05 mg/ml $CHCl_3$:DMSO (10:1) onto glass. Absorption profile of B was taken and compared to that of film A at the absorption maximum (626 nm). In this way, a single layer of PBDTTPD-COOH was calculated to be about 3.6 nm thick, as calculated in Table 3.1. Ideally, any interfacial layer in a solar cell should have low absorption in the UV-visible range to maximize light transmission, and due to the thinness of the PBDTTPD-COOH layer, a small fraction of the light is lost.

AFM micrographs of the ITO/PEDOT:PSS layers, with and without the 3-4 nm thick PBDTTPD-COOH layer, are shown in Figure 3.4. The root-mean-squared roughness of the film increased slightly upon the inclusion of the PBDTTPD-COOH layer, from 1.3 to 1.6 nm. Subtle differences of appearance of the phase images (Figure 3.4b vs 3.4d) may suggest a more uniform surface composition upon addition of the PBDTTPD-COOH layer.

The effects of using a PBDTTPD-COOH interfacial layer on PEDOT:PSS

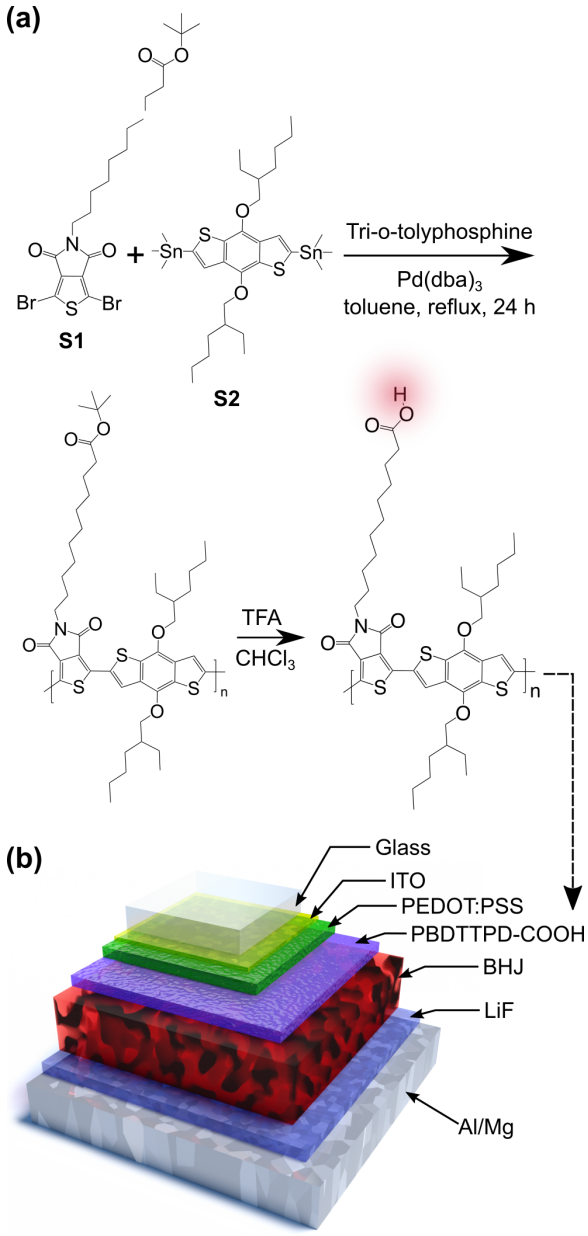

Figure 3.2: (a) Synthesis of acid-functionalized PBDTTPD polymers. (b) Forward device architecture: ITO/PEDOT:PSS/(PBDTTTPD:COOH)/ polymer:$PC_{71}BM$ BHJ/LiF/Al/Mg. Reprinted with permission from reference.[15] Copyright 2015 by American Chemical Society.

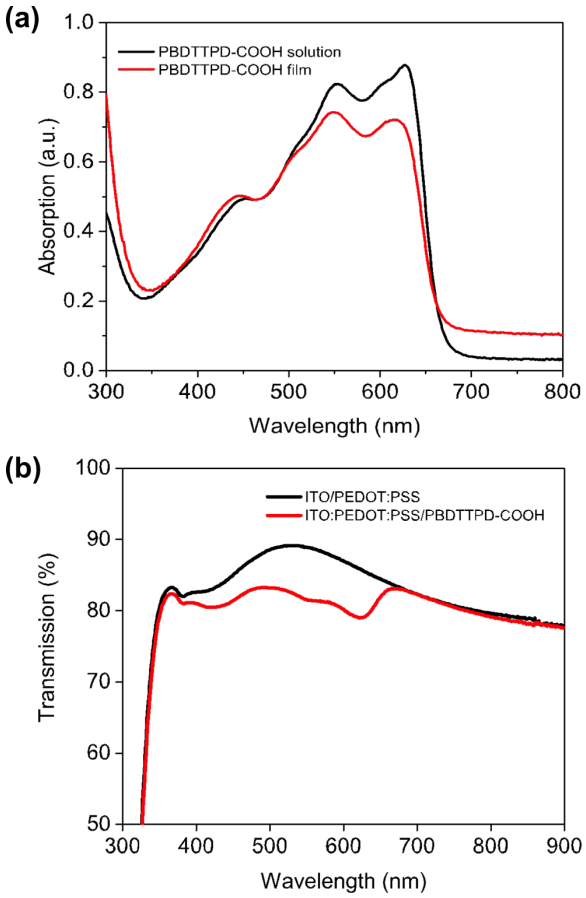

Figure 3.3: Normalized UV-vis spectrum of PBDTTPD-COOH solution and thin film. The thin film is spun-cast at 1000 rpm on a glass slide from a 10 mg/mL solution dissolved in $CHCl_3$/DMSO (10:1). (b) Transmission spectrum of a ITO/PEDOT:PSS substrate (black) and a ITO/PEDOT:PSS/PBDTTPD-COOH substrate (red). Reprinted with permission from reference.[15] Copyright 2015 by American Chemical Society.

Table 3.1: Calculation of PBDTTPD-COOH film thickness.

	Film A	Film B
Absorption (a.u.)	0.333	0.048
Transmittance (a.u.)	0.667	0.952
Absorbance (a.u.)	0.176	0.021
Thickness (nm)	30	3.6

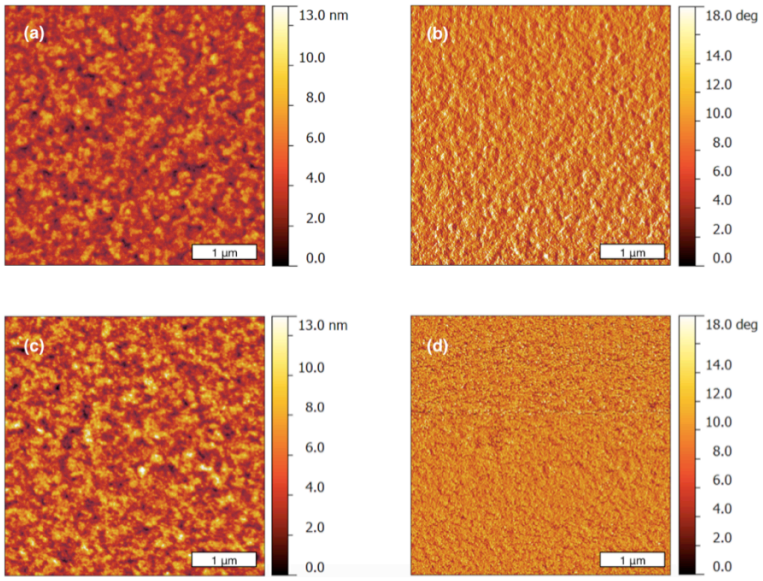

Figure 3.4: AFM images of (a-b) ITO/PEDOT:PSS, with a calculated rms value of 1.3 nm; (c-d), ITO/PEDOT:PSS/PBDTTPD-COOH surface with a calculated rms of 1.63 nm. Conditions: The PEDOT:PSS layer was prepared via spin casting and annealing at 3000 rpm, 60 s, and annealed at 120 °C for 10 min; the PBDTTPD-COOH layer on top of the ITO/PEDOT:PSS was spin-cast from 0.05 mg/mL $CHCl_3$:DMSO (10:1), 1000 rpm, 60 s, and annealed at 120 °C for 5 min. Reprinted with permission from reference.[15] Copyright 2015 by American Chemical Society.

in organic solar cells were investigated in a forward-mode architecture with the following stack: ITO/(interfacial layer or layers)/BHJ/LiF/Al/Mg. Shown in Figure 3.5 are the chemical structures of different donor polymers used in this work, and the corresponding energy diagrams of all the different layers of these OPV stacks. As control experiments, two series of cells needed to be made: (i) 'unmodified' cells with a standard PEDOT:PSS interfacial layer between the ITO and BHJ, and (ii), 'unmodified' cells as described in (i) except that the ITO/PEDOT:PSS films were prepared and then treated via spin-coating with the same solvent combination from which the PBDTTPD-COOH layer was cast ($CHCl_3$:DMSO 10:1, same spin-coating conditions). The $CHCl_3$:DMSO treatment of the PEDOT:PSS, the second set of control experiments, was necessary since it has been shown that DMSO can increase the conductivity of a PEDOT:PSS film, which could influence the efficiency of the solar cells.[288–290] The results of these two sets of control experiments were compared to ITO/PEDOT:PSS/PBDTTPD-COOH electrodes, with the PBDTTPD-COOH cast from $CHCl_3$:DMSO. The results of these experiments, with accompanying statistical analyses, are shown in Table 3.2, and J-V curves of champion devices are depicted in Figure 3.6. The quantity of data in Table 3.2, and accompanying statistics, do not lend themselves to easy interpretation, to simplify understanding, we have represented the data graphically in Figure 3.7.

To clearly represent the distribution of the performances of these organic solar cells, we make use of average shifted histograms (ASHs).[291] Figure 3.7a shows a

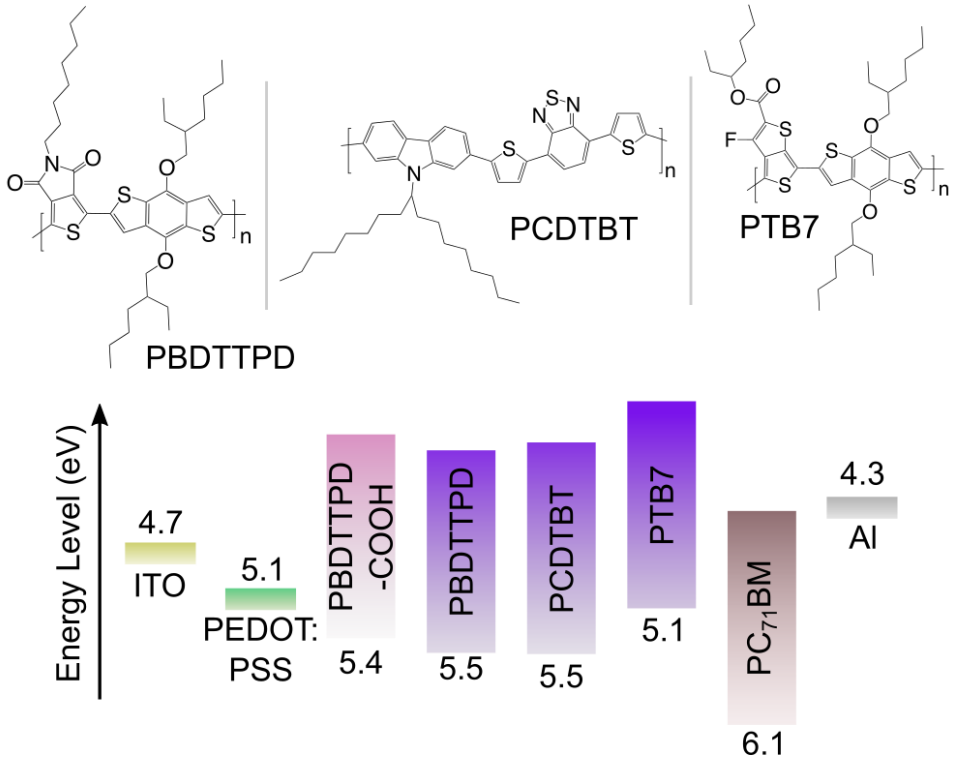

Figure 3.5: Chemical structures of donor polymers used in this work. Corresponding energy levels of all the materials found in the OSC stacks of these BHJ devices. Reprinted with permission from reference.[15] Copyright 2015 by American Chemical Society.

representative example of average shifted histograms, which are density estimations of the distribution of power conversion efficiencies for sets of devices fabricated under identical experimental conditions. Compared to traditional histograms, an ASH avoids two of the three variables in a histogram, bin position and range. This representation helps eliminate artifacts in the distribution that may be introduced due to poor or arbitrary choices of these parameters. The only input variable for constructing an ASH is the bin width, which is determined by the bandwidth of the dataset, using Scott's normal reference rule.[292] The background infill is obtained by overlaying all the histograms corresponding to different shifted origins used in the averaging. The solid line is the resultant average for all the shifted histograms. The small vertical lines underneath the ASH distribution are a plot showing the actual position of each data point, known as a "rug" plot.

Although these average shifted histograms are a useful visual tool for evaluating and comparing the performance of solar cell devices, it is necessary to quantify if modifications to the solar cell architecture result in statistically significant differences in performance. In our previous work we proposed such a protocol, where the p-value of a given set of devices is measured relative to some reference set of devices.[293] Further extending this idea, we use a K-sample Anderson-Darling test to determine if two sets of device data are statistically distinguishable from each other.[294] In this way, if the p-value of the Anderson-Darling test is below some significance value (typically 5%), we can reasonably conclude that the two different sets of devices have measurably different device performances.

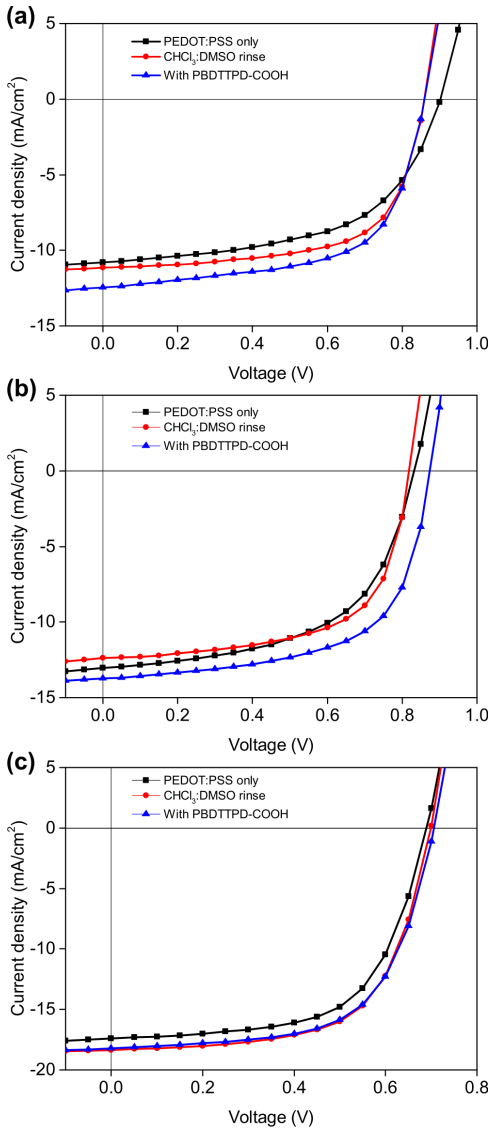

Figure 3.6: J-V curves of champion devices of polymer:$PC_{71}BM$ solar cells fabricated with PEDOT:PSS only, a $CHCl_3$:DMSO (10:1) rinse and with a PBDTTPD-COOH interfacial layer. Corresponding BHJs are: (a) PBDTTPD:$PC_{71}BM$, (b) PCDTBT:$PC_{71}BM$ and (c) PTB7:$PC_{71}BM$. Reprinted with permission from reference.[15] Copyright 2015 by American Chemical Society.

Shown in Figure 3.7b are the average shifted histograms of J_{SC}, V_{OC}, FF and PCE for sets of PBDTTPD:$PC_{71}BM$ solar cells with a PBDTTPD-COOH interfacial layer compared to devices without a PBDTTPD-COOH interfacial layer but the PEDOT:PSS layer has been rinsed with $CHCl_3$:DMSO. Likewise, these data are shown in Figures 3.7c and 3.7d for PCDTBT:$PC_{71}BM$ and PTB7:$PC_{71}BM$ solar cells, respectively.

As a starting point for discussion, the device performance metrics for ITO/(interfacial layers)/PBDTTPD:$PC_{71}BM$/LiF/Al/Mg devices are shown in entries 1-3 in Table 3.2. With respect to the two sets of control experiments, entries 1 and 2, the power conversion efficiency (PCE) increased from 5.6 ± 0.5% to 6.1 ± 0.2% when the standard ITO/PEDOT:PSS electrode was treated with $CHCl_3$:DMSO, which is mostly strongly correlated to an increase in FF from 0.55 ± 0.06 to 0.64 ± 0.01. Modifying the electrode to include the PBDTTPD-COOH interfacial layer, ITO/PEDOT:PSS/PBDTTPD-COOH, resulted in a further increase of the PCE to 6.4 ± 0.3%, concomitant with an increase in J_{SC}. The graphical representation of the full suite of devices tested is shown in Figure 3.7b, and the 'best' devices as J-V plots, and as average-shifted histograms are shown in Figure 3.6a. The p-values, shown in each plot in Figure 3.7b, reveal that the increases in PCE and J_{SC} upon inclusion of the PBDTTPD-COOH modifier are experimentally distinguishable (p = 0.33% and 0.02%, respectively),these data also reveal a decrease in FF (p = 0.10%) due to the PBDTTPD-COOH modifier, and show that the V_{OC} is unaffected (p = 58%).

A similar trend was observed for cells with the PCDTBT:$PC_{71}BM$ BHJ, as shown in Table 3.2. Starting with the two sets of control experiments, the PCE increased from 5.6 ± 0.4% to 6.0 ± 0.4% upon treatment of the standard ITO/PEDOT:PSS electrode with $CHCl_3$:DMSO (again, the additional spin-coating step), due to an increase of FF from 0.54 ± 0.02 to 0.61 ± 0.01 (entries 4 and 5). Addition of the PBDTTPD-COOH interfacial layer led to an increase in PCE to 6.5 ± 0.5% (entry 6 in Table 3.2), due to an increase of the J_{SC} and the V_{OC} accompanied by a small decrease of the FF. The visual representation of the data, the J-V plots and the ASH plots, are shown in Figures 3.6b and 3.7c; the resulting increase of PCE is small but experimentally distinguishable (p = 2.4%).

The third donor-acceptor bulk heterojunction screened, PTB7:$PC_{71}BM$, showed different behavior (Table 3.2, Figure 3.6c, and Figure 3.7d). The standard ITO/PEDOT:PSS electrode was treated with the $CHCl_3$:DMSO spin-coating step, which resulted in an increase of PCE from 7.1 ± 0.3% to 7.4 ± 0.7%. Addition of the PBDTTPD-COOH modifier to the ITO/PEDOT:PSS electrode showed no statistically significant increase in any of the measured properties of the solar cell (FF, J_{SC}, V_{OC}, PCE), as can be seen from the average shifted histograms in Figure 3.7d.

To summarize the results of the OPV solar cell study, inclusion of the PBDTTPD-COOH modifier to the ITO/PEDOT:PSS electrode improved the PCE of both the PBDTTPD/$PC_{71}BM$ and PCDTBT/$PC_{71}BM$ organic solar cells, but was found to have no effect on the PTB7/$PC_{71}BM$ devices. As such, the question

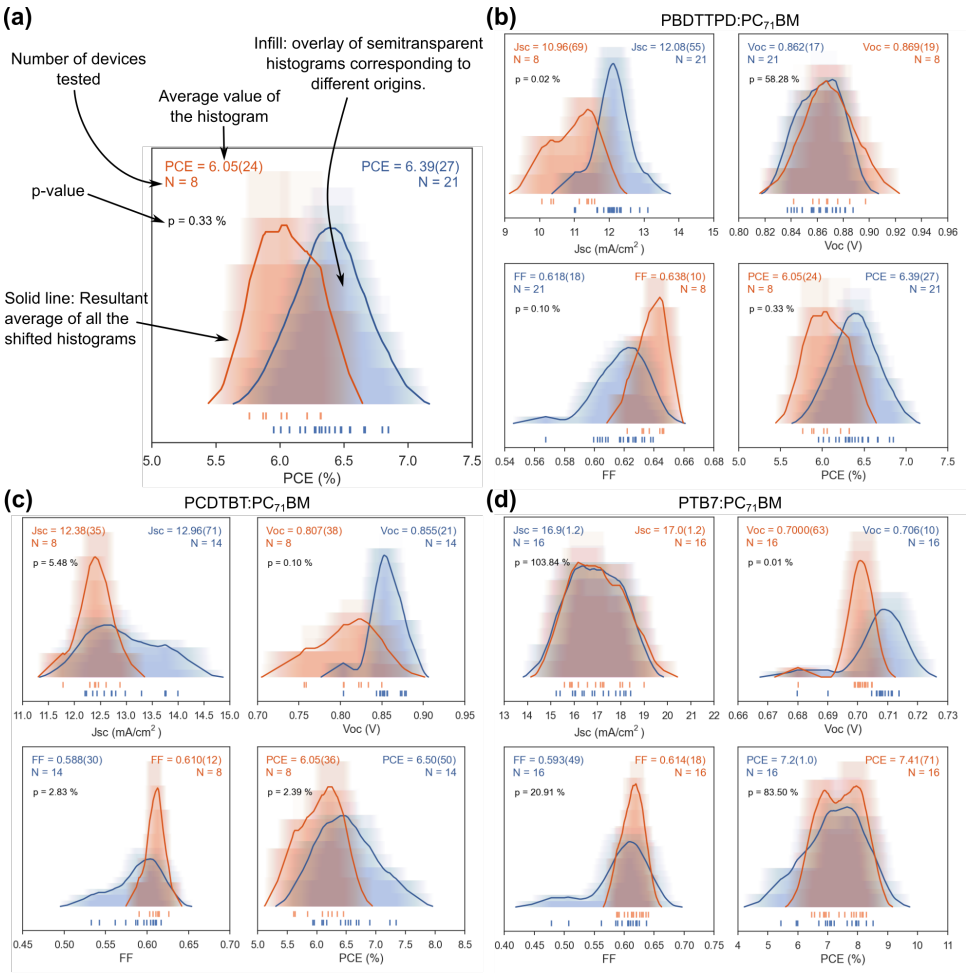

Figure 3.7: Average shifted histograms of J_{SC}, V_{OC}, FF and PCE for polymer:$PC_{71}BM$ solar cells. (a) Example of a pair of ASHs, labeling all the information contained in these figures. (b) PBDTTPD:$PC_{71}BM$, (c) PCDTBT:$PC_{71}BM$ and (d) PTB7:$PC_{71}BM$. Reprinted with permission from reference.[15] Copyright 2015 by American Chemical Society.

remains as to the reason for these differences, as to whether these effects are grounded upon electronic and/or morphological factors. This question is addressed in the following discussion.

3.3 Discussion

When investigating the role of charge extraction barriers between interfaces in OPV devices it is important to consider how the energy levels will align. As is traditionally practiced, the vacuum-level energy diagram of the different OPV stacks is typically portrayed as shown in Figure 3.5. From this energy level diagram, it would appear that hole extraction is energetically favorable from both the PBDTTPD and PCDTPT layers to the PBDTTPD-COOH layer, while a hole extraction barrier would exist between the PTB7 and PBDTTPD-COOH layer. As such, it would be tempting to conclude that the mismatch of energy levels accounts for the differences in enhancement of the PCE observed in this work. However, it is not always the case that vacuum level alignment occurs between adjacent organic layers.[295] Therefore, UPS was utilized in order to determine the relative energy level alignment of the various donor polymer materials used in this study with the anode interface.

Shown in Figure 3.8a are UPS work function scans of ITO, ITO/PEDOT:PSS and ITO/PEDOT:PSS/PBDTTPD-COOH substrates, where we see that the work function increases from 4.7 eV to 5.1 eV upon application of PEDOT:PSS, and

Table 3.2: Summary of OSC device performance for the different polymer:$PC_{71}BM$ BHJs and architectures.

Polymer	Conditions		J_{SC} (mA/cm^2)	V_{OC} (V)	PCE (%)	FF
PBDTTPD	1*	Average	11.2 ± 0.6	0.89 ± 0.02	5.6 ± 0.5	0.55 ± 0.06
		Best	11.91	0.9	6.12	0.56
	2*	Average	11.0 ± 0.7	0.87 ± 0.02	6.1 ± 0.2	0.64 ± 0.01
		Best	11.1	0.86	6.2	0.64
	3*	Average	12.1 ± 0.6	0.86 ± 0.02	6.4 ± 0.3	0.62 ± 0.02
		Best	13.03	0.87	7.01	0.62
PCDTBT	1*	Average	12.5 ± 0.4	0.83 ± 0.01	5.6 ± 0.4	0.54 ± 0.02
		Best	13.14	0.83	6.2	0.55
	2*	Average	12.4 ± 0.4	0.81 ± 0.04	6.1 ± 0.4	0.61 ± 0.01
		Best	12.38	0.82	6.34	0.63
	3*	Average	13.0 ± 0.7	0.86 ± 0.02	6.5 ± 0.5	0.59 ± 0.03
		Best	13.74	0.88	7.34	0.62
PTB7	1*	Average	16.8 ± 0.6	0.70 ± 0.01	7.1 ± 0.3	0.60 ± 0.01
		Best	17.41	0.69	7.53	0.62
	2*	Average	17.0 ± 1.2	0.70 ± 0.00	7.4 ± 0.7	0.61 ± 0.02
		Best	18.36	0.7	8.16	0.63
	3*	Average	16.9 ± 1.2	0.71 ± 0.01	7.2 ± 1.0	0.59 ± 0.05
		Best	18.21	0.71	8.29	0.62

1* - ITO/PEDOT:PSS/BHJ/LiF/Al/Mg, 2* - ITO/PEDOT:PSS/$CHCl_3$:DMSO rinse/BHJ/LiF/Al/Mg and 3* - ITO/PEDOT:PSS/PBDTTPD-COOH/BHJ/LiF/Al/Mg.

is further increased to 5.2 eV after PBDTTPD-COOH deposition. Next, layers of donor polymer were deposited on the ITO/PEDOT:PSS/PBDTTPD-COOH substrates, resulting in vacuum level shifts to 4.6, 4.8 and 4.7 eV for PTB7, PCDTBT and PBDTTPD respectively (Figure 3.8b). This reduction in work function can be understood using the integer charge-transfer (ICT) model, where a spontaneous flow of electrons from the organic donor polymer to the substrate will occur if the work function of the substrate is greater than the energy of the ICT^+ level of the polymer.[139] This transfer of electrons from the donor polymers to the substrate will result in pinning of the polymer to the ICT^+ level to the Fermi level of the substrate. Using the measured HOMO levels of the various organic donor polymers and the vacuum level shifts observed in Figure 3.8b, the energy level alignment at the PBDTTPD-COOH/organic donor polymer interfaces can be determined, as shown in Figure 3.8c. From these energy level diagrams, we see that for all three organic donor polymers used in this work, the HOMO level of the donor polymer is below the Fermi level of the substrate, and as such there is no energy barriers in holes extraction from the donor polymer through the interface to ITO electrode in all three cases. It is also noted that this scenario would also be the case for the ITO/PEDOT:PSS substrate. From these data we can conclude that the differences in the HOMO levels of the donor polymers are not the origin of the observed differences in device performance upon application of the PBDTTPD-COOH interfacial layer.

Next we consider the influence of the PBDTTPD-COOH interfacial layer on the

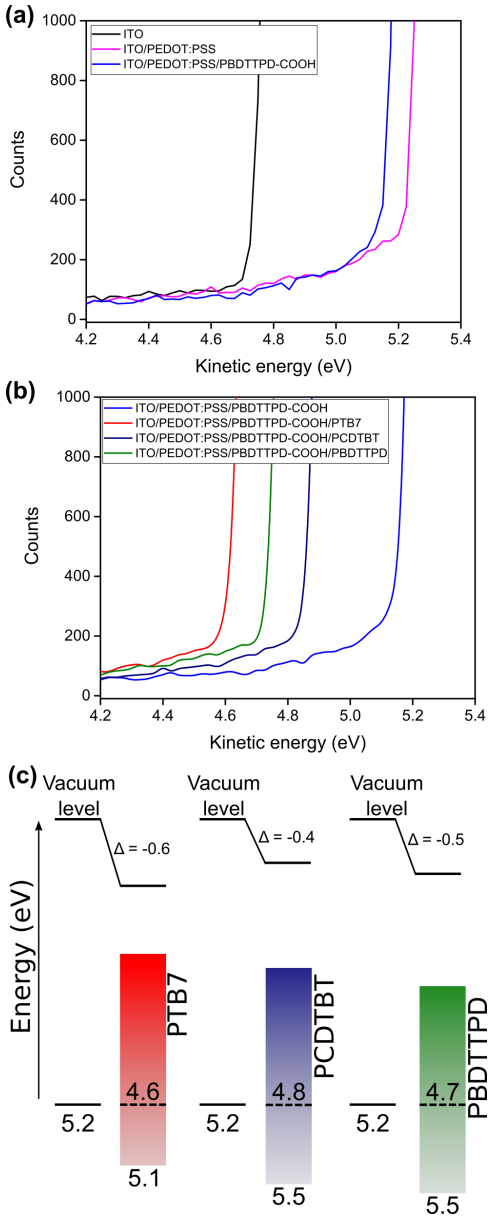

Figure 3.8: (a) UPS spectra of ITO, ITO/PEDOT:PSS and ITO/PEDOT:PSS/PBDTTPD-COOH surfaces. (b) UPS spectra of ITO/PEDOT:PSS/PBDTTPD-COOH with layers of PTB7, PCDTBT and PBDTTPD. (c) Energy diagrams of polymers with the substrate after equilibration. Reprinted with permission from reference.[15] Copyright 2015 by American Chemical Society.

morphology of the BHJ. As seen in Figures 3.9, 3.11 and 3.12, the XRD spectra of the BHJs with the PBDTTPD-COOH interfacial layer are essentially identical to those without an interfacial layer. Moreover, both TEM and AFM micrographs of BHJs with and without the PBDTTPD-COOH interfacial layer do not reveal any significant differences (Figure 3.10). From these data, we can reasonably conclude that the interfacial layer has little obvious influence on the crystallinity or lateral morphology of the BHJs. Although the PBDTTPD-COOH interfacial layer does not significantly affect the crystallinity or lateral morphology of these BHJs, it could influence the vertical composition profile of the BHJs. A large number of studies have elucidated the origins of a vertical composition profile, and its impact of solar cell performance.[296–300] This vertical composition profile is primarily due to the differences in surface tension between the components of the BHJ, and their interaction energies with anode and cathode interfaces. Specifically, in polymer/fullerene BHJs, it is generally found that there is an enrichment of PCBM at the buried ITO/PEDOT:PSS anode interface, which causes hole blocking and charge recombination, resulting in decreased solar cell performance.[301]

To investigate the impact of the PBDTTPD-COOH layer on the BHJ composition at the buried anode interface, the surface energies of each polymer (PBDTTPD, PCDTBT and PTB7) and PBDTTPD-COOH were measured using contact angle goniometry (see experimental methods for details). From the results shown in Table 3.3, it can be seen that the surface energies of the polymers used in this study range between 27.7 and 36.6 mJ/m^2, which are all comparatively lower

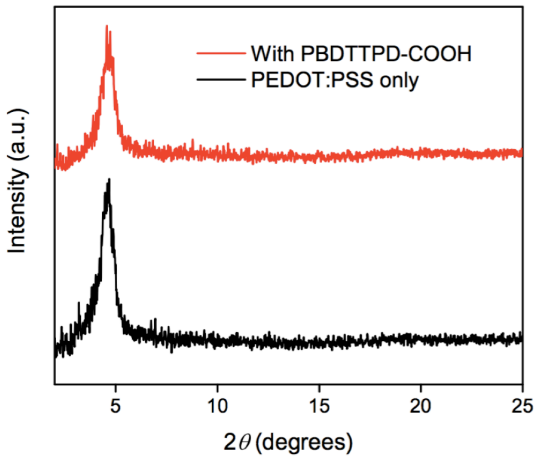

Figure 3.9: XRD of the ITO/PEDOT:PSS/PBDTTPD:$PC_{71}BM$ BHJ with and without PBDTTPD-COOH interfacial layer. Reprinted with permission from reference.[15] Copyright 2015 by American Chemical Society.

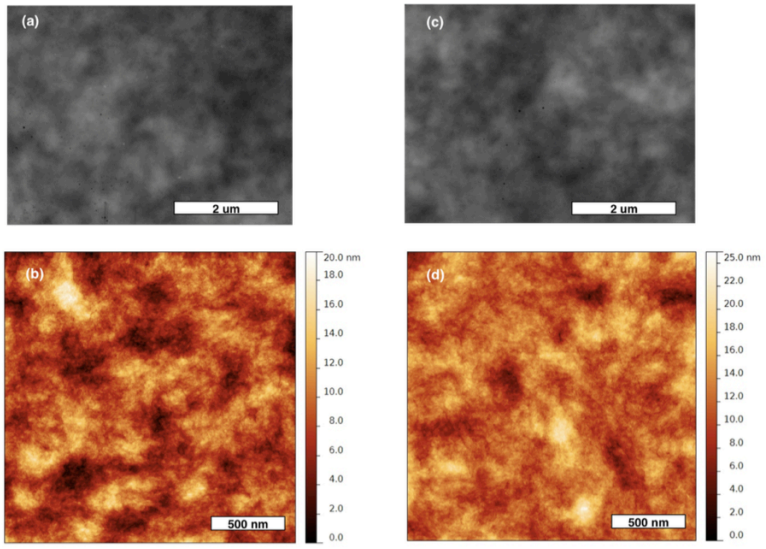

Figure 3.10: TEM and AFM of BHJ morphology. (a-b), BHJ without PBDTTPD-COOH; (c-d), BHJ with PBDTTPD-COOH. All samples are complete devices without metal top contact. TEM samples were prepared by the floating method described in the experimental section. (AFM is taken on ITO/(PEDOT:PSS+interfacial layer)/BHJ stack; TEM is carried out on an isolated BHJ layer that was floated off as described in the experimental section. Reprinted with permission from reference.[15] Copyright 2015 by American Chemical Society.

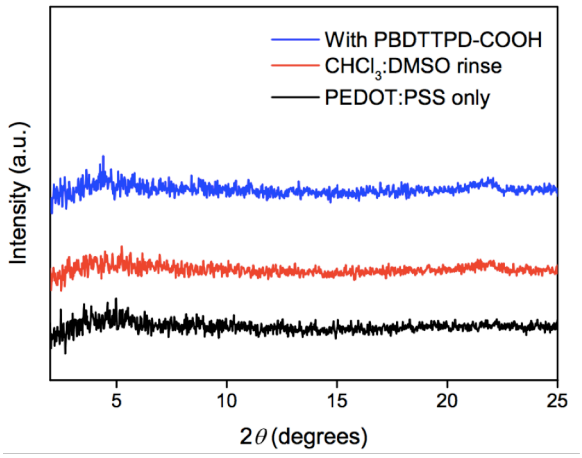

Figure 3.11: XRD of the ITO/PEDOT:PSS/PCDTBT:PC71BM BHJ with and without PBDTTPD- COOH interfacial layer. Reprinted with permission from reference.[15] Copyright 2015 by American Chemical Society.

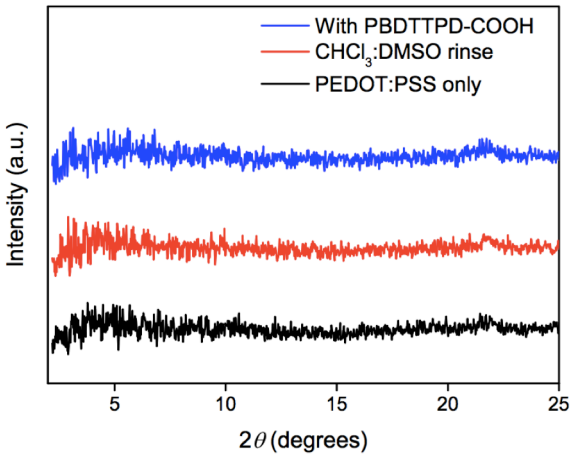

Figure 3.12: XRD of the ITO/PEDOT:PSS/PTB7:PC_{71}BM BHJ with and without PBDTTPD-COOH interfacial layer. Reprinted with permission from reference.[15] Copyright 2015 by American Chemical Society.

Table 3.3: Measured surface energy parameters of different organic materials used in OSC devices investigated in this work.

	γ^{T} (mJ/m^2)	γ^{LW} (mJ/m^2)	γ^{+} (mJ/m^2)	γ^{-} (mJ/m^2)
PEDOT:PSS[a]	63.1 ± 2.8	44.6 ± 2.8	1.86 ± 0.20	46.2 ± 1.5
PCBM[a]	45.8 ± 1.7	45.8 ± 1.7	0	0.88 ± 0.69
PBDTTPD	27.7 ± 0.7	27.7 ± 0.7	0	0.17 ± 0.06
PCDTBT	36.6 ± 0.6	36.6 ± 0.6	0	0.37 ± 0.13
PTB7	30.6 ± 0.6	30.6 ± 0.6	0	0.83 ± 0.10

[a]Values taken from Clark et al. reference[297]

than the 45.8 mJ/m^2 of PCBM. Most importantly, we see that the surface energy of PBDTTPD-COOH (38.0 mJ/m^2) is significantly lower than that of PEDOT:PSS (63.1 mJ/m^2).

Using the measured surface energies of the polymers, it is possible to quantify the influence of the interfacial layer on the composition of the BHJ at the anode. The energy barrier for the deposition of a solvated species on an interface is calculated by,[302]

$$\begin{aligned}\Delta G = &-2(\sqrt{\gamma_1^{LW}}-\sqrt{\gamma_3^{LW}})(\sqrt{\gamma_2^{LW}}-\sqrt{\gamma_3^{LW}}) \\ &+2[(\sqrt{\gamma_1^{+}}-\sqrt{\gamma_2^{+}})(\sqrt{\gamma_1^{-}}-\sqrt{\gamma_2^{-}}) \\ &-(\sqrt{\gamma_1^{+}}-\sqrt{\gamma_3^{+}})(\sqrt{\gamma_1^{-}}-\sqrt{\gamma_3^{-}})-(\sqrt{\gamma_2^{+}}-\sqrt{\gamma_3^{+}})(\sqrt{\gamma_2^{-}}-\sqrt{\gamma_3^{-}})]\end{aligned} \tag{3.3.1}$$

where γ_i^{LW}, γ_i^+ and γ_i^- denote the Lifshitz-van der Waals, Lewis acid and base surface energy components. While γ_1, γ_2 and γ_3 are the surface energies of the solvated species, the interface and the solvent, respectively. To a first order approximation, the rate of deposition of each species at the interface will be proportional to the Arrhenius factor, $\exp(-N_A^{1/3}V^{2/3}\Delta G/RT)$, where N_A is the Avogadro constant and V is the molar volume of the species. As such, the concentration of any species at the interface is given by,

$$c_i^{inter} = \frac{c_i \exp(-N_A^{1/3}V_i^{2/3}\Delta G_i/RT)}{\sum_{n=1}^{N} c_n \exp(-N_A^{1/3}V_n^{2/3}\Delta G_n/RT)}$$

where c_i is the bulk composition of the i^{th} component. In this manner, we have calculated the polymer composition of each BHJ (PBDTTPD, PCDTBT and PTB7) at both the PEDOT:PSS and PBDTTPD-COOH interfaces. From these calculations, we find that the interfacial composition of PBDTTPD/PCBM BHJs on PEDOT:PSS is expected to be polymer deficient (28% polymer), relative to the bulk composition of 40% polymer:60% $PC_{71}BM$. However, on a PBDTTPD-COOH anode, the interface becomes slightly polymer enriched, with a composition of 46% PBDTTPD.(Listed in Table 3.4) A similar trend is observed for the PCDTBT/$PC_{71}BM$ BHJs, where the interfacial composition on PEDOT:PSS is polymer deficient, 13%, while on PBDTTPD-COOH the interfacial composition matches the bulk composition of 20% polymer. Conversely, the interfacial composition of the PTB7/PCBM BHJ on PEDOT:PSS is predicted to be 41%

polymer, which closely matches the bulk composition of 40% polymer. Moreover, on a PBDTTPD-COOH interface layer, there is only a small increase in composition to 47% polymer.

Table 3.4: Calculated polymer compositions for each BHJ (PBDTTPD, PCDTBT and PTB7) at the buried anode interface for both PEDOT:PSS and PBDTTPD-COOH anodes.

BHJ / Interfacial layer	PBDTTPD:$PC_{71}BM$ (1:1.5)	PCDTBT:$PC_{71}BM$ (1:4)	PTB7:$PC_{71}BM$ (1:1.5)
	% PBDTTPD @ anode	% PCDTBT @ anode	% PTB7 @ anode
PEDOT:PSS	28%	13%	41%
PBDTTPD-COOH	46%	20%	47%

These results strongly suggest that the observed changes in solar cell efficiency with a PBDTTPD-COOH interfacial layer are primarily driven by changes in the BHJ composition at the anode. For both the PBDTTPD- and PCDTBT-based BHJs, the buried interfaces are PCBM-rich relative to the bulk concentration of the BHJ when a PEDOT:PSS anode is used. Upon application of the PBDTTPD-COOH layer, the buried interface is no longer PCBM-rich, which we believe is the reason for the improved performance of these cells with the application of the interfacial PBDTTPD-COOH layer. Interestingly, when PEDOT:PSS is used as the anode in the PTB7:PC71BM solar cells, the interfacial composition is essential that of the bulk BHJ. As such, we would not expect a significant improvement in efficiency upon addition of the PBDTTPD-COOH, as there is only a slight decrease in PCBM concentration at the interface. In order to directly investigate the interfacial BHJ composition at the buried PBDTTPD-COOH/PEDOT:PSS/ITO anode, we performed ToF-SIMS depth profiling of all three different polymer BHJs.

Shown in Figure 3.13a are the -CN fragment depth profiles of PBDTTPD/$PC_{71}BM$ BHJs (which are proportional to the concentration PBDTTPD), with and without the PBDTTPD-COOH interfacial layer. Consistent with the surface energy calculations, we see that the concentration of PBDTTPD is higher at the anode when the PBDTTPD-COOH interfacial layer is used. Similarly, in Figure 3.13b the nitrogen depth profiles of PCDTBT/$PC_{71}BM$ BHJs (which is proportional to the concentration of PCDTBT) have a higher concentration of PCDTBT at the anode when a PBDTTPD-COOH interfacial layer is used. Lastly, the fluorine depth profile of PTB7/PCBM BHJs (which is proportional to the concentration of PTB7, except at the cathode where there is a LiF layer) is essentially unchanged when comparing the PEDOT:PSS and PBDTTPD-COOH anodes, which is consistent with the surface energy calculations and solar cell performance.

3.4 Conclusions

OPVs are assembled from a carefully chosen palette of different materials, each of which performs a specific function within the device. There are at least 5 sets of interfaces between the thin layers within the OPV stack, and thus the characteristics of each interface would be expected to affect, both negatively and positively, the most basic mechanistic aspects of the solar cell, from exciton separation and mobility, to charge extraction. The nature of one layer can also influence the physical aspects of the other, including the morphology and composition of a

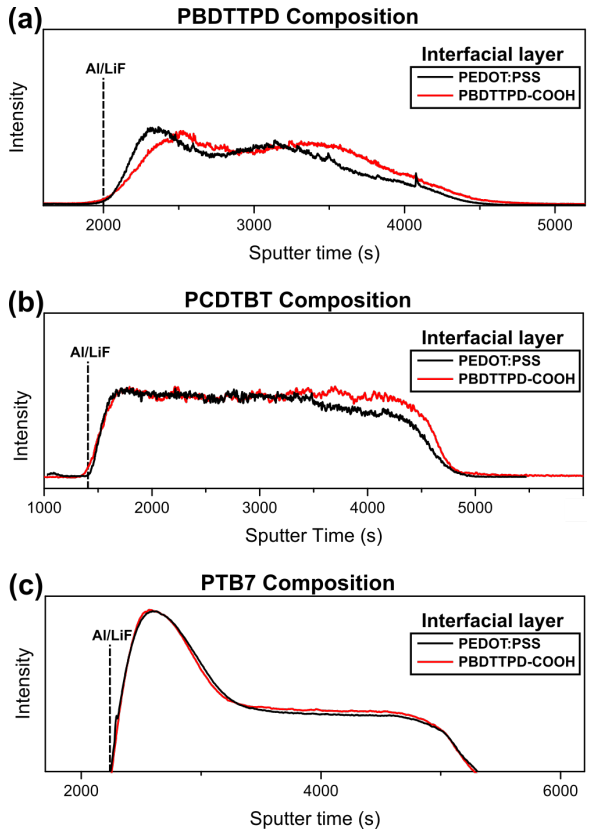

Figure 3.13: ToF-SIMS depth profiles of polymer:$PC_{71}BM$ bulk heterojunctions with a PEDOT:PSS or PBDTTPD-COOH anode interfacial layer. (a) -CN fragment depth profiles of PBDTTPD:$PC_{71}BM$, proportional to PBDTTPD concentration. (b) Nitrogen depth profiles of PCDTBT:$PC_{71}BM$, proportional to PCDTBT concentration. (c) Fluorine depth profiles of PTB7:$PC_{71}BM$, proportional to PTB7 concentration (except at LiF interface). Reprinted with permission from reference.[15] Copyright 2015 by American Chemical Society.

neighboring material with which it is in close physical contact. In the examples shown here, competing effects resulting from modification of the ITO/PEDOT:PSS electrode with a low band gap interfacial layer were deconvoluted, and it was shown that the most important factor in terms of magnitude was the effect of surface energy, which alters the local concentration of donor and acceptor in the adjacent BHJ. However, it was also shown that each polymer/fullerene BHJ combination must be evaluated on an individual basis, as subtle differences in surface energy components can significantly modify the vertical composition profile. The complex melange of possible effects, from electronic to morphological, is challenging to disentangle, but possible, to enable a better understanding of the role of an interface within an OPV device.

3.5 Experimental

3.5.1 Generalities

ITO coated glass (8-12 Ω/sq) substrate was purchased from Delta Technologies Ltd. PEDOT:PSS and Al (99.99%) were purchased from Heraeus (Clevios P VP AI 4083), and Kurt J. Lesker, respectively. PBDTTPD[120] and PCDTBT[222,266] were synthesized according to published literature procedures. PTB7 was purchased from 1-Materials Inc.; $PC_{71}BM$ was purchased from American Dye Sources Inc. Toluene and THF were used as obtained from a PureSolve purification system. Methanol was purchased from Fisher Scientific, and $CHCl_3$ was purchased from BDH Chemicals.

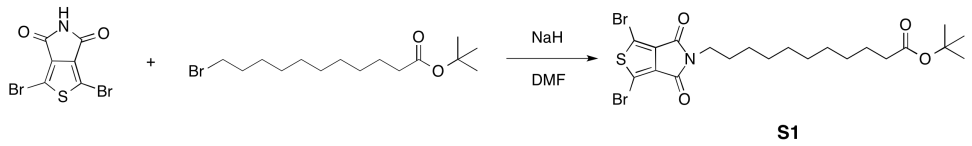

Figure 3.14: Synthesis of **S1**. Reprinted with permission from reference.[15] Copyright 2015 by American Chemical Society.

All other reagents and chemicals were used as received from Sigma-Aldrich unless otherwise stated. All reactions were carried out under an inert atmosphere using standard Schlenk techniques, or in a glove box, unless otherwise noted.

3.5.2 PBDTTPD-COOtBu Synthesis

Synthetic procedures for **S1** are described in figure 3.14.

1,3-Dibromo-4H-thieno[3,4-c]pyrrole-4,6(5H)-dione (0.6 g, 1.93 mmol, 1.0 eq) was dissolved in dry DMF (6 mL) and combined with sodium hydride (56 mg, 2.33 mmol, 1.2 eq). The reaction contents were stirred at room temperature for 1 h and then 0.93 g tbutyl 11-bromoundecanoate (0.93 g, 2.90 mmol, 1.5 eq) in 1 mL DMF was added. After stirring for 6 h at RT, the reaction mixture was extracted with diethyl ether (50 mL) and washed with water (3 $\times$ 50 mL). The organic layer was dried, filtered, concentrated. Pure compound was obtained by washing with ethanol, leaving a white solid. Yield: 40 ^{1}H NMR (400 MHz, $CDCl_3$): δ (ppm) = 3.60 (t, J = 7.6 Hz, 2 H), 2.20 (t, J = 7.6 Hz, 2 H), 1.60 (m, 4 H), 1.44 (s, 9 H), 1.22 (m, 12 H). ^{13}C NMR (100 MHz, $CDCl_3$): δ (ppm) = 173.34, 160.40, 134.85, 112.94, 79.89, 38.84, 35.65, 29.39, 29.27, 29.13, 29.09, 28.27, 28.15, 26.80, 25.13. HRMS

(ESI, m/z): calculated for $C_{21}H_{29}Br_2NNaO_4S$ [M+Na]: 574.0061, found 574.0049.

S2 was synthesized according to previously reported procedures.[237,303] **S1** (311 mg, 560 μmol) was combined with **S2** (435 mg, 560 μmol), tris(dibenzylideneacetone)di-palladium (16 mg, 3%) and tri-*o*-tolylphosphine (21 mg, 12%) in a 3-neck 50 mL Schlenk flask under N_2 (see Figure 3.2 for structures of **S1** and **S2**). 12 mL of degassed toluene was then added to the flask and the reaction mixture was refluxed for 24 h. After cooling the reaction mixture to room temperature, the crude product mixture was diluted with $CHCl_3$ (100 mL), added to an aqueous solution of sodium diethyldithiocarbamate (1g/100 mL) and stirred for 12 h at room temperature. Afterwards, the organic layer was separated and volatiles were reduced to ~10 mL. The mixture was slowly precipitated in methanol (80 mL). The precipitate was filtered through a Soxhlet thimble and purified *via* Soxhlet extraction for 12 h with methanol, followed by 12 h with hexane, before the polymer was finally collected from chloroform. The chloroform solution was concentrated by evaporation, precipitated using methanol (80 mL) and filtered to yield the desired polymer product. Yield: 90%. ^{1}H NMR (400 MHz, $CDCl_3$): δ (ppm) = 9.00-8.00 (br, 2H), 4.80-3.40 (br, 6H), 2.40-0.60 (m, 57H). Mn = 14 kDa; Mw = 31 kDa; PDI = 2.2.

3.5.3 Deprotection of PBDTTPD-COOtBu to yield PBDTTPD-COOH

Trifluoroacetic acid (TFA, 2 mL) was added to PBDTTPD-COOtBu (200 mg, 238 μmol, see Figure 3.2) in CH_2Cl_2 solution (2 mL), and then the mixture was stirred for 2 h at room temperature under an N_2 atmosphere. 50 mL MeOH was added to the mixture, and the desired polymer was then precipitated in quantitative yield. The polymer was purified by washing with MeOH 4 times and drying under vacuum. ^{1}H NMR (400 MHz, $CDCl_3$): δ (ppm) = 9.00-7.40 (br, 2H), 4.60-3.20 (br, 6H), 2.80-0.60 (m, 48H).

3.5.4 Solar Cell Fabrication

Organic solar cells were fabricated using an architecture of ITO/PEDOT:PSS/(interfacial layer)/BHJ/LiF/Al/Mg. First, ITO glass substrates were cleaned through sequential 10 min ultrasonication in methylene chloride, Milli-Q water (18.2 MΩ•cm) and isopropyl alcohol, followed by drying under nitrogen flow. After this, the substrates were further cleaned by 5 min air plasma in a Harrick plasma cleaner (0.1 mTorr, PDC 32G, 18W). PEDOT:PSS was filtered through a 0.2 μm cellulose acetate filter before spin-casting onto the clean ITO substrates at 3000 rpm for 60 s. The PEDOT:PSS films were then annealed at 120 °C for 10 min in air. If it was used, a 0.05 mg/mL solution of PBDTTPD-COOH in $CHCl_3$:DMSO (10:1) was spin-cast onto the ITO/PEDOT:PSS film at 1000 rpm

for 60 s, followed by annealing at 120 °C for 5 min under ambient atmosphere. The BHJ solution was spin-cast from a polymer:$PC_{71}BM$ solution in ambient; the ratio and conditions were: 1) PBDTTPD:$PC_{71}BM$, 1:1.5 (w/w), 2% chloronaphthalene (CN), dissolved in chlorobenzene (CB), 20 mg/mL, spin-cast at 1200 rpm, 45 s; 2) PTB7:$PC_{71}BM$, 1:1.5 (w/w), 3% 1,8-diiodooctane (DIO), dissolved in CB, 20 mg/mL, spin-casted at 2000 rpm, 2 min. 3) PCDTBT:$PC_{71}BM$, 1:4 (w/w), dissolved in *o*-DCB, 15 mg/mL, spin-cast at 1000 rpm, 60 s. The spin-cast films were then sealed in petri-dishes wrapped by parafilm for 20-30 min until completely dry. The cells were then transported to a glovebox evaporator for metal electrode deposition. The top aluminum (20 nm) and Mg (60 nm) cathodes were deposited by thermal evaporation (deposition at a rate of $\sim$2 Å s^{-1} and 2.5 Å s^{-1} under high vacuum, 5×10^{-6} Pa, respectively). The Mg top contact was used to ensure low deposition temperatures.[304] The solar cells were then tested at 25-30 °C under nitrogen flow using simulated AM 1.5G conditions (xenon source from Oriel 91191 1000 W, 100 mW/cm^2), equipped with a custom made water filter and calibrated to a certified Si reference cell with a KG-5 filter(PV Measurements, PVM624). The light intensity was measured using a thermopile (XLP12-3S-H2) during the test. The photovoltaic parameters were recorded using a computer-controlled Keithley 2400 source meter.

3.5.5 Characterization Methods

^{1}H, ^{13}C, and ^{19}F NMR spectra were recorded on a Varian Inova-400 or VNMRS-500 spectrometer. Mass spectra were obtained on an Agilent 6220 spectrometer

or Bruker Ultraflextreme MALDI TOF/TOF system (Bruker Daltonics, Bremen, GmbH). GIXRD was performed using a Bruker D8 Discover instrument with a Cu Kα beam (40 kV, 40 mA; λ = 1.541784 Å, angle of incidence = 0.3°). UV-vis measurements were performed using a PerkinElmer Lambda 1050 spectrophotometer. AFM was performed in tapping mode using a Digital Instruments/Veeco multimode tapping atomic force microscope, and the collected data were analyzed using the open source software Gwyddion.[305] SEM and TEM images were obtained using a Hitachi S-4800 Field Emission SEM (FE-SEM). TEM samples were prepared by immersing the device (without metal electrode) in water, floating the BHJ, and then carefully using a TEM grid to support the film and let it dry. UPS and TOF-SIMS data were measured by the University of Alberta nanoFAB. UPS is carried out done with a Kratos Axis Ultra system, equipped with a 21.2 eV (He I) source, operating at a power of 60 W (3 kV × 20 mA). A 10 volts bias was applied to the sample to measure the cut-off edge for the measurement of work function. The energy step used was 0.025 eV. Work function is extracted from the lowest kinetic energy cutoff. Depth profiles were obtained using a TOF-SIMS IV instrument (ION-TOF GmbH), having a base pressure better than 5×10^{-9} mbar. During depth profiling, Bi^+ ions were used as the analytical source, operated at 25 kV; Cs^+ ions were used as the sputtering source, operated at 500 V, with an ion current of ∼20 nA. By alternating these two ion beams on samples, depth profiles were generated. The craters sputtered were about 300 × 300 μm^2, while acquisition areas of profiles were 40 × 40 μm^2 in the centers of craters.

Table 3.5: Average contact angle of each polymer surface with the four different probe liquids used to determine the surface energies. Each value is the average of 8 separate measurements and the error listed is the standard deviation.

	Water (°)	Diiodomethane (°)	Ethylene Glycol (°)	Formamide (°)
PBDTTPD	103.0 ± 0.5	52.4 ± 0.5	80.3 ± 1.6	89.3 ± 2.2
PCDTBT	97.1 ± 0.8	40.7 ± 0.6	65.5 ± 1.0	75.6 ± 1.6
PTB7	97.3 ± 0.4	47.8 ± 0.4	72.9 ± 1.1	84.8 ± 1.8
PBDTTPD-COOH	82.1 ± 3.4	42.5 ± 1.0	53.5 ± 0.9	64.4 ± 0.9

3.5.6 Surface Energy Measurements

Contact angle measurements were carried out using a First Ten Angstroms FTA200 goniometer. For each different surface, contact angles were collected using four different probe liquids: diiodomethane, water, ethylene glycol and formamide. For each probe liquid, contact angles of a minimum of 8 droplets were recorded. Each drop was allowed to equilibrate until a stable contact angle was reached (∼15 s). From these measured contacts angles the mean and standard deviation were calculated for each probe liquid and each surface (Table 3.5). Using these values, a Monte Carlo method of non-negative least-squares was used to determine the surface energy parameters.[297] The surface energy parameters used for the probe liquids are given in Table 3.6.

Table 3.6: Surface energy components of probe liquids and solvents.

	γ^T (mJ/m^2)	γ^{LW} (mJ/m^2)	γ^+ (mJ/m^2)	γ^- (mJ/m^2)
Water[a]	72.8	21.8	25.5	25.5
Diiodomethane[a]	50.8	50.8	0	0
Ethylene Glycol[a]	48.0	29.0	3.0	30.1
Formamide[a]	58.0	39.0	2.28	39.6
Chlorobenzene[b]	33.6	32.1	0.78	0.72
o-Dichlorobenzene[b]	35.7	34.2	1.0	0.58
Chloronapthelene	41.8[c]	41.8[c]	0 [e]	1.0[e]
Diiodooctane	43.6[d]	43.6[d]	0 [f]	0[f]

[a]Values taken from reference;[302] [b] Values taken from reference;[297] [c] Values taken from reference;[306] [d] Values taken from reference;[307] [e] Values based on similarity to napthelene, taken from reference.[302] [f] Values based on similarity to diiodomethane.

4

Nanostructured Electrodes in Organic Solar Cells

4.1 Introduction

Organic solar cells have attracted intense attention in both research and industry over the last two decades.[36,72,255] They are competitive renewable energy sources with the advantages of low cost, light-weight, and the potential for roll-to-roll production.[62,69,308] A typical BHJ solar cell consists of a transparent indium-tin-oxide (ITO) electrode, a metal contact electrode, and a donor/acceptor matrix sandwiched in between.[95,111] The donor/acceptor matrix is called a BHJ, which works as the photoactive layer to absorb photons.[75,79] In polymer BHJ solar cells, the donors are typically semiconducting conjugated polymers, while the typical acceptors are fullerene derivatives, such as $PC_{61}BM$ and $PC_{71}BM$. When light

illuminates a photovoltaic device, photons with energy larger than the polymer's bandgap can be absorbed by the conjugated polymer. The energy of the photon could excite an electron from the valence band to the conduction band, leaving a hole in the valence band. This electron/hole pair is called an exciton. The generated neutral excitons can diffuse, and separate at the donor/acceptor interfaces into free holes and electrons. From the interfaces, electrons transport through acceptor phase and reach the cathode while holes transport through donor phase and reach the anode.[75,79] Since charge transport strongly depends on the percolating pathway that formed by the donor and acceptor phase and the charge carrier mobilities, the BHJ three-dimensional morphology and arrangement are hypothesized to contribute the power conversion efficiency.[259,309,310] The complex pathways for charge carrier transport and the relatively low charge carrier mobilities are two critical issues that need to be addressed to achieve enhanced performance of BHJ solar cells.

Compared to their inorganic counterparts, donor polymers and acceptor molecules in polymer solar cells generally have very low hole/electron mobilities, which are in the range of $\sim 10^{-4}$-10^{-3} $cm^2/(V \cdot s)$. It has been reported that P3HT has a hole mobility of 10^{-3} cm^2 $/(V \cdot s)$, and $PC_{61}BM$ has an electron mobility of 10^{-4} cm^2 $/(V \cdot s)$.[88] The low mobilities limit the charge carrier extraction in a BHJ, since these charges must be transported towards the desired electrode before they recombine. Specifically, the carrier diffusion length is limited by the charge mobility, and the diffusion length is defined by:

$$L_{diffusion} = \sqrt{D\tau} = \sqrt{\mu\tau kT/e}$$

where μ is the charge carrier mobility; τ is the charge carrier lifetime; D is the diffusion coefficient; k is the Boltzmann constant; e is the electron charge.[91] L_d must be longer than the active layer thickness to prevent significant loss by recombination. Hence, a high mobility or thin film is necessary for efficient charge-carrier extraction.[311,312].

Fortunately several donor polymers containing a diketopyrrolopyrrole (DPP) unit have been developed and shown to have a relatively high hole mobility.[117,313] The DPP unit is an attractive electron-deficient building block that has been used in a variety of applications.[314,315] Association of the DPP unit with appropriate electron donating building blocks has been reported to make low band gap polymers with high charge carrier mobility. The coplanar backbone of DPP is crucial for high charge delocalization over the polymer backbone and strong cofacial π-π interactions between polymer chains, which contributes to the high charge carrier mobility.[117,316–318] For example, PDPP-TT-T-TT has a hole mobility of 1.42 $cm^2/(V \cdot s)$ according to Bronstein and coworkers.[118] However, the problem remains that high electron mobility acceptors have not yet been developed. As a result, using these high hole mobility polymers in combination with the low electron mobility PCBM could result in a mismatched system where the mobility of holes is significantly higher than that of electrons. If one charge carrier mobility

is insufficient, the carriers are unlikely to reach the contacts, but instead, they recombine at trap sites or remain in the device as undesirable space charges that oppose the flow of new carriers which will hamper device performance.

An attractive approach for solving the mismatch mobility problem is to use high-surface-area electrodes. In this work, we present the use of high-surface-area nanostructured ITO electrodes to compensate for the low electron mobility in a BHJ using a high hole mobility polymer. The rationale of using a large surface area electrode is to improve charge collection by geometrically reducing the distances between photogenerated charges and the electrode without reducing the effective thickness of the device. In our previous work we used amorphous ITO nanopillars to improve P3HT:$PC_{61}BM$ solar cell efficiency.[209] Other types of nanostructured electrodes, including ZnO[204,319], TiO_2,[213,320,321] and organic self-assembled fibers[214] have been utilized in organic photovoltaics and dye-densitized solar cells. However, in these works, the mobility of charge carriers is often neglected, and the balance of charge carrier mobilities has not been discussed. Moreover, few studies have focused on the mechanism of how the nanostructured electrode enhances the solar cell performance.

In this work, we chose an electron/hole mobility mismatched system (high-hole-mobility polymer and low-electron-mobility $PC_{71}BM$) and utilized a nanostructured ITO electrode in an attempt to compensate for the low electron mobility of the $PC_{71}BM$. We utilized glancing angle deposition (GLAD) to grow single-crystalline ITO nanotree (NT) electrodes on commercial ITO coated glass substrates. Upon

applying charge selective interfacial layers, we fabricated inverted solar cells in order to collect electrons at the ITO cathode, while the high-mobility holes were collected at the Ag anode. In this manner, the high-surface-area ITO nanotree electrode penetrates into the BHJ three-dimensionally and offers a short pathway for electron collection, compensating for the low electron mobility. Meanwhile, the effect of embedding nanostructured ITO electrode in BHJ is complicated: internal electric fields, charge carrier pathways, and light management are all subject to change. The consequences of embedding a nanostructured ITO electrode and the mechanisms of how it affects solar cell performance are investigated and discussed in this chapter.

4.2 Results and Discussion

4.2.1 ITO Nanotree Electrode Characterization

In the previous work, amorphous ITO nanopillars grown by GLAD method were used as electrodes in P3HT:$PC_{61}BM$ solar cells, which were found to increase the PCE.[209] While improved performance was obtained, the ITO nanopillars were amorphous at the time. Recently, we have developed a new process to grow single-crystalline ITO nanostructures, which not only have a crystalline nanopillar 'trunks' but also single crystalline branchs that grow epitaxially from the nanopillar 'trunks'.[16] Figure 4.1 shows the scanning helium ion microscopy image of the ITO nanotree grew under certain condition. High resolution SEM image in Figure 4.2

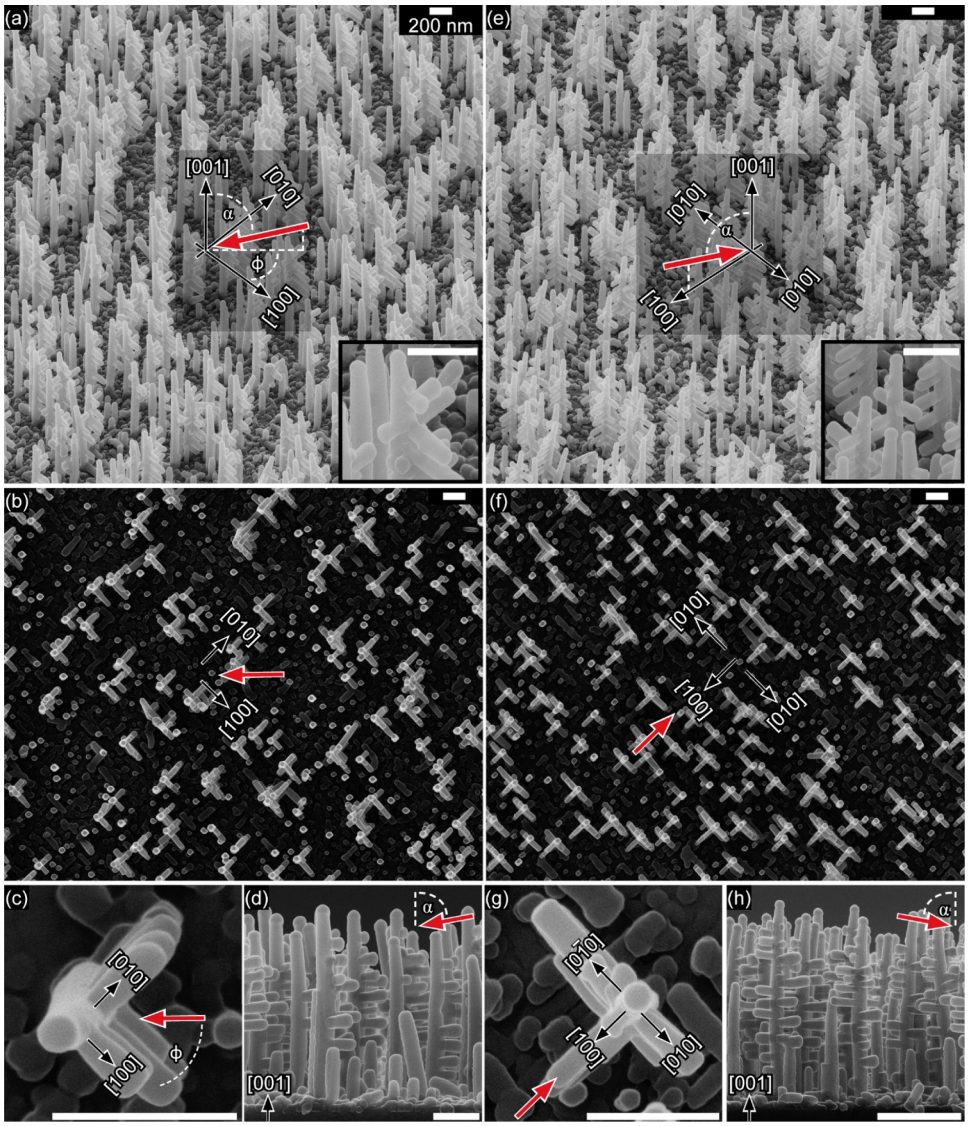

Figure 4.1: Scanning helium ion miscroscopy images of the nanotree shapes controlled by the deposition condition. α is the vapor flux oblique angle relative to the zirconia substrate normal and φ is the offset from the [100] direction of the single cubic crystal ziconia substrate. Images of ITO nanotrees grown with α = 85° and (a−d) φ = 45° (resulting in L-shaped nanotrees) and (e−h) φ = 0° (resulting in T-shaped nanotrees). Red arrows depict vapor flux orientation, and black arrows indicate crystal directions of YSZ substrate. (scale bars: 200 nm). Reprinted with permission from reference.[16] Copyright 2014 by American Chemical Society.

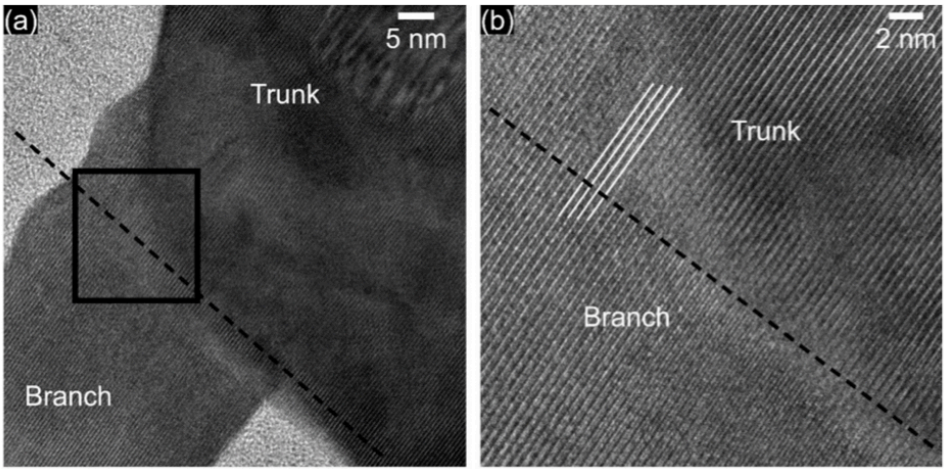

Figure 4.2: HRTEM image of branch-trunk interface on an ITO nanotree. Region in (b) is imaged from black square in (a). Dashed black line indicates branch-trunk interface, while lines in (b) show continuous lattice planes from trunk into branch. Reprinted with permission from reference.[16] Copyright 2014 by American Chemical Society.

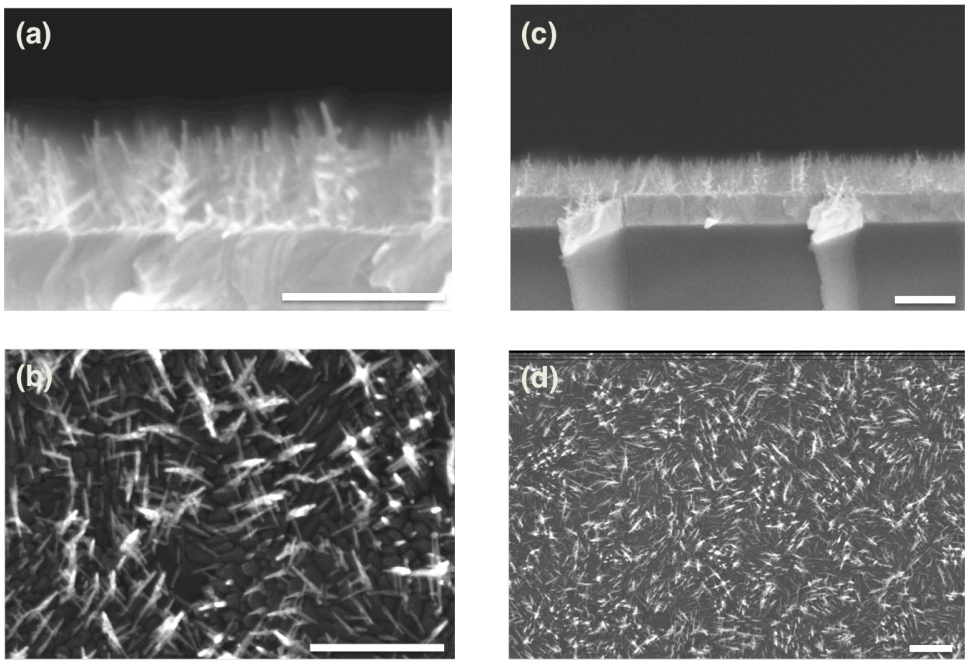

Figure 4.3: SEM images of as-deposited ITO nanotrees.(a-b) Cross-section SEM of the ITO nanotree electrode; (b-d) Top-down SEM of the ITO nanotree electrode. (scale bar, 200 nm)

shows that the nanotree is single crystalline through the trunk and branch. In this work, we adopted this method and grew smaller ITO nanotrees with heights of 50, 75, 100, 120, and 150 nm. Instead of using Si substrates for ease of imaging, these GLAD single-crystalline ITO nanotrees were grown on commercial ITO coated glasses so that they could be used as transparent electrodes in polymer solar cells. The morphology of ITO nanotree electrodes was characterized with a Hitachi S-4800 scanning electron microscope (SEM). Figure 4.3 shows the SEM images of as-deposited 150 nm tall ITO nanotree electrodes. Figure 4.3a,c shows the cross-sectional SEM images, and Figure 4.3b,d shows the top-down SEM images. The as-deposited nanotrees are about 50 nm from each other, forming a nanotree 'forest' on the flat ITO coated glass substrate. The height of the nanotree was monitored by controlling deposition time and confirmed by cross-section SEM images.

To fulfill the requirement of electron extraction at the ITO electrode, an electron-selecting interfacial layer was used. ZnO is a n-type semiconductor metal oxide for electron selection since its deep valence band ($\sim$7.7 eV) could block hole transport while its valence band (4.4 eV) is close to the LUMO of $PC_{71}BM$ and could fulfill electron extraction.[142] However, the common methods for ZnO thin layer deposition on planar substrates such as spin casting, either from a precursor solution or nanoparticle solution, cannot be used with our nanostructured substrate because a uniform conformal layer is required. With this consideration, atomic layer deposition (ALD) was selected to deposit interfacial ZnO to form a conformal coating layer on the surface of ITO nanotrees. The ALD conditions have been

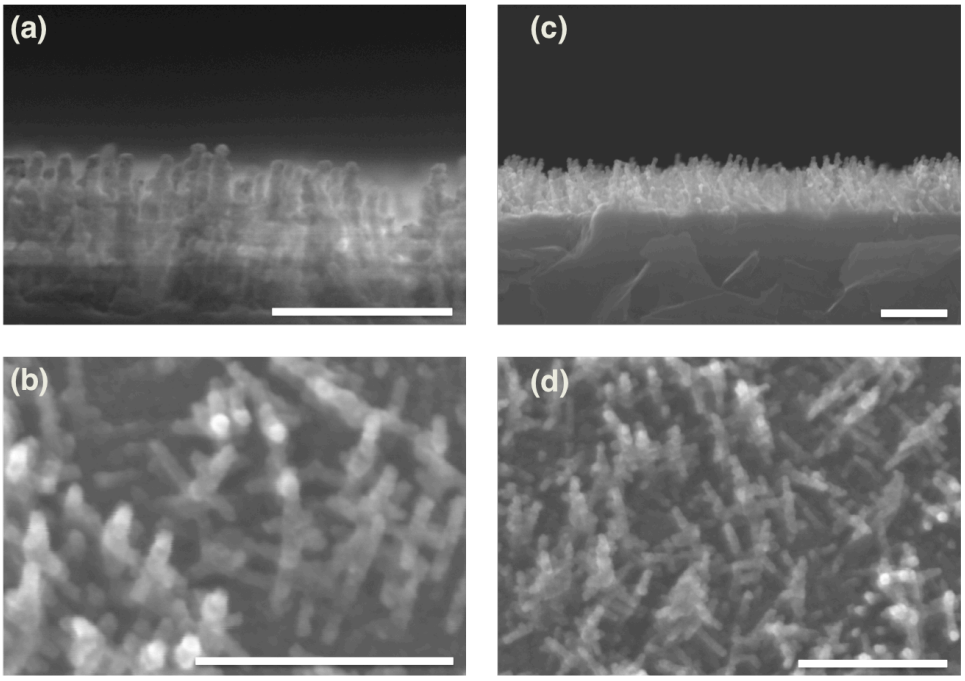

Figure 4.4: SEM images of ZnO coated ITO nanotree using ALD method.(a-b) Cross-section SEM of the ITO nanotree electrode; (b-d) Top-down SEM of the ITO nanotree electrode. (scale bar, 200 nm)

systematically screened at a range of temperatures, and it was found that 8 nm thermal atomic layer deposition (TALD) ZnO at 50 °C resulted in the highest solar cell performance. Figure 4.4 shows the cross-sectional and plan-view SEM micrographs of the 150 nm tall nanotrees with a 8 nm ALD ZnO coating. Both the 'trunk' and 'branch'' of the nanotrees become equally thicker as a result of the ZnO coating. To further confirm that the ZnO coating is uniform and conformal, TEM and energy-dispersive x-ray spectroscopy (EDX) elemental analysis were performed. In Figure 4.5, the EDX elemental analysis was carried out to investigate the ZnO coating. In the top row (a), the EDX line scan clearly shows that the Zn is on the exterior of the nanotree, while the core is rich in indium. In the bottom row (b), a top-down view TEM image was taken by cutting the ITO nanotree to half. Line scan elemental analysis indicates that strong indium signal from the inner the 'trunk', while the zinc signal is mainly from the outer skin, indicating that ZnO 'skin' surrounds the inner ITO 'core'. These results strongly confirm that ITO nanotrees are conformally coated using an 8 nm thick TALD ZnO film.

4.2.2 Solar Cell Devices Fabrication

Bulk heterojunctions of PDPP-TT-T-TT and $PC_{71}BM$ were chosen for the fabrication of solar cells due to their significant differences in mobility. PDPP-TT-T-TT has a hole mobility of 1.42 $cm^2/(V \cdot s)$, and $PC_{71}BM$ has an electron mobility of 10^{-4} $cm^2/(V \cdot s)$. To fabricate OPV devices, the ITO nanotree electrodes need to be infiltrated with a photoactive layer, the compatibility and degree of

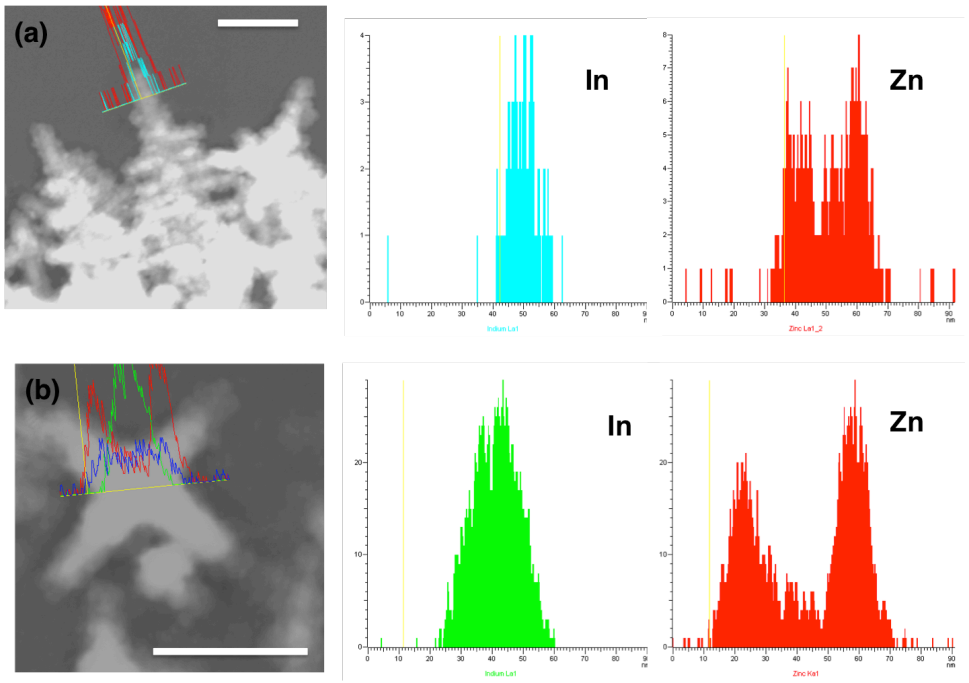

Figure 4.5: Line-scan EDX of a ZnO (10 nm) coated ITO nanotree electrode. (a) front view and (b) top-down view after cutting the 'nanotree' by FIB and elemental anylysis. (scale bar: 80 nm)

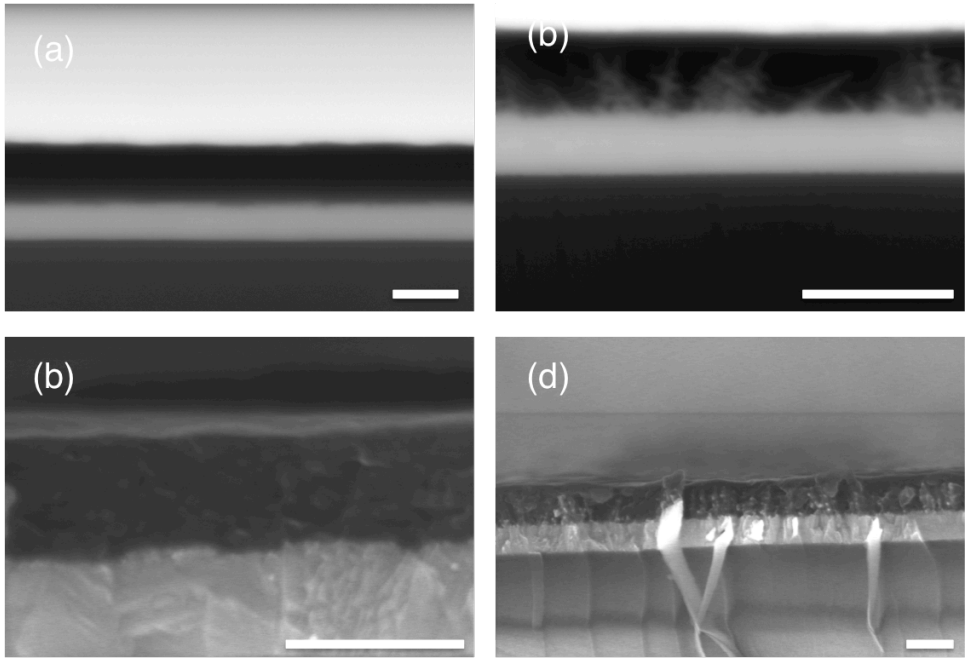

Figure 4.6: Cross-section SEM images of BHJ with flat ITO (a-b) and nanotree ITO (c-d). a,c, back-scattering mode SEM; b,d, regular mode. Scale bar: 200 nm.

infiltration of the BHJ into the three-dimensional structured electrode is the key to fabricating a functional solar cell. Initially, the mixed polymer:PCBM solution was spin-cast onto the freshly deposited ITO electrode and cross-sectional SEM images were taken to observe the infiltration. Cross sections of BHJ solar cells with ITO nanotree electrodes were characterized in SEM using both secondary electrons and backscattered electrons, as shown in Figure 4.6. Figure 4.6 a and c are back-scattering SEM images and b,d are secondary electron SEM images. In a backscattering SEM image, the signal is sensitive to the atomic mass of the nuclei they scatter from. As a result, elements with a higher Z-number appear brighter than those with a lower Z-number. So in Figure 4.6b, the bright phase represents ITO and the dark phase represents the polymer/PCBM mixture. Compared to Figure 4.6a, which was taken on a BHJ with planar electrodes, it is clear that The ITO nanotrees survived during the PDPPTT-T-TT:$PC_{71}BM$ spin-casting process and the PDPPTT-T-TT:$PC_{71}BM$ mixture filled the three-dimensional structure well. Secondary electron cross-sectional SEM images of the BHJ are shown in Figure 4.6d. From the spot where the nanotree partly is exposed (caused by sample preparation process) we see that the polymer:$PC_{71}BM$ mixture filled the nanotree well. To check if the ITO nanotrees were damaged by spin-coating of the active layer, it was washed off the substrate, which was subsequently imaged in SEM. The polymer:PCBM BHJ was washed off by first immersing in $CHCl_3$:ODCB (4:1) to dissolve it, which was then followed by immersing in $CHCl_3$:acetone (1:1) and then pure acetone. The reason to use acetone was to take advantage of its

high evaporation rate in order to avoid capillary forces which could collapse the nanotrees. The resulting ITO nanotrees were imaged in SEM and compared with the as-deposited ITO nanotree electrodes. The results indicate that the nanotrees are undamaged during solar cell processing, and the nanotrees were neither torn down nor broken.

For inverted devices, it is ideal if the BHJ is PCBM rich at the ITO cathode. To promote the accumulation of PCBM on the ITO surface, we modified the surface energy of the cathode to induce the desired phase distribution. The surface of ZnO was modified with a fullerene derivative C60-SAM, a self-assembled monolayer that has been shown to promote vertical phase segregation of the BHJ (where the PCBM is enriched near the SAM) and also results in improved photoinduced charge transfer.[167] The self-assembled monolayer is formed by anchoring of the carboxylic acid group of C60-SAM to the hydrophilic ZnO, leaving the 'body' of the fullerene ball exposed. Consequently, this monolayer modifies both the the workfunction and the surface energy of the interface. The change in surface energy is evidenced by the water contact angle, which goes from 16° (bare ZnO) to 59° after applying the C60-SAM monolayer. After application of the C60-SAM monolayer, the nanotree electrode is infiltrated with the BHJ. The infiltration step consists of spin-casting in air a 1:2 (wt.%/wt.%) blend of PDPP-TT-T-TT and $PC_{71}BM$ in $CHCl_3$:ODCB (4:1) solution (20 mg/ml) onto the nanostructured ITO electrode and slowly evaporating the residual casting solvent over 15–20 min by sealing in a petri-dish. The samples were then transferred to glovebox for MoOx (8 nm) and Ag (20nm) deposition.

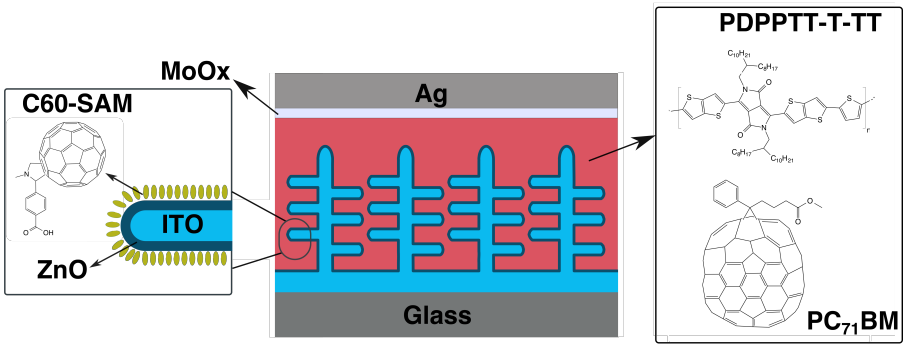

Figure 4.7: Scheme of solar cell device structure.

Table 4.1: Summary of photovoltaic parameters of BHJ solar cellls.

ITO nanotree height (nm)	J_{SC} (mA/cm^2)	V_{OC} (V)	Average PCE (%)	FF
120	13.85 ± 0.61	0.47 ± 0.02	2.80 ± 0.40	0.42 ± 0.04
100	14.04 ± 1.23	0.47 ± 0.33	3.19 ± 0.25	0.43 ± 0.04
75	17.63 ± 0.60	0.53 ± 0.01	4.59 ± 0.41	0.48 ± 0.03
50	16.64 ± 0.33	0.53 ± 0.00	4.42 ± 0.18	0.51 ± 0.01
0	16.54 ± 0.52	0.52 ± 0.01	3.67 ± 0.56	0.47 ± 0.01

4.2.3 Solar Cell Performance

The utility of the ZnO/C60-SAM modified nanotree GLAD ITO electrodes for polymer solar cells was evaluated using the standard PDPP-TT-T-TT:$PC_{71}BM$ BHJ photoactive layer described above. The solar cell device structure is depicted in Figure 4.7. The general device architecture is defined as: commercial ITO/GLAD ITO (nanotree height = x nm)/ZnO/C60-SAM/PDPP-TT-T-TT:$PC_{71}BM$ (∼130 nm thickness)/MoOx(8 nm)/Ag (20 nm)/Mg(60 nm), where x stands for 50, 75, 100 or 120 nm. Magnesium is used to cool the evaporation temperature, so the overall

deposition temperature is less than 100 °C.[11]

The performance of these solar cells are summarized in Table 4.1, and the J-V curves of the champion devices (for each different nanotree height) are shown in Figure 4.8. From these data we see that the solar cell performance changes as the height of ITO nanotree increases. Specifically, the optimum performance is reached at the height of 75 nm, beyond which increasing height reduces solar cell performance. The control devices fabricated on commercially available ITO coated glass had an average efficiency of 3.67 $\pm$ 0.56%, J_{SC} of 16.54 $\pm$ 0.52 mA/cm^2, V_{OC} of 0.52 $\pm$ 0.01 V, and FF of 0.47 $\pm$ 0.01. By using the 50 nm tall ITO nanotree electrode, an increase in FF to 0.51 $\pm$ 0.01 is obtained, which contributes to a higher PCE of 4.24 $\pm$ 0.18 %. A further increase of the ITO nanotree height to 75 nm enhances the PCE to 4.59 $\pm$ 0.41%, primarily due to an increased J_{SC} of 17.63 $\pm$ 0.60 mA/cm^2. However, further increasing the height of ITO nanotree degrades device performance. Major decreases in J_{SC} and FF are observed in solar cell devices fabricated with 100 nm and 120 nm ITO nanotree electrodes, which results in PCEs of 3.19 $\pm$ 0.25 and 2.80 $\pm$ 0.40 % respectively, due to dramatic decreases in J_{SC} and FF. The devices with 150 nm ITO nanotree electrodes had no PCE, which is believed to be the result of the taller ITO nanotrees shorting the devices. In summary, the performance of solar cell devices did not have a linear relationship with the height of the ITO nanotree electrode. Instead, an optimum performance was obtained at the 75 nm tall ITO nanotree electrode. The J-V curves of the champion devices for each different ITO nanotree height are depicted in Figure 4.8a, while the photovoltaic

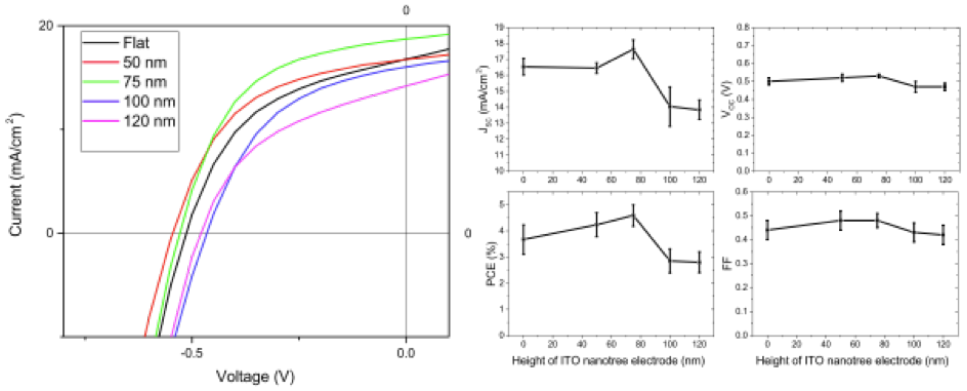

Figure 4.8: The champion J-V curves of inverted solar cells with nanotree GLAD ITO electrodes, and the photovoltaic parameters as a function of the height of ITO nanotree.

parameters, J_{SC}, V_{OC}, PCE, and FF are plotted against the height of ITO nanotrees. The PCE behavior is strongly correlated to J_{SC} and FF, which follows the same trend as the heights of ITO nanotrees were increased.

4.2.4 Mechanism Discussion

The observed solar cell device performance can be explained as a combination of effects due to the high-surface-area electrode: 1) the enhancement of charge extraction due to a shorter collection path; 2) the charge recombination loss resulting from electric field redistribution near and at the ITO nanotree electrode surface; 3) Light trapping by the nanostructured ITO nanotree arrays.

Shorter Electron Pathway

The three-dimensional electrode has been proved to have good compatibility with the BHJ as characterized by SEM above. The nanotree reaches out in the BHJ and provides a shorter pathway for charge carrier transport. For the electrons, instead of travelling all the way through the BHJ to reach the flat electrode, they need only travel to the surface of these nanotrees to be extracted. Diffusion length, which is defined as the distance a charge carrier can travel before recombination, is greatly compensated because the distance the charge carriers need to travel is much shorter. The low resistive pathway provided by the ITO nanotrees facilitate the charge extraction, and reduce the average extraction time. Considering that the hole mobility is much higher in the polymer phase than electron mobility in the fullerene, it is expected that rate of electron extraction can be compensated by reducing the charge transport distance for extraction of electrons relative to holes. The enhancement of FF seen in 50 and 75 nm tall ITO nanotree devices is strong evidence of the enhanced charge extraction. At the same time, a slight increase was seen in J_{SC}, which is attributed to better electric transport with less space charge.

However, the impaired performance of BHJs using taller ITO nanotrees indicates that there are other mechanisms affecting device performance besides simply shortening the electron transport pathways.

Firstly, one should also consider the pathway for the holes in the BHJ: since the charge carriers that generated near the anode, the pathway for holes may be blocked

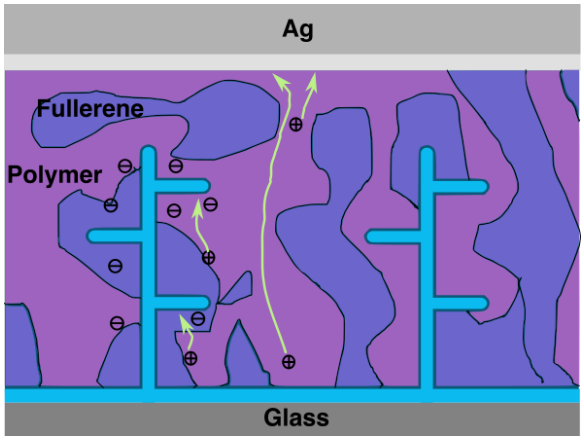

Figure 4.9: Scheme of hole pathway in the BHJ with nanotree GLAD ITO electrodes.

by the ITO nanotrees. As shown schematically in Figure 4.9, the chance of a hole colliding with a nanotree branch increases as the nanotrees are taller. This could potentially increase the bimolecular recombination at the cathode surface, which is consistent with the decreased J_{SC} and FF for 100 and 120 nm tall nanotree electrodes. A compromise between shorter electron transport pathways and hole recombination at the ITO branch interfaces may be the origin of the optimum performance observed at 75 nm. However, it is also important to consider the influence of other factors such as electric field redistribution.

Electric Field Redistribution

The use of three-dimensional branched ITO nanotree electrodes alters the electric field distribution. Earlier work from Ray and coworkers[322] showed electric field redistribution is an important consequence of using a three-dimensional substrate. The change of electric field has several effects on charge collection. Depending on

whether the nanoelectrode is embedded in the desired phase, there may be either a positive or negative impact on solar cell performance since the electric field near the ITO nanotree surface tends to attract electrons to the nanotree surface while repulsing the holes. If the ITO nanotrees are all embedded in the desired phase (PCBM in the inverted solar cells) a positive effect will be observed. However, if the nanotrees are embedded in the donor phase, which transports holes, huge recombination is expected, impairing holes from travelling to the anode. Serious recombination could occur. In total, the overall effect of the electric field could significantly change depending on the percentage of surface area that is surrounded by the desired acceptor material. The larger the surface area embedded in the acceptor phase, the better charge transport and less recombination. As such, the phase distribution plays a critical role here.

Phase Distribution of BHJ

As discussed above the phase distribution in the BHJ is critical to the device performance. In order to increase the surface area that embedded in the desired acceptor phase, C60-SAM is used to form a monolayer on the ZnO hole-blocking layer and make it more favourable for the $PC_{71}BM$ phase to condense at the ITO nanotree surface. The device performance is expected to increase as the percentage of the nanotree surface that is surrounded by the acceptor phase is increased. This can be evidenced when comparing the device performance with and without the C60-SAM layer. For example, in the case of the 50 nm tall ITO nanotree

electrode, if the C60-SAM is not used, J_{SC} is reduced to 15.39 ± 0.48 mA/cm^2, FF reduced to 0.40 ± 0.03, and PCE reduced to 3.08 ± 0.43% compared to those with C60-SAM, where the PCE is found to be 4.24 ± 0.18%. The phase distribution plays an important role in defining the positive or negative effects brought by the nanostructured electrode.

Light Trapping

The branched ITO nanotree structure is believed to trap light in space which can confine more photons in the BHJ by scattering. The external quantum efficiency of organic solar cells are limited by the thickness of the photoactive layer. These scattered photons are then trapped by the nanostructure and absorbed by the donor material and converted to excitons.[323] The light harvesting is enhanced in this manner. This could lead to enhancement of J_{SC} and PCE as well.

In a summary, the observed differences in solar cell device performance results from a complicated competition of several processes due to the high surface area electrode and the use of high-hole-mobility polymer. The shorter electron extraction pathway, the electric field distribution altered by the nanostructured electrode in the BHJ, the donor/acceptor phase distribution, and light trapping by the nanostructured electrode work simultaneously to define the ultimate solar cell device performance. The shorter charge carrier pathway provided by the large-surface-area electrode enhance FF and J_{SC} by promoting charge carrier transport and reducing average charge carrier collection time. The potential redistribution

could induce serious recombination at the ITO nanotree surface if the nanostructured electrode is embedded in the undesired phase. Thus, the donor/acceptor phase distribution is critical as well. In addition, light trapping plays a role in harvesting photons to contribute photocurrent. The solar cell performance is determined by competition of these effects. So, an optimized nanotree height is expected, which is found to be 75 nm experimentally. As the height of ITO nanotrees increased from 0 to 50 nm, J_{SC} and V_{OC} remain almost the same, while FF increases from 0.47 to 0.51. With increasing height of the nanotree and the surface area, the photocarrier collection path becomes shorter, and hence, FF increases rapidly. At this height, better charge extraction outweighs the negative effect of recombination. When increasing the height to 75 nm, J_{SC} increases clearly, while V_{OC} and FF remain the same. The balance of charge extraction and bimolecular recombination reaches the optimum at this point, which led to more balanced electron/hole transport. However, beyond a certain electrode height, a higher chance of the electrode surface being exposed to the donor phase leads to significant recombination loss; The potential distribution in the BHJ when using taller ITO nanotrees become complicated, which could contribute to charge recombination near the ITO nanotree surface. As a result, both V_{OC} and FF decrease with increased height of ITO nanotrees. The significant interface recombination loss is reflected in the 100 and 120 nm high electrode cells. In summary, faster charge extraction dominates and leads to an increased J_{SC} and FF when the ITO nanotrees are under 75 nm in height; on the other hand, at ITO nanotree heights above 75 nm, potential redistribution dominates, resulting in

increased bimolecular recombination, causing significant decrease in V_{OC} and FF.

4.3 Conclusion

In this work, we fabricated solar cells using single-crystalline ITO nanotree electrodes and studied the dependence of nanotree height on solar cell performance. Inverted solar cells were fabricated using the nanostructured electrode and a high-hole-mobility polymer to study the charge extraction behavior. With variation of the height of ITO nanotree, an optimum ITO nanotree height of 75 nm was obtained. We investigated the mechanism and concluded that there are several effects brought by the ITO nanotree that work simultaneously to affect the solar cell performance: the shorter photocarrier pathway provided by the three-dimensional large-surface-area ITO nanotree, potential redistribution in BHJ, vertical phase distribution, and light trapping. The competition of these effects defined the solar cell performance.

4.4 Experimental Section

4.4.1 Materials

ITO coated glass substrates were purchased from Delta Technologies, 8-12W/m^2. The high-hole-mobility polymer PDPP-TT-T-TT (P1) was synthesized according to literature,[118] the molecular weight was measured to be Mw=178 kDa, Mn=13 kDa

using Viscotek TDA305 Triple Detection GPC system by Malvern Instruments Ltd., and chloroform was used as mobile phase. $PC_{71}BM$ was purchased from American Dye Sources; C60-SAM was purchased from One-Material Inc. All the solvents were purchased from Sigma Aldrich. All the materials and solvent were used as received without further treatment unless otherwise stated.

4.4.2 Nanostructured Electrode Deposition

All the nanostructured electrodes were fabricated on commercially available flat ITO-coated substrates. The flat ITO slides were cleaned successively by 10 min ultrasonication in dimethyl chloride, Millipore deionized water, and 2-propanol. Before ITO nanotree deposition, the flat substrates were dried in nitrogen flow and 10 min air plasma (100 mTorr). GLAD method can be found in reference[16]. The height of the ITO nanotree was controlled by changing deposition time.

A thin layer of ZnO (∼8 nm)was coated onto ITO nanotree electrode by atomic layer deposition. ZnO was grown using a low temperature ALD reactor (Kurt J. Lesker 150LX). The substrate temperature was maintained at 53 °C and the chamber pressure was kept at 1.07 Torr during thin film growth. Diethylzinc (Sigma-Aldrich >99.99%) was utilized as precursor for zinc and water vapor was used as oxidant species. The alternating precursor pulses width/purge times were, respectively, diethylzinc (0.03/5 s) and water vapor (0.5/10 S). Accordingly, 8 nm thick zinc oxide was grown under steady growth per cycle of 0.075 nm. The growth per cycle (GPC) was resolved using an in-situ spectroscopic ellipsometry (J.A. Woollam M2000DI)

during growth on the planar structure.

4.4.3 Photovoltaic Devices Fabrication

A solution of PDPPTT-T-TT:$PC_{71}BM$ 1:2, 20 mg/ml total in $CHCl_3$: *o*-dichlorobenzene (ODCB) was prepared in the glovebox and stirred at $\sim$70°C for several hours. 1 mM solution of fullerene derivative, C60-SAM in a 1:1 (v: v) cosolvent tetrahydrofuran:chlorobenzene (THF:CB) was prepared. A self-assembled monolayer was formed on the surface of the ITO nanotree electrode/ZnO surface by immersing into the solution for 10 min followed by thorough rinse with THF:CB and acetone. PDPPTT-T-TT:PCBM films were spin-cast onto the electrode at 1500 rpm for 60s before being sealed in a petri-dish in dark to dry. Samples were then transported in a sealed glass vial to a nitrogen glovebox for thermal evaporation of metal contact. At base pressure of 5×10^{-6} Torr, MoOx/Ag/Mg contacts were evaporated subsequently a rate of 0.1 Å s^{-1}, 2.0 Å s^{-1} and 2.5 Å s^{-1}, respectively. The device area was 0.155 ± 0.008 cm^2. The PV characteristics of the OPV devices were characterized at 25–30 °C in air under simulated AM1.5 G conditions (Xenon source from Oriel 91191 1000 W) equipped with a custom made water filter and calibrated to a certified Si reference cell with a KG-5 filter (PV Measurements, PVM624). The light intensity was then subsequently measured immediately proceeding any J-V curves using a thermopile (XL2-3S-H2). J–V characteristics were recorded using a computer-controlled Keithley 2400 source meter. ITO nanotree electrodes were characterized with a Hitachi S-4800

scanning electron microscope (SEM). Optical properties were quantified by UV–vis transmission measurements using a Perkin-Elmer Lambda 900 UV/vis/NIR spectrometer for a window framing the visible wavelengths.

5

Summary and Outlook

5.1 Thesis Summary

In this thesis, three approaches to investigate three important components of OSCs and the fundamental photovoltaic process were studied and discussed. Chapter 1 introduced the topic of OSCs and explained why such research is desirable to pursue. Chapter 2 focused on the photoactive layer and described the development of organic small molecules as photon-absorbing materials for OSCs. Chapter 3 focused on the interfacial modifier of OSCs. A low-band-gap interfacial modifier was developed to improve the solar cell performance and the mechanism behind its

effects was investigated. Chapter 4 described not only a novel electrode design, but also covered the topic of an overall device engineering approach including device structure design, interface engineering, and charge carrier mobility in the BHJ. In this final chapter, the work of these chapters is summarized and future research directions are suggested. A brief outlook is presented with regard to the commercial applications of OSCs as well.

5.1.1 Chapter 1

The first chapter introduced OSCs and current research progress. There is a strong need to develop renewable energy sources to meet increasing global energy requirements. Solar energy stands out as a promising renewable energy source since one hour of sunshine on the earth could power the world for an entire year. The development of photovoltaic cells was reviewed, including the pioneer silicon solar cells, second generation thin film solar cells, and emerging third generation solar cells. While the conventional inorganic-type solar cells are rigid, expensive, and often contain toxic materials, OSCs succeed in being lightweight, inexpensive, easy to process and compatible with flexible applications. To evaluate and compare solar cell performance, the standard characterization of solar cell devices was introduced. Critical photovoltaic parameters including J_{SC}, V_{OC}, FF and PCE were explained under simulated solar radiation conditions. The operating principle of OSCs was introduced and the structure of an OSC device was deconstructed to three critical components: the photoactive materials, the interfacial materials, and the electrodes.

Each component of OSC devices was thoroughly discussed and reviewed. The function and importance of each component was addressed. A brief history was reviewed while major benchmarks and significant advances were highlighted.

5.1.2 Chapter 2

Chapter 2 described the synthesis of two conjugated small molecules used as photon-absorbing materials in OSC. The motivation of developing conjugated small molecules is to take advantage of the ease of synthesis and mono-dispersity of such molecules compared to polymers. Based on the donor-acceptor concept, two isostructural low-band-gap small molecules were designed and synthesized with a one-atom substitution, S for Se (**1** and **2**). The two molecules both contain the electron-rich central unit benzo[1,2-b:4,5-b′]dithiophene. The effect of one-atom substitution on the optoelectronic properties and photovoltaic performance of devices was investigated. One-atom substitution engendered substantial differences in the physical and electro-optical properties. A small but measurable effect on the energy of frontier molecular orbitals (HOMO and LUMO) was observed. One atom substitution shifts the absorption profile of the molecules, both neat and when mixed in a BHJ with $PC_{71}BM$. The bandgap of **1** and **2** were measured to be 1.7 eV and 1.6 eV, respectively. OSCs were fabricated using **1** or **2**:$PC_{71}BM$, and the photovoltaic performance was measured and compared. The solubilities are different between **1** and **2**: at room temperature the solubility of **1** and **2** in chloroform are 20 and 40 mg/mL, respectively. Therefore, **1**:$PC_{71}BM$ needs to

be processed at a high temperature to increase the solubility. The Se-containing variant **2** led to higher efficiencies [highest power conversion efficiency (PCE) of 2.6%] in a standard organic photovoltaic architecture, when combined with $PC_{71}BM$ after a brief thermal annealing, than the S-containing molecule **1** (highest PCE of 1.0%). Brief thermal annealing resulted in rotation of the crystalline grains of both molecules to more energetically favorable configurations. Studies of the resulting morphologies of BHJs based on 1 and 2 showed that one-atom substitution could engender important differences in the solubilities, which then influenced the crystal orientations of the small molecules within this thin layer.

5.1.3 Chapter 3

In this chapter, an interfacial material PBDTTPD-COOH was synthesized and applied to several OSCs to improve efficiency. While several low-band-gap polymers with different HOMO levels were chosen to pair with this interfacial modifier, enhanced device performance was only seen in two polymers. The mechanism behind the performance enhancement was investigated and a guideline for choosing the correct interfacial material/donor polymer pair was provided. The PBDTTPD-COOH interfacial modifier was based upon the backbone of the established donor polymer, PBDTTPD, but has appended alkyl carboxylic acid side chains. Three BHJs composed of a donor polymer and $PC_{71}BM$ were examined, including the donor polymers PBDTTPD, PCDTBT, and PTB7 within the following OPV device stack: ITO/(interfacial layer or layers)/BHJ/LiF/Al/Mg. The PBDTTPD-based

modifier of the PEDOT:PSS layer resulted in statistically significant increases of efficiency for PBDTTPD- and PCDTBT-based donor polymer:$PC_{71}BM$ BHJs, but not for PTB7:$PC_{71}BM$ BHJ. Electronic and morphological effects were considered with regard to the origin of this phenomenon. Energy level diagrams for these three different polymers relative to the ITO/PEDOT:PSS/PBDTTPD-COOH electrode showed there was no energy barrier for hole extraction from donor polymer to ITO anode in all three polymer/substrate pairs, and thus the observed discrepancy was most likely not electronic in origin. ToF-SIMS depth profiling and surface energy measurements, however, strongly suggested that the observed effects of the PEDOT:PSS/interfacial layer were driven by changes in the local composition of the BHJ at this interface. For both the PBDTTPD- and PCDTBT-based BHJs, favorable accumulation of the donor polymer at the PEDOT:PSS/interfacial layer resulted in higher device efficiency; no similar change of the BHJ composition was observed for the PTB7-based BHJ. In this work, the device performance of groups of identically prepared devices was compared using a K-sample Anderson-Darling test to enable comparison in a statistically quantifiable manner, and the data were visually presented as average shifted histograms.

5.1.4 Chapter 4

The chapter presented an approach for overall solar cell engineering using a high-hole-mobility polymer and nanostructured ITO electrodes. The charge carrier properties and the effect brought by the nanostructured electrode were investigated

and discussed. The single-crystalline nanostructured ITO electrodes adopted a nanotree-like structure and were grown by glancing angle deposition on planar ITO coated glass. Overall device engineering was achieved by integrating the nanostructured ITO electrode with a high-hole-mobility polymer into an inverted solar cell configuration in order to achieve balanced electron/hole extraction and collection. Interface engineering was carried out to fulfill the requirement for inverted solar cell design by adopting atomic layer deposited ZnO to conformally coat the ITO nanotree. The ZnO-coated surface was further treated with a fullerene derivative, C60-SAM to form a self-assembled monolayer in order to control the surface energy. ITO nanotrees with the height of 50, 75, 100, and 120 nm were screened to make solar cells. Enhancement was obtained for the devices fabricated with 50 and 75 nm ITO nanotree electrodes, while reduced performance was obtained for devices with 100 and 120 nm ITO nanotree electrodes. The optimal efficiency was obtained using 75 nm nanotree ITO electrode. The control devices built on planar ITO coated glass performed an average PCE of 3.67± 0.56% with J_{SC} of 16.54 ± 0.52 mA/cm^2, V_{OC} of 0.52 ± 0.01 V, and FF of 0.47 ± 0.01. The PCE was enhanced to 4.59 ± 0.41%, with J_{SC} of 17.63 ± 0.60 mA/cm^2, V_{OC} of 0.53 ± 0.01 V, and FF of 0.48 ± 0.03 when the 75 nm ITO nanotree electrode was used. Investigation on the underlying mechanism indicated that the insertion of the ITO nanotrees into BHJ had several complicated effects that could determine the device performance. Shortening the electron extraction pathway, altering the potential distribution throughout the BHJ, and trapping light for photon harvesting

were all found to affect the photovoltaic performance. More importantly, the charge carrier recombination at the ITO electrode interface induced by these effects listed above played a critical role in defining the solar cell device performance. Only when these effects reached an optimum, could an optimal device performance be obtained. In this work, 75 nm was the optimal ITO nanotree height with effective charge extraction, desired phase distribution and a reasonable rate of the charge carrier recombination near the ITO nanotree surface.

5.2 Future Work

5.2.1 Mechanism of Crystallite Reorientation in Small Molecule /$PC_{71}BM$ Photoactive Layer During Thermal Annealing

The molecular arrangement of the conjugated molecules is critical to the optical and charge transfer events in organic electronics.[259,317,324,325] Further study on the recrystallization in the small molecule OSC BHJ described in Chapter 2 would provide a guideline for structural requirements for efficient OSCs. The importance of the structure-property relationship has been addressed over the past years.[17,326] Figure 5.1 shows the nanoscale, mesoscale, and macroscale structures in organic electronics.[17] In the molecular level, the conjugated molecules arrange themselves in a low-energy equilibrium packing configuration. For example, in BHJ solar cells the packing of the π conjugated polymer is characterized to have two packing

directions: the π-π stacking direction and the interdigitation of the alkyl side chains.[98] At the nanoscale, the polymer/small molecule packing forms crystalline grains and the crystalline grains co-exist with the amorphous phase. In a larger scale, phase segregation between the donor and acceptor phase forms an intermixed and percolated matrix in the BHJ and therefore, the nano- and micro-structures determine the percolation in the BHJ, thus the solar cell performance. Efforts have been directed to studying the mechanism of film growth and crystallization to make high-performance OSCs.[327,328] Tumbleston and coworkers discovered that the degree of molecular orientation at the donor/acceptor interface is an important parameter in realizing high-performance, fullerene-based OSCs.[329] They used soft X-ray scattering to characterize and distinguish the face-on and edge-on orientation at the heterointerface and discovered methods that can promote the favored orientation. It was shown that the degree of the molecular orientation could be manipulated by molecular structure design as well as the processing solvent control. Other research showed that the edge-on oriented molecules showed high hole mobilities in organic field-effect transistors, while the radially oriented molecules exhibited high photovoltaic properties in organic photovoltaic cells.[330]

Thus, manipulating and controlling the crystallization behavior is critical in promoting the solar cell efficiency. Other than changing the chemical structure and the processing solvent, post-deposition annealing, including solvent annealing and thermal annealing, could also tune the molecular orientation of polymers and small molecules oreintation in BHJ[309,331,332] An early study found that annealing at 150°C

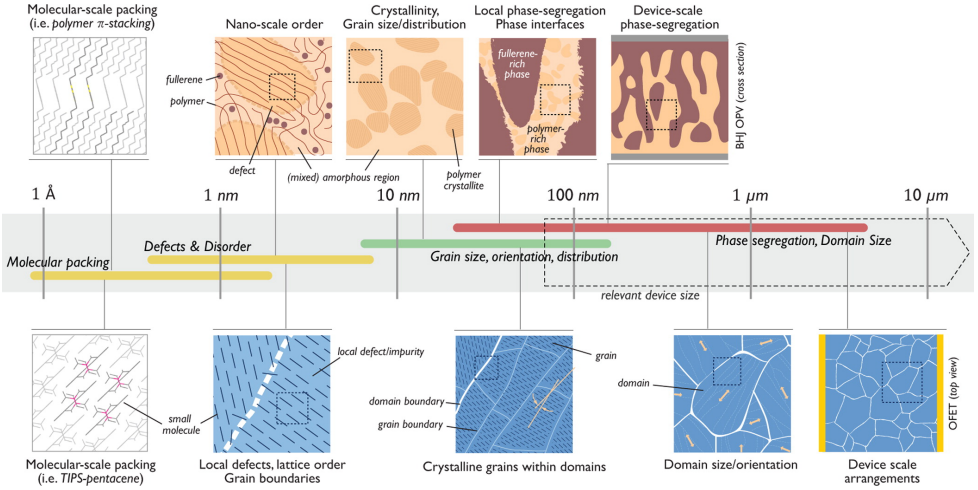

Figure 5.1: Size scale and relevant morphology features in organic electronic devices. Reprinted with permission from reference.[17] Copyright 2012 by American Chemical Society.

could increase the P3HT crystallite size and enhance the PCE of the P3HT:PCBM solar cell from 0.8% to 3.2%.[98] It is noticeable that during the annealing process, the sample was heated to an elevated temperature and then cooled down to room temperature. Both the heating and cooling processes could result in the change in the crystallinity and orientation of the crystalline domains. It is worth studying and understanding the behavior of the molecules during these processes. For example, Bau and coworkers conducted in-situ grazing incidence X-ray scattering (GIXS) to study the morphology and crystalline structure of P3HT:PC_{61}BM BHJ in a range of temperatures from room temperature up to 220 °C.[102] The critical temperature for crystallite reorientation was obtained for pure phase film and the mixed BHJ.

In Chapter 2, we reported an interesting crystallite reorientation behavior upon thermal annealing for the small molecule (**1** and **2**)/PC_{71}BM solar cells. For

2:$PC_{71}BM$, spin-casting the small molecule:$PC_{71}BM$ solution at room temperature and 80 °C led to different crystalline structures as seen from the GIXRD spectra. This initial crystalline structure subsequently determined the thermal annealing effects. While no crystallite reorientation was observed for the room temperature samples, obvious crystallite reorientation occurred for the 80 °C processed sample. Enhancement of PCE was obtained in the devices that underwent crystallite reorientation. For 1:$PC_{71}BM$ devices which were processed at 80 °C, the crystallites underwent reorientation upon annealing. However, the PCE was not improved by this process. Limited by the solubility, **1**:$PC_{71}BM$ could not be processed at room temperature as a comparison. As the results suggested, the BHJ processed at elevated temperature is more likely to undergo crystallite reorientation. However, the mechanism that leads to this behavior is still under investigation. Investigation of this behavior based on chemical structure is of interest to better understand the structure-efficiency relationship. In-situ wide angle X-ray diffraction is suggested here to characterize the crystallite transition behavior. Both in-plane and out-of-plane crystallite orientation could be obtained using wide-angle X-ray diffraction. The crystallite reorientation and transition could be monitored both in the initial BHJ before annealing as well as during the annealing process. Moreover, the in-situ monitoring of the crystallite transition could be used to obtain the critical transition temperature. The relationship of the microstructure to the BHJ morphology could be set up and understood. The relative influence of the small molecule's melting point, the glass transition temperature of the PCBM, and the blend ratio of

small molecule/$PC_{71}BM$ with relationship to the molecule structure could provide a guideline for the optimization of processing conditions for solar cell device fabrication.

5.2.2 Distinguish the Origin of J_{SC} Enhancement in OSCs with ITO NT Electrodes

In Chapter 4, the comprehensive effects of nanostructured electrodes on the performance of OSC devices are studied and summarized. Both effective charge transport and light trapping account for the J_{SC} enhancement. However, the relative contribution of each factor is not distinguished. First, the nanostructured ITO electrodes occupy physical space in the BHJ. The volume of the ITO NTs should be calculated and excluded. Solar cells with the same amount of BHJ material excluding ITO NT volume then can be compared. Second, additional light scattering and absorption can be caused be the NTs. This can be measured by comparing the absorbance profiles of BJHs with and without ITO NTs. By subtracting the additional absorption from the total absorption, the effect of the effective charge transport could be distinguished. A better understanding of charge carrier transport in BHJ can then be achieved.

5.2.3 Spray-Cast Thick Film OSCs

Here, a thick photoactive layer OSC faciliating spray-casting method is proposed to achieve high photovoltaic performance. The critical photon to electricity conversion procedure includes photon absorption, exciton generation, electron and hole separation, free charge carrier transport, and charge carrier extraction.[79,255] The thickness of the OSCs is limited by the diffusion length of low mobility charge carriers.[333] Traditionally, the thickness of polymer:PCBM solar cells is less than 150 nm to compromise for the short charge carrier diffusion length. For example, 75 nm has been reported to be the optimal thickness for PCDTBT:PCBM solar cells and several groups have obtained 6-7% PCE with this photoactive layer thickness.[111,334] However, the thin active layer limits light harvesting efficiency.[335] To resolve this dilemma, the use of high-hole-mobility polymer could make the fabrication of thick OSC devices possible.[336] In OSCs, free carrier transport is governed by the charge carrier mobility and the free charge carrier diffusion length. The charge carrier diffusion length is defined as the mean distance over which the charges can move before significant recombination occurs.The diffusion can be expressed as:

$$L_{diffusion} = \sqrt{D\tau} = \sqrt{\mu\tau kT/e}$$

where μ is the charge carrier mobility; τ is the charge carrier lifetime; D is the diffusion coefficient; k is the Boltzmann constant; e is the electron charge. The equation indicates that the $\mu\tau$ product determines the average distance the charge

carrier can travel before recombination.[91] Therefore, the polymer, PDPPTT-T-TT, which was introduced in Chapter 3 and has a hole mobility of 1.42 $cm^2/(V \cdot s)$ could be used in as a high-hole-mobility donor in achieving thick OSC devices. The hole mobility of PDPPTT-T-TT is 1.42 $cm^2/(V \cdot s)$ compared to that of P3HT which is in the order of 10^{-3} $cm^2/(V \cdot s)$. Thus the average distance that the hole can travel in PDPPTT-T-TT before recombination is 30 times longer than that in P3HT based BHJ solar cells. Given the general thickness of polymer solar cells are about 100 nm, the device with PDPPTT-T-TT could be as thick as 3 μm. Indeed, the thick devices require a nanostructured ITO electrode for electron extraction to obtain the balanced charge extraction. In this way, the low intrinsic electron mobility could be compensated because the electron pathway could be much shorter since the nanotree electrode could reach out three-dimensionally into the BHJ.[337] However, as discussed in in Chapter 3, the influence of inserting ITO nanotree structures into the BHJ is complicated and a few factors would possibly impair solar cell performance. Hence, it is necessary to use the simulation and computational results as a geometry guide to achieve a simpler electrode design. Moreover, it has been shown that the field at the nanostructure interface is the key to electron extraction since the single crystalline ITO nanostructure allows electrons to diffuse freely, hence the interface requires further engineering to improve charge extraction.[337] Furthermore, spray casting is a suitable method to make the thick BHJ layer solar cells as proposed above. There are several advantages:[308,338–341] first of all, spray casting could make thicker films than spin-casting. A regular spin-casting method

is not capable of making films thicker than 300 nm, due to the solubility of materials and the nature of the fast spin-casting technique. Second, spray casting easily provides a robust film with desired thickness.[342–344] Third, spray casting is suitable for large scale manufacturing.[336,345]

5.2.4 Stability and Degradation Mechanism in OSCs

Efficiency, ease of processing, and stability are three import indices for evaluating the application of OSCs. The record efficiency of OSCs has reached 10%.[26] The robust manufacturing techniques, such as spray casting, ink injecting and roll-to-roll production, have been adopted to fabricate OSCs.[346] The critical issue that limits the application and commercialization of OSCs is stability. Compared to inorganic silicon solar cells which can be stable for over 25 years, organic materials are naturally more susceptible to chemical degradation.[347] Polymer photodegradation, water diffusion, and oxidation can all affect the lifetime and stability of the OSC devices.[286] Figure 5.2 shows some degradation processes that could take place in a typical OSC device. The metallic electrode, typically aluminum, could react with water/oxygen and degrade. Water and oxygen could penetrate into the BHJ and react with the polymer. The photodegradation and thermal degradation of the polymer are also major causes of device failure.[348] PEDOT:PSS, the most common interfacial material in the forward solar cell configuration, is very sensitive to water and oxygen because of its acidic and hydophilic nature.[349] Furthermore, the performance of the OSC strongly depends on the micro-phase separation and the interconnected

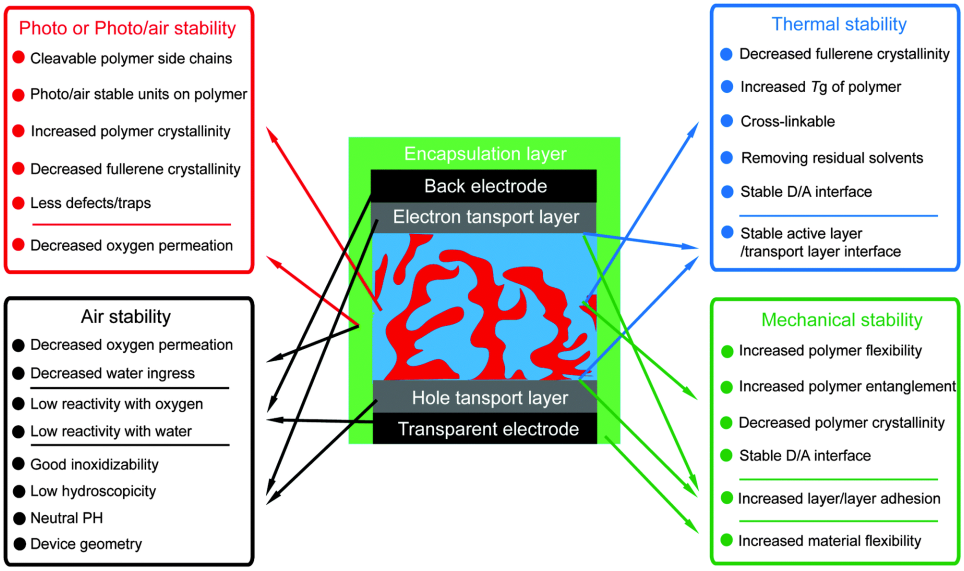

Figure 5.2: Schematic diagram of the strategies to increase stability. Reprinted with permission from reference.[18] Copyright 2016 by the Royal Society of Chemistry.

pathway formed in BHJ, however, this structure formed during fabrication may not be the most stable. As a result, the structural change may occur especially when heated.[350]

There are several approaches to improving the OSC device stability. Figure 5.2 lists the strategies that could improve the stability of OSC in terms of unstable morphology, diffusion of electrodes and buffer layer, oxygen and water, irradiation and mechanical stress.[18] These approaches can be summarized into two catergories: the chemical development of stable materials and physical external encapsulation. Efforts into the development of both air-stable photoactive materials[351–355] and interfacial materials[82,356–359] are continuing. For example, developing air-stable interfacial material to replace the unstable PEDOT:PSS is

an option for stability enhancement.[360] As mentioned in the introduction chapter, the inverted PCDTBT:PCBM solar cell design, which uses ZnO and MoOx as the interfacial layers, could retain 80% of the initial performance after one month in air. Encapsulation is another effective approach to protecting materials from environmental effects. The exposure to water and oxygen can be minimized, prolonging the lifetime of the devices.[18]

For the small molecule solar cells and the polymer solar cells presented in this thesis, the next step is to study device degradation and stability. The introduction of acid molecules, such as C60-SAM and PBDTTPD-COOH may act as a chemical reactive factor that limits the device stability.[285] The long-term stability and degradation mechanism should be studied and evaluated controlling humidity and temperature of the atmosphere. Ultimately, by understanding the degradation mechanism, an effective chemical approach or physical encapsulation could be developed to ensure long-term stability.[18]

5.3 Outlook

The growing concerns about climate change and alternative sources of energy have led to the significant growth of the photovoltaic market.[29] A recent Fraunhofer Institute for Solar Energy Systems's Photovoltaics Reports shows that the total photovoltaic installation has reached 240 GWp (Gigawatt-peak) in 2015 with an annual growth rate of 41% from 2008 to 2015.(Figure 5.3). While the current

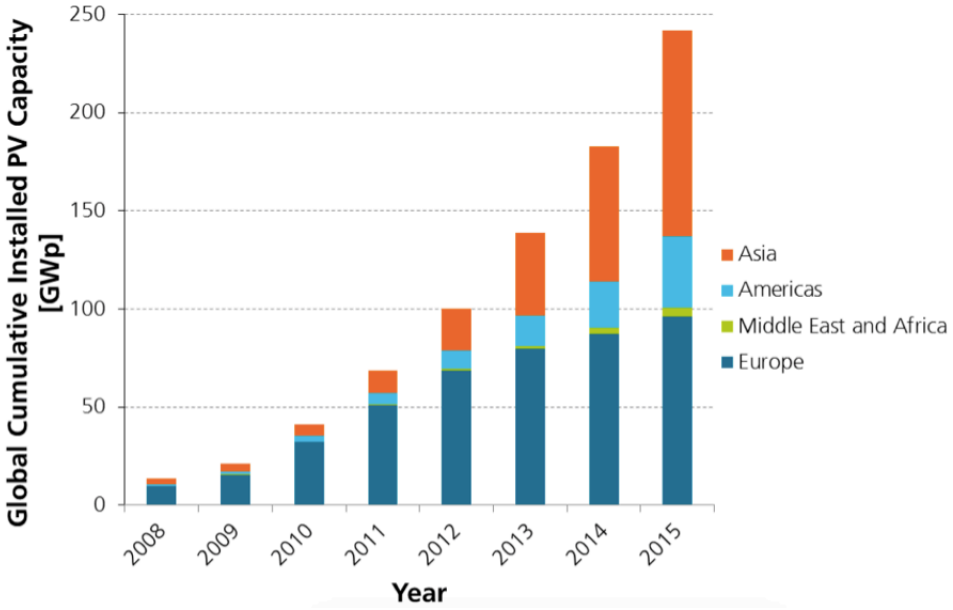

Figure 5.3: Global cumulative photovoltaic installation from 2008 to 2015. Reprinted with permission from 'Photovoltaics Reports'. Copyright 2016 by Fraunhofer ISE.

photovoltaic market is dominated by silicon solar cells (> 90%),[29] the major factor hindering the growth of this market is the demand for high quality and low priced products. The cost reduction demand in the industry drives increasing research on low-manufacturing-cost OSCs.[361] Figure 5.4 compares the attributes of all three solar cell generations.[362] The first generation (crystalline and amorphous silicon) and second generation (CIGS and CdTe) have higher efficiencies and longer lifetime than the third generation. However, OSC (or OPV) outperforms on printability and flexibility.

The organic solar cells market is growing at a steady rate, and this rate is forecasted to remain in the next 10 years as shown in Figure 5.5.The estimated mass-production is expected to reach 194 Mw in 2020.[363] A total OSC market value of

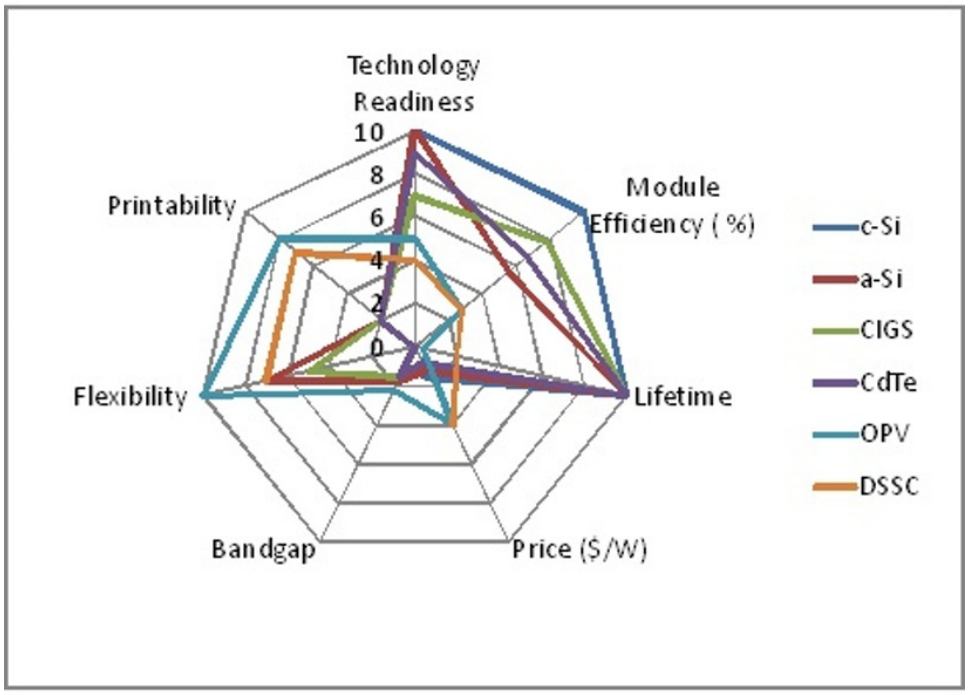

Figure 5.4: A radar chart comparing attributes of different PV technologies. Reprinted with permission from 'Organic Photovoltaics (OPV) 2013-2023: Technologies, Markets, Players'. Copyright 1996-2016 by IDTechEx.

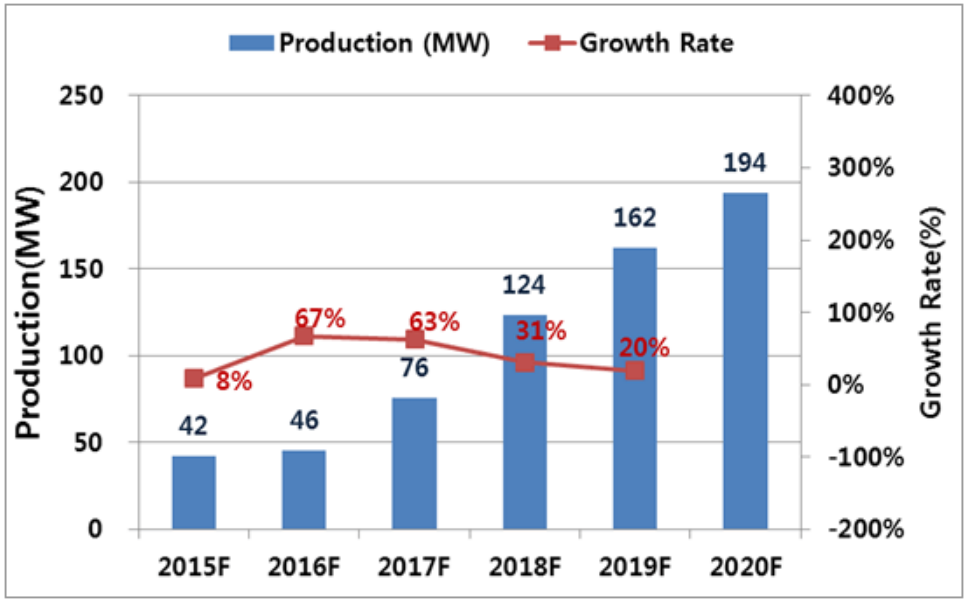

Figure 5.5: Projected OPV production and growth rate (2015-2020). Reprinted with permission from 'Next Generation OPV Technology Trend and Market Forecast'. Copyright 2015 by Electronics.ca Publication.

$87 million is expected by 2023.[362]

While the challenge remains in the efficiency and lifetime, the selling point of OSC lies in their unique and distinct features such as light weight, freedom in shape, substrate and color, semi-transparency, and shorter processing lead time.[363,364]

Figure 5.6 shows an example of the roll-to-roll technology that can print OSCs in a large-scale, robust, and affordable manner, achieved by Commonwealth Scientific and Industrial Research Organization (CSIRO) in Australia. It is reported that solar cells could be printed every two seconds.[365]

Heliatek Inc. has commercialized their building integrated photovoltaics (BIPV). BIPV integrates organic solar films in glass to collect solar energy.[366]

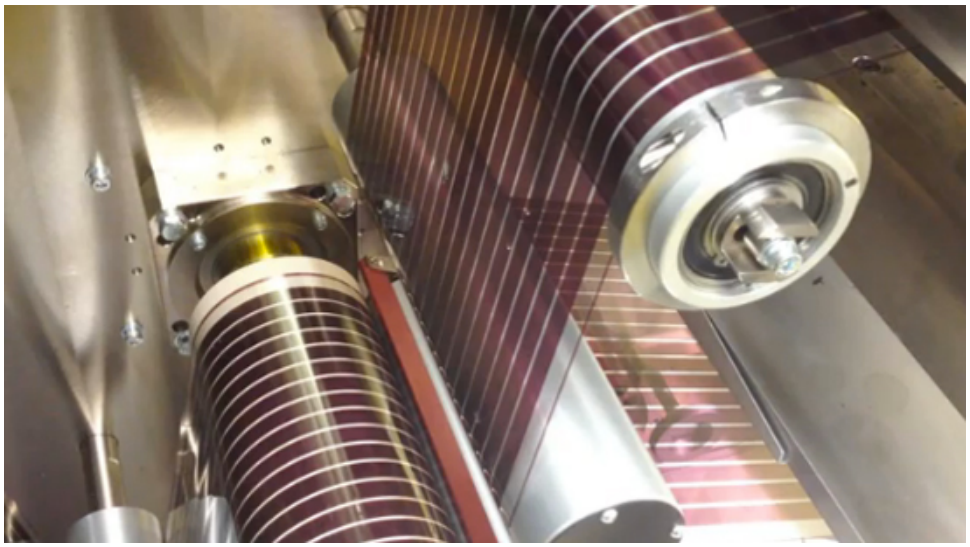

Figure 5.6: Roll-to-roll production of flexible OSCs. Image is reproduced with permission from CSIRO Australia. Copyright 2015 by CSIRO Australia.

As a result, the sides of buildings, including windows, can be used to collect solar energy, much more square footage and energy collection opportunities than just rooftop collection.

In summary, OSCs could and should find their own distinct applications from other solar cell technologies for further industry development, such as for recharging mobile electronics in off-grid scenarios. Devices such as the Heli-on phone charger recently introduced by infinityPV (Figure 5.7), which allow consumers to escape inconveniences experienced while off-grid, can ultimately be applied to other situations where minor (i.e. non-industrial) amounts of energy will be needed but grid connection is inconvenient or implausible.

Figure 5.7: Image of Heli-on flexible phone charger. Image is reproduced with permission from InfinityPV. Copyright 2016 by infinityPV.

References

[1] Darling, S. B.; You, F. *RSC Advances* **2013**, *3*, 17633–17648.

[2] Bura, T.; Leclerc, N.; Fall, S.; Lévêque, P.; Heiser, T.; Retailleau, P.; Rihn, S.; Mirloup, A.; Ziessel, R. *Journal of the American Chemical Society* **2012**, *134*, 17404–17407.

[3] Liu, Y.; Yang, Y. M.; Chen, C.-C.; Chen, Q.; Dou, L.; Hong, Z.; Li, G.; Yang, Y. *Advanced Materials* **2013**, *25*, 4657–4662.

[4] Zhang, Q. et al. *Nature Photonics* **2015**, *9*, 35–41.

[5] Liu, J.; Sun, Y.; Moonsin, P.; Kuik, M.; Proctor, C. M.; Lin, J.; Hsu, B. B.; Promarak, V.; Heeger, A. J.; Nguyen, T.-Q. *Advanced Materials* **2013**, *25*, 5898–5903.

[6] Zhou, J.; Zuo, Y.; Wan, X.; Long, G.; Zhang, Q.; Ni, W.; Liu, Y.; Li, Z.; He, G.; Li, C.; Kan, B.; Li, M.; Chen, Y. *Journal of the American Chemical Society* **2013**, *135*, 8484–8487.

[7] Zhou, H.; Yang, L.; You, W. *Macromolecules* **2012**, *45*, 607–632.

[8] Sun, Y.; Welch, G. C.; Leong, W. L.; Takacs, C. J.; Bazan, G. C.; Heeger, A. J. *Nature Materials* **2012**, *11*, 44–48.

[9] Love, J. A.; Nagao, I.; Huang, Y.; Kuik, M.; Gupta, V.; Takacs, C. J.; Coughlin, J. E.; Qi, L.; van der Poll, T. S.; Kramer, E. J.; Heeger, A. J.; Nguyen, T.-Q.; Bazan, G. C. *Journal of the American Chemical Society* **2014**, *136*, 3597–3606.

[10] Kyaw, A. K. K.; Wang, D. H.; Wynands, D.; Zhang, J.; Nguyen, T.-Q.; Bazan, G. C.; Heeger, A. J. *Nano Letters* **2013**, *13*, 3796–3801.

[11] He, X.; Cao, B.; Hauger, T. C.; Kang, M.; Gusarov, S.; Luber, E. J.; Buriak, J. M. *ACS Applied Materials & Interfaces* **2015**, *7*, 8188–8199.

[12] Zhang, W.; Zhao, B.; He, Z.; Zhao, X.; Wang, H.; Yang, S.; Wu, H.; Cao, Y. *Energy & Environmental Science* **2013**, *6*, 1956–1964.

[13] Meng, B.; Fu, Y.; Xie, Z.; Liu, J.; Wang, L. *Macromolecules* **2014**, *47*, 6246–6251.

[14] Xu, Q.; Wang, F.; Qian, D.; Tan, Z.; Li, L.; Li, S.; Tu, X.; Sun, G.; Hou, X.; Hou, J.; Li, Y. *ACS Applied Materials & Interfaces* **2013**, *5*, 6591–6597.

[15] Cao, B.; He, X.; Fetterly, C. R.; Olsen, B. C.; Luber, E. J.; Buriak, J. M. *ACS Applied Materials & Interfaces* **2016**, *8*, 18238–18248.

[16] Beaudry, A. L.; LaForge, J. M.; Tucker, R. T.; Sorge, J. B.; Adamski, N. L.; Li, P.; Taschuk, M. T.; Brett, M. J. *Nano Letters* **2014**, *14*, 1797–1803.

[17] Rivnay, J.; Mannsfeld, S. C. B.; Miller, C. E.; Salleo, A.; Toney, M. F. *Chemical Reviews* **2012**, *112*, 5488–5519.

[18] Cheng, P.; Zhan, X. *Chemical Society Reviews* **2016**, *45*, 2544–2582.

[19] *2015 World Energy Outlook Special Report on Energy and Climate Change*.

[20] Melillo, J. M.; Terese, R.; Gary, Y. *Climate Change Impacts in the United States: The Third National Climate Assessment.*; 2014.

[21] Lewis, N. S.; Nocera, D. G. *Proceedings of the National Academy of Sciences* **2006**, *103*, 15729–15735.

[22] Becquerel, *Comptes Rendus de L´Academie des Sciences* **1839**, *9*, 145–149.

[23] Chapin, D. M.; Fuller, C. S.; Pearson, G. L. *Journal of Applied Physics* **1954**, *25*, 676–677.

[24] Goetzberger, A.; Hebling, C.; Schock, H.-W. *Materials Science and Engineering: R: Reports* **2003**, *40*, 1–46.

[25] Bahrami, A.; Mohammadnejad, S.; Soleimaninezhad, S. *Optical and Quantum Electronics* **2012**, *45*, 161–197.

[26] Green, M. A.; Emery, K.; Hishikawa, Y.; Warta, W.; Dunlop, E. D. *Progress in Photovoltaics: Research and Applications* **2015**, *23*, 1–9.

[27] Polman, A.; Knight, M.; Garnett, E. C.; Ehrler, B.; Sinke, W. C. *Science* **2016**, *352*, aad4424.

[28] Green, M. *Semiconductor Science and Technology* **1993**, *8*, 1–12.

[29] Smith, D. D. et al. Generation III high efficiency lower cost technology: Transition to full scale manufacturing. 2012 38th IEEE Photovoltaic Specialists Conference (PVSC). 2012; pp 001594–001597.

[30] Guenes, S.; Neugebauer, H.; Sariciftci, N. S. *Chemical Reviews* **2007**, *107*, 1324–1338.

[31] Yan, J.; Saunders, B. R. *Rsc Advances* **2014**, *4*, 43286–43314.

[32] Grätzel, M. *Journal of Photochemistry and Photobiology C: Photochemistry Reviews* **2003**, *4*, 145–153.

[33] Kamat, P. V. *Journal of Physical Chemistry C* **2008**, *112*, 18737–18753.

[34] Liu, Y.; Zhao, J.; Li, Z.; Mu, C.; Ma, W.; Hu, H.; Jiang, K.; Lin, H.; Ade, H.; Yan, H.

Nature Communications **2014**, *5*, 5293.

[35] Ma, W.; Yang, G.; Jiang, K.; Carpenter, J. H.; Wu, Y.; Meng, X.; McAfee, T.; Zhao, J.; Zhu, C.; Wang, C.; Ade, H.; Yan, H. *Advanced Energy Materials* **2015**, *5*, 1501400.

[36] Etxebarria, I.; Ajuria, J.; Pacios, R. *Organic Electronics* **2015**, *19*, 34–60.

[37] Chuang, C.-H. M.; Brown, P. R.; Bulović, V.; Bawendi, M. G. *Nature Materials* **2014**, *13*, 796–801.

[38] Søndergaard, R. R.; Hösel, M.; Espinosa, N.; Jørgensen, M.; Krebs, F. C. *Energy Science & Engineering* **2013**, *1*, 81–88.

[39] Hecht, D. S.; Hu, L.; Irvin, G. *Advanced Materials* **2011**, *23*, 1482–1513.

[40] Langley, D.; Giusti, G.; Mayousse, C.; Celle, C.; Bellet, D.; Simonato, J.-P. *Nanotechnology* **2013**, *24*, 452001.

[41] Green, M. A.; Ho-Baillie, A.; Snaith, H. J. *Nature Photonics* **2014**, *8*, 506–514.

[42] Gao, P.; Graetzel, M.; Nazeeruddin, M. K. *Energy & Environmental Science* **2014**, *7*, 2448–2463.

[43] Kojima, A.; Teshima, K.; Shirai, Y.; Miyasaka, T. *Journal of the American Chemical Society* **2009**, *131*, 6050–6051.

[44] Heo, J. H.; Im, S. H.; Noh, J. H.; Mandal, T. N.; Lim, C.-S.; Chang, J. A.; Lee, Y. H.; Kim, H.-j.; Sarkar, A.; Nazeeruddin, M. K.; Grätzel, M.; Seok, S. I. *Nature Photonics* **2013**, *7*, 486–491.

[45] Kim, H.-S.; Lee, C.-R.; Im, J.-H.; Lee, K.-B.; Moehl, T.; Marchioro, A.; Moon, S.-J.; Humphry-Baker, R.; Yum, J.-H.; Moser, J. E.; Grätzel, M.; Park, N.-G. *Scientific*

Reports **2012**, *2*.

[46] Lee, M. M.; Teuscher, J.; Miyasaka, T.; Murakami, T. N.; Snaith, H. J. *Science* **2012**, *338*, 643–647.

[47] Seo, J.; Noh, J. H.; Seok, S. I. *Accounts of Chemical Research* **2016**, *49*, 562–572.

[48] Shi, H.; Liu, C.; Jiang, Q.; Xu, J. *Advanced Electronic Materials* **2015**, *1*, 1500017.

[49] Dong, Q.; Fang, Y.; Shao, Y.; Mulligan, P.; Qiu, J.; Cao, L.; Huang, J. *Science* **2015**, *347*, 967–970.

[50] Wang, W.; Tade, M. O.; Shao, Z. *Chemical Society Reviews* **2015**, *44*, 5371–5408.

[51] Ye, M.; Hong, X.; Zhang, F.; Liu, X. *Journal of Materials Chemistry A* **2016**, *4*, 6755–6771.

[52] Albero, J.; Asiri, A. M.; Garcia, H. *Journal of Materials Chemistry A* **2016**, *4*, 4353–4364.

[53] Kim, Y.; Cook, S.; Tuladhar, S. M.; Choulis, S. A.; Nelson, J.; Durrant, J. R.; Bradley, D. D. C.; Giles, M.; McCulloch, I.; Ha, C.-S.; Ree, M. *Nature Materials* **2006**, *5*, 197–203.

[54] Voelker, S. F.; Collavini, S.; Luis Delgado, J. *Chemsuschem* **2015**, *8*, 3012–3028.

[55] Herz, L. M. **2016**, *67*, 65–89.

[56] Manser, J. S.; Saidaminov, M. I.; Christians, J. A.; Bakr, O. M.; Kamat, P. V. *Accounts of Chemical Research* **2016**, *49*, 330–338.

[57] Egger, D. A.; Rappe, A. M.; Kronik, L. *Accounts of Chemical Research* **2016**, *49*,

573–581.

[58] Frost, J. M.; Walsh, A. *Accounts of Chemical Research* **2016**, *49*, 528–535.

[59] Gottesman, R.; Zaban, A. *Accounts of Chemical Research* **2016**, *49*, 320–329.

[60] Youn, H.; Park, H. J.; Guo, L. J. *Small* **2015**, *11*, 2228–2246.

[61] Cao, W.; Xue, J. *Energy & Environmental Science* **2014**, *7*, 2123–2144.

[62] Reale, A.; La Notte, L.; Salamandra, L.; Polino, G.; Susanna, G.; Brown, T. M.; Brunetti, F.; Di Carlo, A. *Energy Technology* **2015**, *3*, 385–406.

[63] Krebs, F. C. *Solar Energy Materials and Solar Cells* **2009**, *93*, 394–412.

[64] Angmo, D.; Krebs, F. C. *Journal of Applied Polymer Science* **2013**, *129*, 1–14.

[65] Shaheen, S. E.; Ginley, D. S.; Jabbour, G. E. *MRS Bulletin* **2005**, *30*, 10–19.

[66] Forrest, S. R. *Nature* **2004**, *428*, 911–918.

[67] Zimmermann, Y.-S.; Schaeffer, A.; Hugi, C.; Fent, K.; Corvini, P. F.-X.; Lenz, M. *Environment International* **2012**, *49*, 128–140.

[68] Espinosa, N.; García-Valverde, R.; Krebs, F. C. *Energy & Environmental Science* **2011**, *4*, 1547–1557.

[69] Espinosa, N.; Hösel, M.; Angmo, D.; Krebs, F. C. *Energy & Environmental Science* **2012**, *5*, 5117–5132.

[70] Lindholm, F. A.; Fossum, J. G.; Burgess, E. L. *IEEE Transactions on Electron Devices* **1979**, *26*, 165–171.

[71] Würfel, P. *Physics of Solar Cells: From Basic Principles to Advanced Concepts*, 2nd

ed.; Wiley, 2009.

[72] Mazzio, K. A.; Luscombe, C. K. *Chemical Society Reviews* **2014**, *44*, 78–90.

[73] Bernede, J. C. *Journal of the Chilean Chemical Society* **2008**, *53*, 1549–1564, WOS:000259295100001.

[74] Shockley, W.; Queisser, H. J. *Journal of Applied Physics* **1961**, *32*, 510–519.

[75] Mazzio, K. A.; Luscombe, C. K. *Chemical Society Reviews* **2015**, *44*, 78–90.

[76] Brabec, C. J.; Sariciftci, N. S.; Hummelen, J. C. *Advanced Functional Materials* **2001**, *11*, 15–26.

[77] Clarke, T. M.; Durrant, J. R. *Chemical Reviews* **2010**, *110*, 6736–6767.

[78] Blom, P. W. M.; Mihailetchi, V. D.; Koster, L. J. A.; Markov, D. E. *Advanced Materials* **2007**, *19*, 1551–1566.

[79] Li, G.; Zhu, R.; Yang, Y. *Nat Photon* **2012**, *6*, 153–161.

[80] Brabec, C. J.; Shaheen, S. E.; Winder, C.; Sariciftci, N. S.; Denk, P. *Applied Physics Letters* **2002**, *80*, 1288–1290.

[81] Yip, H.-L.; Jen, A. K.-Y. *Energy & Environmental Science* **2012**, *5*, 5994–6011.

[82] Litzov, I.; Brabec, C. J. *Materials* **2013**, *6*, 5796–5820.

[83] Coughlin, J. E.; Henson, Z. B.; Welch, G. C.; Bazan, G. C. *Accounts of Chemical Research* **2014**, *47*, 257–270.

[84] Shirota, Y.; Kageyama, H. *Chemical Reviews* **2007**, *107*, 953–1010.

[85] Guo, X.; Baumgarten, M.; Muellen, K. *Progress in Polymer Science* **2013**, *38*, 1832–

1908.

[86] Xu, T.; Yu, L. *Materials Today* **2014**, *17*, 11–15.

[87] Heeger, A.; MacDiarmid, A. G.; Shirakawa, H. *The Nobel Prize in Chemistry 2000: Conductive Polymer*; Royal Swedish Academy of Science, 2000.

[88] Bian, L.; Zhu, E.; Tang, J.; Tang, W.; Zhang, F. *Progress in Polymer Science* **2012**, *37*, 1292–1331.

[89] Tang, C. W. *Applied Physics Letters* **1986**, *48*, 183–185.

[90] Lu, L.; Zheng, T.; Wu, Q.; Schneider, A. M.; Zhao, D.; Yu, L. *Chemical Reviews* **2015**, *115*, 12666–12731.

[91] Pivrikas, A.; Sariciftci, N. S.; Juška, G.; Österbacka, R. *Progress in Photovoltaics: Research and Applications* **2007**, *15*, 677–696.

[92] Sariciftci, N. S.; Smilowitz, L.; Heeger, A. J.; Wudl, F. *Science* **1992**, *258*, 1474–1476.

[93] Kraabel, B.; Lee, C. H.; McBranch, D.; Moses, D.; Sariciftci, N. S.; Heeger, A. J. *Chemical Physics Letters* **1993**, *213*, 389–394.

[94] Halls, J. J. M.; Walsh, C. A.; Greenham, N. C.; Marseglia, E. A.; Friend, R. H.; Moratti, S. C.; Holmes, A. B. *Nature* **1995**, *376*, 498–500.

[95] Yu, G. *Science* **1995**, *270*, 1789–1791.

[96] Padinger, F.; Rittberger, R.; Sariciftci, N. *Advanced Functional Materials* **2003**, *13*, 85–88.

[97] Schilinsky, P.; Waldauf, C.; Brabec, C. J. *Applied Physics Letters* **2002**, *81*, 3885–3887.

[98] Ma, W.; Yang, C.; Gong, X.; Lee, K.; Heeger, A. J. *Advanced Functional Materials* **2005**, *15*, 1617–1622.

[99] Kim, J. Y.; Kim, S. H.; Lee, H.-H.; Lee, K.; Ma, W.; Gong, X.; Heeger, A. J. *Advanced Materials* **2006**, *18*, 572–576.

[100] Lou, S. J.; Szarko, J. M.; Xu, T.; Yu, L.; Marks, T. J.; Chen, L. X. *Journal of the American Chemical Society* **2011**, *133*, 20661–20663.

[101] Lee, J. K.; Ma, W. L.; Brabec, C. J.; Yuen, J.; Moon, J. S.; Kim, J. Y.; Lee, K.; Bazan, G. C.; Heeger, A. J. *Journal of the American Chemical Society* **2008**, *130*, 3619–3623.

[102] Verploegen, E.; Mondal, R.; Bettinger, C. J.; Sok, S.; Toney, M. F.; Bao, Z. *Advanced Functional Materials* **2010**, *20*, 3519–3529.

[103] Zhao, G.; He, Y.; Li, Y. *Advanced Materials* **2010**, *22*, 4355–4358.

[104] Gao, J.; Dou, L.; Chen, W.; Chen, C.-C.; Guo, X.; You, J.; Bob, B.; Chang, W.-H.; Strzalka, J.; Wang, C.; Li, G.; Yang, Y. *Advanced Energy Materials* **2014**, *4*, 1300739.

[105] Intemann, J. J.; Yao, K.; Li, Y.-X.; Yip, H.-L.; Xu, Y.-X.; Liang, P.-W.; Chueh, C.-C.; Ding, F.-Z.; Yang, X.; Li, X.; Chen, Y.; Jen, A. K.-Y. *Advanced Functional Materials* **2014**, *24*, 1465–1473.

[106] Fang, L.; Zhou, Y.; Yao, Y.-X.; Diao, Y.; Lee, W.-Y.; Appleton, A. L.; Allen, R.; Reinspach, J.; Mannsfeld, S. C. B.; Bao, Z. *Chemistry of Materials* **2013**, *25*, 4874–4880.

[107] Cabanetos, C.; El Labban, A.; Bartelt, J. A.; Douglas, J. D.; Mateker, W. R.; Fréchet, J. M. J.; McGehee, M. D.; Beaujuge, P. M. *Journal of the American Chemical Society* **2013**, *135*, 4656–4659.

[108] Price, S. C.; Stuart, A. C.; Yang, L.; Zhou, H.; You, W. *Journal of the American Chemical Society* **2011**, *133*, 4625–4631.

[109] Liang, Y.; Xu, Z.; Xia, J.; Tsai, S.-T.; Wu, Y.; Li, G.; Ray, C.; Yu, L. *Advanced Materials* **2010**, *22*, E135–E138.

[110] Jung, J. W.; Jo, J. W.; Jung, E. H.; Jo, W. H. *Organic Electronics* **2016**, *31*, 149–170.

[111] Park, S. H.; Roy, A.; Beaupré, S.; Cho, S.; Coates, N.; Moon, J. S.; Moses, D.; Leclerc, M.; Lee, K.; Heeger, A. J. *Nature Photonics* **2009**, *3*, 297–302.

[112] Zou, Y.; Najari, A.; Berrouard, P.; Beaupré, S.; Réda Aïch, B.; Tao, Y.; Leclerc, M. *Journal of the American Chemical Society* **2010**, *132*, 5330–5331.

[113] He, Z.; Zhong, C.; Su, S.; Xu, M.; Wu, H.; Cao, Y. *Nature Photonics* **2012**, *6*, 591–595.

[114] Mihailetchi, V. D.; Koster, L. J. A.; Blom, P. W. M.; Melzer, C.; de B., Boer; van J. K. J., Duren; Janssen, R. a. J. *Advanced Functional Materials* **2005**, *15*, 795–801.

[115] Mihailetchi, V. D.; Xie, H. X.; de B., Boer; Koster, L. J. A.; Blom, P. W. M. *Advanced Functional Materials* **2006**, *16*, 699–708.

[116] Li, W.; Hendriks, K. H.; Wienk, M. M.; Janssen, R. A. J. *Accounts of Chemical Research* **2016**, *49*, 78–85.

[117] Li, Y.; Sonar, P.; Murphy, L.; Hong, W. *Energy & Environmental Science* **2013**, *6*,

1684–1710.

[118] Bronstein, H. et al. *Journal of the American Chemical Society* **2011**, *133*, 3272–3275.

[119] Boudreault, P.-L. T.; Najari, A.; Leclerc, M. *Chemistry of Materials* **2011**, *23*, 456–469.

[120] Aïch, B. R.; Lu, J.; Beaupré, S.; Leclerc, M.; Tao, Y. *Organic Electronics* **2012**, *13*, 1736–1741.

[121] Roncali, J. *Accounts of Chemical Research* **2009**, *42*, 1719–1730.

[122] Lin, Y.; Li, Y.; Zhan, X. *Chemical Society Reviews* **2012**, *41*, 4245–4272.

[123] Lai, L. F.; Love, J. A.; Sharenko, A.; Coughlin, J. E.; Gupta, V.; Tretiak, S.; Nguyen, T.-Q.; Wong, W.-Y.; Bazan, G. C. *Journal of the American Chemical Society* **2014**, *136*, 5591–5594.

[124] Roncali, J.; Leriche, P.; Blanchard, P. *Advanced Materials* **2014**, *26*, 3821–3838.

[125] Peumans, P.; Yakimov, A.; Forrest, S. R. *Journal of Applied Physics* **2003**, *93*, 3693–3723.

[126] Walzer, K.; Maennig, B.; Pfeiffer, M.; Leo, K. *Chemical Reviews* **2007**, *107*, 1233–1271.

[127] de Bettignies, R.; Nicolas, Y.; Blanchard, P.; Levillain, E.; Nunzi, J.-M.; Roncali, J. *Advanced Materials* **2003**, *15*, 1939–1943.

[128] Uhrich, C.; Schueppel, R.; Petrich, A.; Pfeiffer, M.; Leo, K.; Brier, E.; Kilickiran, P.; Baeuerle, P. *Advanced Functional Materials* **2007**, *17*, 2991–2999.

[129] Peumans, P.; Forrest, S. R. *Applied Physics Letters* **2001**, *79*, 126–128.

[130] Peumans, P.; Forrest, S. R. *Applied Physics Letters* **2002**, *80*, 338–338.

[131] Fukuzumi, S.; Kojima, T. *Journal of Materials Chemistry* **2008**, *18*, 1427–1439.

[132] Hains, A. W.; Liang, Z.; Woodhouse, M. A.; Gregg, B. A. *Chemical Reviews* **2010**, *110*, 6689–6735.

[133] Walker, B.; Kim, C.; Nguyen, T.-Q. *Chemistry of Materials* **2011**, *23*, 470–482.

[134] Imahori, H.; Fukuzumi, S. *Advanced Functional Materials* **2004**, *14*, 525–536.

[135] van der Poll, T. S.; Love, J. A.; Nguyen, T.-Q.; Bazan, G. C. *Advanced Materials* **2012**, *24*, 3646–3649.

[136] Eisenmenger, N. D.; Su, G. M.; Welch, G. C.; Takacs, C. J.; Bazan, G. C.; Kramer, E. J.; Chabinyc, M. L. *Chemistry of Materials* **2013**, *25*, 1688–1698.

[137] Chueh, C.-C.; Li, C.-Z.; Jen, A. K.-Y. *Energy & Environmental Science* **2015**, *8*, 1160–1189.

[138] Yip, H.-L.; Jen, A. K.-Y. *Energy & Environmental Science* **2012**, *5*, 5994–6011.

[139] Braun, S.; Salaneck, W. R.; Fahlman, M. *Advanced Materials* **2009**, *21*, 1450–1472.

[140] Hu, Z.; Zhong, Z.; Chen, Y.; Sun, C.; Huang, F.; Peng, J.; Wang, J.; Cao, Y. *Advanced Functional Materials* **2016**, *26*, 129–136.

[141] Wang, K.; Liu, C.; Meng, T.; Yi, C.; Gong, X. *Chemical Society Reviews* **2016**, *45*, 2937–2975.

[142] Sun, Y.; Seo, J. H.; Takacs, C. J.; Seifter, J.; Heeger, A. J. *Advanced Materials* **2011**,

23, 1679–1683.

[143] White, M. S.; Olson, D. C.; Shaheen, S. E.; Kopidakis, N.; Ginley, D. S. *Applied Physics Letters* **2006**, *89*, 143517.

[144] Jagadamma, L. K.; Abdelsamie, M.; Labban, A. E.; Aresu, E.; Ndjawa, G. O. N.; Anjum, D. H.; Cha, D.; Beaujuge, P. M.; Amassian, A. *Journal of Materials Chemistry A* **2014**, *2*, 13321–13331.

[145] Noh, Y.-J.; Na, S.-I.; Kim, S.-S. *Solar Energy Materials and Solar Cells* **2013**, *117*, 139–144.

[146] You, J.; Chen, C.-C.; Dou, L.; Murase, S.; Duan, H.-S.; Hawks, S. A.; Xu, T.; Son, H. J.; Yu, L.; Li, G.; Yang, Y. *Advanced Materials* **2012**, *24*, 5267–5272.

[147] Ibrahem, M. A.; Wei, H.-Y.; Tsai, M.-H.; Ho, K.-C.; Shyue, J.-J.; Chu, C. W. *Solar Energy Materials and Solar Cells* **2013**, *108*, 156–163.

[148] Ihn, S.-G.; Lim, Y.; Yun, S.; Park, I.; Park, J. H.; Chung, Y.; Bulliard, X.; Chang, J.; Choi, H.; Park, J. H.; Choi, Y. S.; Park, G.-S.; Chang, H. *Journal of Materials Chemistry A* **2014**, *2*, 2033–2039.

[149] Thambidurai, M.; Kim, J. Y.; Ko, Y.; Song, H.-j.; Shin, H.; Song, J.; Lee, Y.; Muthukumarasamy, N.; Velauthapillai, D.; Lee, C. *Nanoscale* **2014**, *6*, 8585–8589.

[150] Chen, F.; Chen, Q.; Mao, L.; Wang, Y.; Huang, X.; Lu, W.; Wang, B.; Chen, L. *Nanotechnology* **2013**, *24*, 484011.

[151] Park, B.; Shin, J. C.; Cho, C. Y. *Solar Energy Materials and Solar Cells* **2013**, *108*, 1–8.

[152] Jia, Y.; Yang, L.; Qin, W.; Yin, S.; Zhang, F.; Wei, J. *Renewable Energy* **2013**, *50*, 565–569.

[153] Xiao, T.; Cui, W.; Cai, M.; Leung, W.; Anderegg, J. W.; Shinar, J.; Shinar, R. *Organic Electronics* **2013**, *14*, 267–272.

[154] Choy, W. C. H.; Zhang, D. *Small* **2016**, *12*, 416–431.

[155] Zhou, Y. et al. *Science* **2012**, *336*, 327–332.

[156] Wang, H.; Zhang, W.; Xu, C.; Bi, X.; Chen, B.; Yang, S. *ACS Applied Materials & Interfaces* **2013**, *5*, 26–34.

[157] Kang, H.; Hong, S.; Lee, J.; Lee, K. *Advanced Materials* **2012**, *24*, 3005–3009.

[158] Tang, Z.; Andersson, L. M.; George, Z.; Vandewal, K.; Tvingstedt, K.; Heriksson, P.; Kroon, R.; Andersson, M. R.; Inganäs, O. *Advanced Materials* **2012**, *24*, 554–558.

[159] Lv, M.; Li, S.; Jasieniak, J. J.; Hou, J.; Zhu, J.; Zhan'ao Tan, Z.; Watkins, S. E.; Li, Y.; Chen, X. *Advanced Materials* **2013**, *25*, 6889–6894.

[160] Xiao, H.; Miao, J.; Cao, J.; Yang, W.; Wu, H.; Cao, Y. *Organic Electronics* **2014**, *15*, 758–774.

[161] Xu, W.; Zhang, X.; Hu, Q.; Zhao, L.; Teng, X.; Lai, W.-Y.; Xia, R.; Nelson, J.; Huang, W.; Bradley, D. D. C. *Organic Electronics* **2014**, *15*, 1244–1253.

[162] Shi, T.; Zhu, X.; Yang, D.; Xie, Y.; Zhang, J.; Tu, G. *Applied Physics Letters* **2012**, *101*, 161602.

[163] Duan, C.; Zhong, C.; Liu, C.; Huang, F.; Cao, Y. *Chemistry of Materials* **2012**, *24*, 1682–1689.

[164] Hong, D.; Lv, M.; Lei, M.; Chen, Y.; Lu, P.; Wang, Y.; Zhu, J.; Wang, H.; Gao, M.; Watkins, S. E.; Chen, X. *ACS Applied Materials & Interfaces* **2013**, *5*, 10995–11003.

[165] Jiao, W.; Ma, D.; Lv, M.; Chen, W.; Wang, H.; Zhu, J.; Lei, M.; Chen, X. *Journal of Materials Chemistry A* **2014**, *2*, 14720–14728.

[166] Yi, C.; Yue, K.; Zhang, W.-B.; Lu, X.; Hou, J.; Li, Y.; Huang, L.; Newkome, G. R.; Cheng, S. Z. D.; Gong, X. *ACS Applied Materials & Interfaces* **2014**, *6*, 14189–14195.

[167] Hau, S. K.; Cheng, Y.-J.; Yip, H.-L.; Zhang, Y.; Ma, H.; Jen, A. K.-Y. *ACS Applied Materials & Interfaces* **2010**, *2*, 1892–1902.

[168] Hains, A. W.; Liu, J.; Martinson, A. B. F.; Irwin, M. D.; Marks, T. J. *Advanced Functional Materials* **2010**, *20*, 595–606.

[169] Ma, W.; Iyer, P. K.; Gong, X.; Liu, B.; Moses, D.; Bazan, G. C.; Heeger, A. J. *Advanced Materials* **2005**, *17*, 274–277.

[170] Mauger, S. A.; Chang, L.; Rochester, C. W.; Moulé, A. J. *Organic Electronics* **2012**, *13*, 2747–2756.

[171] Park, S. H.; Roy, A.; Beaupré, S.; Cho, S.; Coates, N.; Moon, J. S.; Moses, D.; Leclerc, M.; Lee, K.; Heeger, A. J. *Nature Photonics* **2009**, *3*, 297–302.

[172] Sun, K.; Zhang, S.; Li, P.; Xia, Y.; Zhang, X.; Du, D.; Isikgor, F. H.; Ouyang, J. *Journal of Materials Science: Materials in Electronics* **2015**, *26*, 4438–4462.

[173] Wong, K. W.; Yip, H. L.; Luo, Y.; Wong, K. Y.; Lau, W. M.; Low, K. H.; Chow, H. F.; Gao, Z. Q.; Yeung, W. L.; Chang, C. C. *Applied Physics Letters* **2002**, *80*, 2788–2790.

[174] Pingree, L. S. C.; MacLeod, B. A.; Ginger, D. S. *The Journal of Physical Chemistry C* **2008**, *112*, 7922–7927.

[175] Hau, S. K.; Yip, H.-L.; Zou, J.; Jen, A. K. Y. *Organic Electronics* **2009**, *10*, 1401–1407.

[176] Bulliard, X.; Ihn, S.-G.; Yun, S.; Kim, Y.; Choi, D.; Choi, J.-Y.; Kim, M.; Sim, M.; Park, J.-H.; Choi, W.; Cho, K. *Advanced Functional Materials* **2010**, *20*, 4381–4387.

[177] Zeng, H.; Zhu, X.; Liang, Y.; Guo, X. *Polymers* **2015**, *7*, 333–372.

[178] Zhao, K.; Ngongang Ndjawa, G. O.; Jagadamma, L. K.; Labban, A. E.; Hu, H.; Wang, Q.; Li, R.; Abdelsamie, M.; Beaujuge, P. M.; Amassian, A. *Nano Energy* **2015**, *16*, 458–469.

[179] Li, W.; Worfolk, B. J.; Li, P.; Hauger, T. C.; Harris, K. D.; Buriak, J. M. *Journal of Materials Chemistry* **2012**, *22*, 11354–11363.

[180] Sun, J.; Zhu, Y.; Xu, X.; Lan, L.; Zhang, L.; Cai, P.; Chen, J.; Peng, J.; Cao, Y. *The Journal of Physical Chemistry C* **2012**, *116*, 14188–14198.

[181] Shim, J. W.; Fuentes-Hernandez, C.; Dindar, A.; Zhou, Y.; Khan, T. M.; Kippelen, B. *Organic Electronics* **2013**, *14*, 2802–2808.

[182] Steirer, K. X.; Ndione, P. F.; Widjonarko, N. E.; Lloyd, M. T.; Meyer, J.; Ratcliff, E. L.; Kahn, A.; Armstrong, N. R.; Curtis, C. J.; Ginley, D. S.; Berry, J. J.; Olson, D. C. *Advanced Energy Materials* **2011**, *1*, 813–820.

[183] Hau, S. K.; Yip, H.-L.; Zou, J.; Jen, A. K. Y. *Organic Electronics* **2009**, *10*, 1401–1407.

[184] Chen, C.-P.; Chen, Y.-D.; Chuang, S.-C. *Advanced Materials* **2011**, *23*, 3859–3863.

[185] Lu, L.; Xu, T.; Jung, I. H.; Yu, L. *The Journal of Physical Chemistry C* **2014**, *118*, 22834–22839.

[186] Tu, X.; Wang, F.; Li, C.; Tan, Z.; Li, Y. *The Journal of Physical Chemistry C* **2014**, *118*, 9309–9317.

[187] Li, S.-S.; Tu, K.-H.; Lin, C.-C.; Chen, C.-W.; Chhowalla, M. *ACS Nano* **2010**, *4*, 3169–3174.

[188] Murray, I. P.; Lou, S. J.; Cote, L. J.; Loser, S.; Kadleck, C. J.; Xu, T.; Szarko, J. M.; Rolczynski, B. S.; Johns, J. E.; Huang, J.; Yu, L.; Chen, L. X.; Marks, T. J.; Hersam, M. C. *The Journal of Physical Chemistry Letters* **2011**, *2*, 3006–3012.

[189] Stratakis, E.; Savva, K.; Konios, D.; Petridis, C.; Kymakis, E. *Nanoscale* **2014**, *6*, 6925–6931.

[190] Günes, S.; Neugebauer, H.; Sariciftci, N. S. *Chemical Reviews* **2007**, *107*, 1324–1338.

[191] Yu, M.; Long, Y.-Z.; Sun, B.; Fan, Z. *Nanoscale* **2012**, *4*, 2783–2796.

[192] Kang, M.-G.; Xu, T.; Park, H. J.; Luo, X.; Guo, L. J. *Advanced Materials* **2010**, *22*, 4378–4383.

[193] Kang, S.-B.; Noh, Y.-J.; Na, S.-I.; Kim, H.-K. *Solar Energy Materials and Solar Cells* **2014**, *122*, 152–157.

[194] Kim, A.; Won, Y.; Woo, K.; Kim, C.-H.; Moon, J. *ACS Nano* **2013**, *7*, 1081–1091.

[195] Cha, M. J.; Kim, S. M.; Kang, S. J.; Seo, J. H.; Walker, B. *RSC Advances* **2015**, *5*,

65646–65650.

[196] Choi, Y.-Y.; Kang, S. J.; Kim, H.-K.; Choi, W. M.; Na, S.-I. *Solar Energy Materials and Solar Cells* **2012**, *96*, 281–285.

[197] Wan, X.; Long, G.; Huang, L.; Chen, Y. *Advanced Materials* **2011**, *23*, 5342–5358.

[198] Park, H.; Brown, P. R.; Bulović, V.; Kong, J. *Nano Letters* **2012**, *12*, 133–140.

[199] Rowell, M. W.; Topinka, M. A.; McGehee, M. D.; Prall, H.-J.; Dennler, G.; Sariciftci, N. S.; Hu, L.; Gruner, G. *Applied Physics Letters* **2006**, *88*, 233506.

[200] Tenent, R. C.; Barnes, T. M.; Bergeson, J. D.; Ferguson, A. J.; To, B.; Gedvilas, L. M.; Heben, M. J.; Blackburn, J. L. *Advanced Materials* **2009**, *21*, 3210–3216.

[201] Kim, Y. H.; Sachse, C.; Machala, M. L.; May, C.; Müller-Meskamp, L.; Leo, K. *Advanced Functional Materials* **2011**, *21*, 1076–1081.

[202] Na, S.-I.; Kim, S.-S.; Jo, J.; Kim, D.-Y. *Advanced Materials* **2008**, *20*, 4061–4067.

[203] Hauger, T. C.; Al-Rafia, S. M. I.; Buriak, J. M. *ACS Applied Materials & Interfaces* **2013**, *5*, 12663–12671.

[204] Gonzalez-Valls, I.; Lira-Cantu, M. *Energy & Environmental Science* **2008**, *2*, 19–34.

[205] Li, L.; Zhai, T.; Bando, Y.; Golberg, D. *Nano Energy* **2012**, *1*, 91–106.

[206] Yu, P.; Chang, C.-H.; Su, M.-S.; Hsu, M.-H.; Wei, K.-H. *Applied Physics Letters* **2010**, *96*, 153307.

[207] Olson, D. C.; Shaheen, S. E.; Collins, R. T.; Ginley, D. S. *The Journal of Physical Chemistry C* **2007**, *111*, 16670–16678.

[208] Hsu, M.-H.; Yu, P.; Huang, J.-H.; Chang, C.-H.; Wu, C.-W.; Cheng, Y.-C.; Chu, C.-W. *Applied Physics Letters* **2011**, *98*, 073308.

[209] Rider, D. A.; Tucker, R. T.; Worfolk, B. J.; Krause, K. M.; Lalany, A.; Brett, M. J.; Buriak, J. M.; Harris, K. D. *Nanotechnology* **2011**, *22*, 085706.

[210] Yuan, Z.; Fu, M.; Huang, W. *Synthetic Metals* **2013**, *185*, 133–136.

[211] Hsu, M.-H.; Huang, J.-H.; Chang, C.-H.; Cheng, Y.-C.; Chu, C.-W.; Yu, P. Balanced carrier transport in organic solar cells using implanted indium-tin-oxide nano-columns. 2011 37th IEEE Photovoltaic Specialists Conference (PVSC). 2011; pp 001160–001164.

[212] Iza, D. C.; Muñoz-Rojas, D.; Jia, Q.; Swartzentruber, B.; MacManus-Driscoll, J. L. *Nanoscale Research Letters* **2012**, *7*, 655.

[213] Tu, Y.-C.; Lin, J.-F.; Lin, W.-C.; Liu, C.-P.; Shyue, J.-J.; Su, W.-F. *CrystEngComm* **2012**, *14*, 4772–4776.

[214] Yoon, S. M.; Lou, S. J.; Loser, S.; Smith, J.; Chen, L. X.; Facchetti, A.; Marks, T. *Nano Letters* **2012**, *12*, 6315–6321.

[215] Weickert, J.; Dunbar, R. B.; Hesse, H. C.; Wiedemann, W.; Schmidt-Mende, L. *Advanced Materials* **2011**, *23*, 1810–1828.

[216] Bai, H.; Wang, Y.; Cheng, P.; Li, Y.; Zhu, D.; Zhan, X. *ACS Applied Materials & Interfaces* **2014**, *6*, 8426–8433.

[217] Chen, Y.; Wan, X.; Long, G. *Accounts of Chemical Research* **2013**, *46*, 2645–2655.

[218] Lin, Y.; Ma, L.; Li, Y.; Liu, Y.; Zhu, D.; Zhan, X. *Advanced Energy Materials* **2014**,

4, 1300626.

[219] Lu, H.-I.; Lu, C.-W.; Lee, Y.-C.; Lin, H.-W.; Lin, L.-Y.; Lin, F.; Chang, J.-H.; Wu, C.-I.; Wong, K.-T. *Chemistry of Materials* **2014**, *26*, 4361–4367.

[220] Mishra, A.; Bäuerle, P. *Angewandte Chemie International Edition* **2012**, *51*, 2020–2067.

[221] Kyaw, A. K. K.; Wang, D. H.; Gupta, V.; Zhang, J.; Chand, S.; Bazan, G. C.; Heeger, A. J. *Advanced Materials* **2013**, *25*, 2397–2402.

[222] Blouin, N.; Michaud, A.; Leclerc, M. *Advanced Materials* **2007**, *19*, 2295–2300.

[223] Chen, J.; Cao, Y. *Accounts of Chemical Research* **2009**, *42*, 1709–1718.

[224] Scharber, M. C.; Koppe, M.; Gao, J.; Cordella, F.; Loi, M. A.; Denk, P.; Morana, M.; Egelhaaf, H.-J.; Forberich, K.; Dennler, G.; Gaudiana, R.; Waller, D.; Zhu, Z.; Shi, X.; Brabec, C. J. *Advanced Materials* **2010**, *22*, 367–370.

[225] Zhou, H.; Yang, L.; Stuart, A. C.; Price, S. C.; Liu, S.; You, W. *Angewandte Chemie International Edition* **2011**, *50*, 2995–2998.

[226] He, X.; Baumgartner, T. *RSC Advances* **2013**, *3*, 11334–11350.

[227] Gibson, G. L.; McCormick, T. M.; Seferos, D. S. *Journal of the American Chemical Society* **2012**, *134*, 539–547.

[228] He, G.; Kang, L.; Torres Delgado, W.; Shynkaruk, O.; Ferguson, M. J.; McDonald, R.; Rivard, E. *Journal of the American Chemical Society* **2013**, *135*, 5360–5363.

[229] Park, Y. S.; Wu, Q.; Nam, C.-Y.; Grubbs, R. B. *Angewandte Chemie International*

Edition **2014**, *53*, 10691–10695.

[230] Lee, J.; Han, A.-R.; Kim, J.; Kim, Y.; Oh, J. H.; Yang, C. *Journal of the American Chemical Society* **2012**, *134*, 20713–20721.

[231] Dou, L.; Chang, W.-H.; Gao, J.; Chen, C.-C.; You, J.; Yang, Y. *Advanced Materials* **2013**, *25*, 825–831.

[232] Warnan, J.; El Labban, A.; Cabanetos, C.; Hoke, E. T.; Shukla, P. K.; Risko, C.; Brédas, J.-L.; McGehee, M. D.; Beaujuge, P. M. *Chemistry of Materials* **2014**, *26*, 2299–2306.

[233] Kronemeijer, A. J.; Gili, E.; Shahid, M.; Rivnay, J.; Salleo, A.; Heeney, M.; Sirringhaus, H. *Advanced Materials* **2012**, *24*, 1558–1565.

[234] Carrera, E. I.; Seferos, D. S. *Macromolecules* **2015**, *48*, 297–308.

[235] Gibson, G. L.; McCormick, T. M.; Seferos, D. S. *The Journal of Physical Chemistry C* **2013**, *117*, 16606–16615.

[236] Das, S.; Pati, P. B.; Zade, S. S. *Macromolecules* **2012**, *45*, 5410–5417.

[237] Hou, J.; Park, M.-H.; Zhang, S.; Yao, Y.; Chen, L.-M.; Li, J.-H.; Yang, Y. *Macromolecules* **2008**, *41*, 6012–6018.

[238] Hou, J.; Chen, T. L.; Zhang, S.; , H.-Y. C.; Yang, Y. *The Journal of Physical Chemistry C* **2009**, *113*, 1601–1605.

[239] Yang, R.; Tian, R.; Hou, Q.; Yang, W.; Cao, Y. *Macromolecules* **2003**, *36*, 7453–7460.

[240] Pati, P. B.; Zade, S. S. *Crystal Growth & Design* **2014**, *14*, 1695–1700.

[241] Worfolk, B. J.; Hauger, T. C.; Harris, K. D.; Rider, D. A.; Fordyce, J. A. M.; Beaupré, S.; Leclerc, M.; Buriak, J. M. *Advanced Energy Materials* **2012**, *2*, 361–368.

[242] Piliego, C.; Holcombe, T. W.; Douglas, J. D.; Woo, C. H.; Beaujuge, P. M.; Fréchet, J. M. J. *Journal of the American Chemical Society* **2010**, *132*, 7595–7597.

[243] Hollinger, J.; Gao, D.; Seferos, D. S. *Israel Journal of Chemistry* **2014**, *54*, 440–453.

[244] Heeney, M.; Zhang, W.; Crouch, D. J.; Chabinyc, M. L.; Gordeyev, S.; Hamilton, R.; Higgins, S. J.; McCulloch, I.; Skabara, P. J.; Sparrowe, D.; Tierney, S. *Chemical Communications* **2007**, 5061–5063.

[245] Hollinger, J.; Jahnke, A. A.; Coombs, N.; Seferos, D. S. *Journal of the American Chemical Society* **2010**, *132*, 8546–8547.

[246] Würthner, F.; Kaiser, T. E.; Saha-Möller, C. R. *Angewandte Chemie International Edition* **2011**, *50*, 3376–3410.

[247] Spano, F. C.; Silva, C. *Annual Review of Physical Chemistry* **2014**, *65*, 477–500.

[248] Frisch, M. J.; Trucks, G. W.; Schlegel, H. B.; Scuseria, G. E.; Robb, M. A.; Cheeseman, J. R.; Scalmani, G.; Barone, V.; Mennucci, B.; Petersson, G. A.; Nakatsuji, H.; Caricato, M.; Li, X.; Hratchian, H. P.; Izmaylov, A. F.; Bloino, J.; Zheng, G.; Sonnenberg, J. L.; Hada, M.; Ehara, M.; Toyota, K.; Fukuda, R.; Hasegawa, J.; Ishida, M.; Nakajima, T.; Honda, Y.; Kitao, O.; Nakai, H.; Vreven, T.; Montgomery, J. A., Jr.; Peralta, J. E.; Ogliaro, F.; Bearpark, M.; Heyd, J. J.; Brothers, E.; Kudin, K. N.; Staroverov, V. N.; Kobayashi, R.; Normand, J.; Raghavachari, K.; Rendell, A.; Burant, J. C.; Iyengar, S. S.; Tomasi, J.; Cossi, M.; Rega, N.; Millam, J. M.; Klene, M.; Knox, J. E.; Cross, J. B.; Bakken, V.; Adamo, C.; Jaramillo, J.;

Gomperts, R.; Stratmann, R. E.; Yazyev, O.; Austin, A. J.; Cammi, R.; Pomelli, C.; Ochterski, J. W.; Martin, R. L.; Morokuma, K.; Zakrzewski, V. G.; Voth, G. A.; Salvador, P.; Dannenberg, J. J.; Dapprich, S.; Daniels, A. D.; Farkas, Ö.; Foresman, J. B.; Ortiz, J. V.; Cioslowski, J.; Fox, D. J. Gaussian 09, revision A.02; Gaussian, Inc.: Wallingford, CT, 2009.

[249] Agostinelli, T.; Lilliu, S.; Labram, J. G.; Campoy-Quiles, M.; Hampton, M.; Pires, E.; Rawle, J.; Bikondoa, O.; Bradley, D. D. C.; Anthopoulos, T. D.; Nelson, J.; Macdonald, J. E. *Advanced Functional Materials* **2011**, *21*, 1701–1708.

[250] Huang, W. Y.; Huang, P. T.; Han, Y. K.; Lee, C. C.; Hsieh, T. L.; Chang, M. Y. *Macromolecules* **2008**, *41*, 7485–7489.

[251] Chabinyc, M. L.; Toney, M. F.; Kline, R. J.; McCulloch, I.; Heeney, M. *Journal of the American Chemical Society* **2007**, *129*, 3226–3237.

[252] McCulloch, I.; Heeney, M.; Bailey, C.; Genevicius, K.; MacDonald, I.; Shkunov, M.; Sparrowe, D.; Tierney, S.; Wagner, R.; Zhang, W.; Chabinyc, M. L.; Kline, R. J.; McGehee, M. D.; Toney, M. F. *Nature Materials* **2006**, *5*, 328–333.

[253] Kline, R. J.; DeLongchamp, D. M.; Fischer, D. A.; Lin, E. K.; Richter, L. J.; Chabinyc, M. L.; Toney, M. F.; Heeney, M.; McCulloch, I. *Macromolecules* **2007**, *40*, 7960–7965.

[254] Dhar, P.; Khlyabich, P. P.; Burkhart, B.; Roberts, S. T.; Malyk, S.; Thompson, B. C.; Benderskii, A. V. *The Journal of Physical Chemistry C* **2013**, *117*, 15213–15220.

[255] Lu, L.; Zheng, T.; Wu, Q.; Schneider, A. M.; Zhao, D.; Yu, L. *Chemical Reviews* **2015**, *115*, 12666–12731.

[256] Deibel, C.; Dyakonov, V. *Reports on Progress in Physics* **2010**, *73*, 096401.

[257] Cao, W.; Xue, J. *Energy & Environmental Science* **2014**, *7*, 2123–2144.

[258] Brabec, C. J.; Gowrisanker, S.; Halls, J. J. M.; Laird, D.; Jia, S.; Williams, S. P. *Advanced Materials* **2010**, *22*, 3839–3856.

[259] Huang, Y.; Kramer, E. J.; Heeger, A. J.; Bazan, G. C. *Chemical Reviews* **2014**, *114*, 7006–7043.

[260] Li, G.; Zhu, R.; Yang, Y. *Nature Photonics* **2012**, *6*, 153–161.

[261] Helgesen, M.; Carlé, J. E.; dos Reis Benatto, G. A.; Søndergaard, R. R.; Jørgensen, M.; Bundgaard, E.; Krebs, F. C. *Advanced Energy Materials* **2015**, *5*, 1401996.

[262] Dam, H. F.; Andersen, T. R.; Pedersen, E. B. L.; Thydén, K. T. S.; Helgesen, M.; Carlé, J. E.; Jørgensen, P. S.; Reinhardt, J.; Søndergaard, R. R.; Jørgensen, M.; Bundgaard, E.; Krebs, F. C.; Andreasen, J. W. *Advanced Energy Materials* **2015**, *5*, 1400736.

[263] Galagan, Y.; Coenen, E. W. C.; Zimmermann, B.; Slooff, L. H.; Verhees, W. J. H.; Veenstra, S. C.; Kroon, J. M.; Jørgensen, M.; Krebs, F. C.; Andriessen, R. *Advanced Energy Materials* **2014**, *4*, 1300498.

[264] Krebs, F. C.; Espinosa, N.; Hösel, M.; Søndergaard, R. R.; Jørgensen, M. *Advanced Materials* **2014**, *26*, 29–39.

[265] Scharber, M. C.; Mühlbacher, D.; Koppe, M.; Denk, P.; Waldauf, C.; Heeger, A. J.; Brabec, C. J. *Advanced Materials* **2006**, *18*, 789–794.

[266] Beaupré, S.; Leclerc, M. *Journal of Materials Chemistry A* **2013**, *1*, 11097–11105.

[267] Beaujuge, P. M.; Fréchet, J. M. J. *Journal of the American Chemical Society* **2011**, *133*, 20009–20029.

[268] Chen, L.; Xie, C.; Chen, Y. *Organic Electronics* **2013**, *14*, 1551–1561.

[269] Peet, J.; Heeger, A. J.; Bazan, G. C. *Accounts of Chemical Research* **2009**, *42*, 1700–1708.

[270] Liu, Y.; Zhao, J.; Li, Z.; Mu, C.; Ma, W.; Hu, H.; Jiang, K.; Lin, H.; Ade, H.; Yan, H. *Nature Communications* **2014**, *5*, 5293.

[271] Sun, Y.; Seifter, J.; Wang, M.; Perez, L. A.; Luo, C.; Bazan, G. C.; Huang, F.; Cao, Y.; Heeger, A. J. *Advanced Energy Materials* **2014**, *4*, 1301601.

[272] Aytun, T.; Barreda, L.; Ruiz-Carretero, A.; Lehrman, J. A.; Stupp, S. I. *Chemistry of Materials* **2015**, *27*, 1201–1209.

[273] Livi, F.; Zawacka, N. K.; Angmo, D.; Jørgensen, M.; Krebs, F. C.; Bundgaard, E. *Macromolecules* **2015**, *48*, 3481–3492.

[274] Hu, Z.; Zhang, K.; Huang, F.; Cao, Y. *Chemical Communications* **2015**, *51*, 5572–5585.

[275] Steim, R.; Kogler, F. R.; Brabec, C. J. *Journal of Materials Chemistry* **2010**, *20*, 2499–2512.

[276] Crispin, X.; Jakobsson, F. L. E.; Crispin, A.; Grim, P. C. M.; Andersson, P.; Volodin, A.; van Haesendonck, C.; Van der Auweraer, M.; Salaneck, W. R.; Berggren, M. *Chemistry of Materials* **2006**, *18*, 4354–4360.

[277] Ouyang, J.; Chu, C.-W.; Chen, F.-C.; Xu, Q.; Yang, Y. *Advanced Functional Materials* **2005**, *15*, 203–208.

[278] Kim, Y.-H.; Lee, S.-H.; Noh, J.; Han, S.-H. *Thin Solid Films* **2006**, *510*, 305–310.

[279] Voroshazi, E.; Verreet, B.; Buri, A.; Müller, R.; Di Nuzzo, D.; Heremans, P. *Organic Electronics* **2011**, *12*, 736–744.

[280] Norrman, K.; Larsen, N. B.; Krebs, F. C. *Solar Energy Materials and Solar Cells* **2006**, *90*, 2793–2814.

[281] Norrman, K.; Gevorgyan, S. A.; Krebs, F. C. *ACS Applied Materials & Interfaces* **2009**, *1*, 102–112.

[282] Kawano, K.; Pacios, R.; Poplavskyy, D.; Nelson, J.; Bradley, D. D. C.; Durrant, J. R. *Solar Energy Materials and Solar Cells* **2006**, *90*, 3520–3530.

[283] Crispin, X.; Marciniak, S.; Osikowicz, W.; Zotti, G.; van der Gon, A. W. D.; Louwet, F.; Fahlman, M.; Groenendaal, L.; De Schryver, F.; Salaneck, W. R. *Journal of Polymer Science Part B: Polymer Physics* **2003**, *41*, 2561–2583.

[284] de Jong, M. P.; van IJzendoorn, L. J.; de Voigt, M. J. A. *Applied Physics Letters* **2000**, *77*, 2255–2257.

[285] Turak, A. *RSC Advances* **2013**, *3*, 6188–6225.

[286] Jørgensen, M.; Krebs, F. C. *Stability and Degradation of Organic and Polymer Solar Cells*; John Wiley & Sons, Ltd, 2012; pp 143–162.

[287] Xia, Y.; Ouyang, J. *ACS Applied Materials & Interfaces* **2010**, *2*, 474–483.

[288] Luo, J.; Billep, D.; Waechtler, T.; Otto, T.; Toader, M.; Gordan, O.; Sheremet, E.;

Martin, J.; Hietschold, M.; Zahn, D. R. T.; Gessner, T. *Journal of Materials Chemistry A* **2013**, *1*, 7576–7583.

[289] Xia, Y.; Ouyang, J. *Journal of Materials Chemistry* **2011**, *21*, 4927–4936.

[290] Lee, I.; Kim, G. W.; Yang, M.; Kim, T.-S. *ACS Applied Materials & Interfaces* **2016**, *8*, 302–310.

[291] Scott, D. W. *Multivariate Density Estimation: Theory, Practice, and Visualization*, 1st ed.; Wiley: New York, 1992.

[292] Scott, D. W. *Biometrika* **1979**, *66*, 605–610.

[293] Luber, E. J.; Buriak, J. M. *ACS Nano* **2013**, *7*, 4708–4714.

[294] Anderson, T. W.; Darling, D. A. *The Annals of Mathematical Statistics* **1952**, *23*, 193–212.

[295] Oehzelt, M.; Akaike, K.; Koch, N.; Heimel, G. *Science Advances* **2015**, *1*, e1501127.

[296] Vaynzof, Y.; Kabra, D.; Zhao, L.; Chua, L. L.; Steiner, U.; Friend, R. H. *ACS Nano* **2011**, *5*, 329–336.

[297] Clark, M. D.; Jespersen, M. L.; Patel, R. J.; Leever, B. J. *ACS Applied Materials & Interfaces* **2013**, *5*, 4799–4807.

[298] Oh, J. Y.; Jang, W. S.; Lee, T. I.; Myoung, J.-M.; Baik, H. K. *Applied Physics Letters* **2011**, *98*, 023303.

[299] Xue, B.; Vaughan, B.; Poh, C.-H.; Burke, K. B.; Thomsen, L.; Stapleton, A.; Zhou, X.; Bryant, G. W.; Belcher, W.; Dastoor, P. C. *The Journal of Physical Chemistry C* **2010**, *114*, 15797–15805.

[300] Mauger, S. A.; Chang, L.; Friedrich, S.; Rochester, C. W.; Huang, D. M.; Wang, P.; Moulé, A. J. *Advanced Functional Materials* **2013**, *23*, 1935–1946.

[301] Wang, H.; Gomez, E. D.; Kim, J.; Guan, Z.; Jaye, C.; Fischer, D. A.; Kahn, A.; Loo, Y.-L. *Chemistry of Materials* **2011**, *23*, 2020–2023.

[302] *Interfacial Forces in Aqueous Media, Second Edition*, 2nd ed.; CRC Press: Boca Raton, Fla, 2006.

[303] Yang, D.; Guan, Z.; Yang, L.; Huang, Y.; Wei, Q.; Lu, Z.; Yu, J. *Solar Energy Materials and Solar Cells* **2012**, *105*, 220–228.

[304] He, Y.; Liu, C.; Li, J.; Zhang, X.; Li, Z.; Shen, L.; Guo, W.; Ruan, S. *ACS Applied Materials & Interfaces* **2015**, *7*, 15848–15854.

[305] Němcas, D.; Klapetek, P. *Central European Journal of Physics* **2012**, *10*, 181–188.

[306] Girifalco, L. A.; Good, R. J. *The Journal of Physical Chemistry* **1957**, *61*, 904–909.

[307] Wohlfarth, C. In *Surface Tension of Pure Liquids and Binary Liquid Mixtures:*, 2008th ed.; Lechner, M. D., Ed.; Springer, 2008.

[308] Aziz, F.; Ismail, A. F. *Materials Science in Semiconductor Processing* **2015**, *39*, 416–425.

[309] Wang, D.; Liu, F.; Yagihashi, N.; Nakaya, M.; Ferdous, S.; Liang, X.; Muramatsu, A.; Nakajima, K.; Russell, T. P. *Nano Letters* **2014**, *14*, 5727–5732.

[310] Proctor, C. M.; Kher, A. S.; Love, J. A.; Huang, Y.; Sharenko, A.; Bazan, G. C.; Nguyen, T.-Q. *Advanced Energy Materials* **2016**, *6*, 1502285.

[311] Deibel, C.; Baumann, A.; Dyakonov, V. *Applied Physics Letters* **2008**, *93*, 163303.

[312] Kaake, L. G.; Jasieniak, J. J.; Bakus, R. C.; Welch, G. C.; Moses, D.; Bazan, G. C.; Heeger, A. J. *Journal of the American Chemical Society* **2012**, *134*, 19828–19838.

[313] Olivier, Y.; Niedzialek, D.; Lemaur, V.; Pisula, W.; Müllen, K.; Koldemir, U.; Reynolds, J. R.; Lazzaroni, R.; Cornil, J.; Beljonne, D. *Advanced Materials* **2014**, *26*, 2119–2136.

[314] Proctor, C. M.; Love, J. A.; Nguyen, T.-Q. *Advanced Materials* **2014**, *26*, 5957–5961.

[315] Dou, L.; Gao, J.; Richard, E.; You, J.; Chen, C.-C.; Cha, K. C.; He, Y.; Li, G.; Yang, Y. *Journal of the American Chemical Society* **2012**, *134*, 10071–10079.

[316] Kim, M. J.; Choi, J. Y.; An, G.; Kim, H.; Kang, Y.; Kim, J. K.; Son, H. J.; Lee, J. H.; Cho, J. H.; Kim, B. *Dyes and Pigments* **2016**, *126*, 138–146.

[317] Chen, M. S.; Niskala, J. R.; Unruh, D. A.; Chu, C. K.; Lee, O. P.; Fréchet, J. M. J. *Chemistry of Materials* **2013**, *25*, 4088–4096.

[318] Nketia-Yawson, B.; Lee, H.-S.; Seo, D.; Yoon, Y.; Park, W.-T.; Kwak, K.; Son, H. J.; Kim, B.; Noh, Y.-Y. *Advanced Materials* **2015**, *27*, 3045–3052.

[319] Kumar, S. G.; Rao, K. S. R. K. *Rsc Advances* **2015**, *5*, 3306–3351.

[320] Mor, G. K.; Varghese, O. K.; Paulose, M.; Shankar, K.; Grimes, C. A. *Solar Energy Materials and Solar Cells* **2006**, *90*, 2011–2075.

[321] Noh, J. H.; Han, H. S.; Lee, S.; Kim, J. Y.; Hong, K. S.; Han, G.-S.; Shin, H.; Jung, H. S. *Advanced Energy Materials* **2011**, *1*, 829–835.

[322] Ray, B.; Khan, M.; Black, C.; Alam, M. *IEEE Journal of Photovoltaics* **2013**, *3*, 318–329.

[323] Chou, C.-H.; Chen, F.-C. *Nanoscale* **2014**, *6*, 8444–8458.

[324] Duong, D. T.; Ho, V.; Shang, Z.; Mollinger, S.; Mannsfeld, S. C.; Dacuña, J.; Toney, M. F.; Segalman, R.; Salleo, A. *Advanced Functional Materials* **2014**, *24*, 4515–4521.

[325] Liu, F.; Gu, Y.; Shen, X.; Ferdous, S.; Wang, H.-W.; Russell, T. P. *Progress in Polymer Science* **2013**, *38*, 1990–2052.

[326] Koch, F. P. V. et al. *Progress in Polymer Science* **2013**, *38*, 1978–1989.

[327] Mukherjee, S.; Proctor, C. M.; Tumbleston, J. R.; Bazan, G. C.; Nguyen, T.-Q.; Ade, H. *Advanced Materials* **2015**, *27*, 1105–1111.

[328] Viterisi, A.; Montcada, N. F.; Kumar, C. V.; Gispert-Guirado, F.; Martin, E.; Escudero, E.; Palomares, E. *Journal of Materials Chemistry A* **2014**, *2*, 3536–3542.

[329] Tumbleston, J. R.; Collins, B. A.; Yang, L.; Stuart, A. C.; Gann, E.; Ma, W.; You, W.; Ade, H. *Nature Photonics* **2014**, *8*, 385–391.

[330] Jung, M. et al. *ACS Nano* **2014**, *8*, 5988–6003.

[331] Yi, Z.; Ni, W.; Zhang, Q.; Li, M.; Kan, B.; Wan, X.; Chen, Y. *Journal of Materials Chemistry C* **2014**, *2*, 7247–7255.

[332] Hiszpanski, A. M.; Baur, R. M.; Kim, B.; Tremblay, N. J.; Nuckolls, C.; Woll, A. R.; Loo, Y.-L. *Journal of the American Chemical Society* **2014**, *136*, 15749–15756.

[333] Hazar Apaydın, D.; Esra Yıldız, D.; Cirpan, A.; Toppare, L. *Solar Energy Materials and Solar Cells* **2013**, *113*, 100–105.

[334] Chu, T.-Y.; Alem, S.; Verly, P. G.; Wakim, S.; Lu, J.; Tao, Y.; Beaupré, S.; Leclerc, M.;

Bélanger, F.; Désilets, D.; Rodman, S.; Waller, D.; Gaudiana, R. *Applied Physics Letters* **2009**, *95*, 063304.

[335] Clarke, T. M.; Peet, J.; Nattestad, A.; Drolet, N.; Dennler, G.; Lungenschmied, C.; Leclerc, M.; Mozer, A. J. *Organic Electronics* **2012**, *13*, 2639–2646.

[336] Duan, C.; Huang, F.; Cao, Y. *Polymer Chemistry* **2015**, *6*, 8081–8098.

[337] Hodes, G.; Kamat, P. V. *The Journal of Physical Chemistry Letters* **2015**, *6*, 4090–4092.

[338] Wang, T. Polymer Solar Cells Fabricated by Spray Coating in Air. International Photonics and OptoElectronics. 2015; p PT3D.6.

[339] Nie, W.; Coffin, R.; Liu, J.; MacNeill, C. M.; Li, Y.; Noftle, R. E.; Carroll, D. L.; Nie, W.; Coffin, R.; Liu, J.; MacNeill, C. M.; Li, Y.; Noftle, R. E.; Carroll, D. L. *International Journal of Photoenergy* **2012**, *2012*, e175610.

[340] Noebels, M.; Cross, R. E.; Evans, D. A.; Finlayson, C. E. *Journal of Materials Science* **2014**, *49*, 4279–4287.

[341] Girotto, C.; Rand, B. P.; Genoe, J.; Heremans, P. *Solar Energy Materials and Solar Cells* **2009**, *93*, 454–458.

[342] Chen, L.-M.; Hong, Z.; Kwan, W. L.; Lu, C.-H.; Lai, Y.-F.; Lei, B.; Liu, C.-P.; Yang, Y. *ACS nano* **2010**, *4*, 4744–4752.

[343] Abdellah, A.; Fabel, B.; Lugli, P.; Scarpa, G. *Organic Electronics* **2010**, *11*, 1031–1038.

[344] Hoth, C. N.; Steim, R.; Schilinsky, P.; Choulis, S. A.; Tedde, S. F.; Hayden, O.;

Brabec, C. J. *Organic Electronics* **2009**, *10*, 587–593.

[345] Susanna, G.; Salamandra, L.; Brown, T. M.; Di Carlo, A.; Brunetti, F.; Reale, A. *Solar Energy Materials and Solar Cells* **2011**, *95*, 1775–1778.

[346] Liu, K.; Larsen-Olsen, T. T.; Lin, Y.; Beliatis, M.; Bundgaard, E.; Jørgensen, M.; Krebs, F. C.; Zhan, X. *Journal of Materials Chemistry A* **2016**, *4*, 1044–1051.

[347] Jørgensen, M.; Norrman, K.; Krebs, F. C. *Solar Energy Materials and Solar Cells* **2008**, *92*, 686–714.

[348] Manceau, M.; Rivaton, A.; Gardette, J.-L. *Stability and Degradation of Organic and Polymer Solar Cells*; John Wiley & Sons, Ltd, 2012; pp 71–108.

[349] Choi, H.; Kim, B.; Ko, M. J.; Lee, D.-K.; Kim, H.; Kim, S. H.; Kim, K. *Organic Electronics* **2012**, *13*, 959–968.

[350] Schaffer, C. J.; Palumbiny, C. M.; Niedermeier, M. A.; Jendrzejewski, C.; Santoro, G.; Roth, S. V.; Müller-Buschbaum, P. *Advanced Materials (Deerfield Beach, Fla.)* **2013**, *25*, 6760–6764.

[351] Hee Kim, S.; Hwang, I.-W.; Jin, Y.; Song, S.; Moon, J.; Suh, H.; Lee, K. *Solar Energy Materials and Solar Cells* **2011**, *95*, 361–364.

[352] Manceau, M.; Bundgaard, E.; Carlé, J. E.; Hagemann, O.; Helgesen, M.; Søndergaard, R.; Jørgensen, M.; Krebs, F. C. *Journal of Materials Chemistry* **2011**, *21*, 4132–4141.

[353] Carlé, J. E.; Helgesen, M.; Madsen, M. V.; Bundgaard, E.; Krebs, F. C. *Journal of Materials Chemistry C* **2014**, *2*, 1290–1297.

[354] Ryu, T. I.; Yoon, Y.; Kim, J.-H.; Hwang, D.-H.; Ko, M. J.; Lee, D.-K.; Kim, J. Y.; Kim, H.; Park, N.-G.; Kim, B.; Son, H. J. *Macromolecules* **2014**, *47*, 6270–6280.

[355] Constantinou, I.; Lai, T.-H.; Zhao, D.; Klump, E. D.; Deininger, J. J.; Lo, C. K.; Reynolds, J. R.; So, F. *ACS Applied Materials & Interfaces* **2015**, *7*, 4826–4832.

[356] Yin, Z.; Zheng, Q.; Chen, S.-C.; Cai, D.; Ma, Y. *Advanced Energy Materials* **2016**, *6*, 1501493.

[357] Jayawardena, K. D. G. I. et al. *Nanoscale* **2015**, *7*, 14241–14247.

[358] Wang, J.; Lee, Y.-J.; Hsu, J. W. P. *The Journal of Physical Chemistry C* **2014**, *118*, 18417–18423.

[359] Wang, M.; Tang, Q.; An, J.; Xie, F.; Chen, J.; Zheng, S.; Wong, K. Y.; Miao, Q.; Xu, J. *ACS Applied Materials & Interfaces* **2010**, *2*, 2699–2702.

[360] Chen, L.; Du, D.; Sun, K.; Hou, J.; Ouyang, J. *ACS Applied Materials & Interfaces* **2014**, *6*, 22334–22342.

[361] Turkeli, S.; Kemp, R. *The political economy of research and innovation in organic photovoltaics (OPV) in different world regions*; 2014.

[362] Zervos, H.; Das, R.; Ghaffarzadeh, K. *Organic Photovoltaics (OPV) 2013-2023: Technologies, Markets, Players: IDTechEx*; 2012.

[363] *Next Generation OPV Technology Trend and Market Forecast*; 2015.

[364] *National Solar Technology Roadmap: Organic PV*; 2007.

[365] Amazing Technology Can Print a Solar Cell Every Two Seconds. http://inhabitat.com/

next-gen-technology-can-print-a-solar-cell-every-two-seconds/.

[366] Heliatek | organic based photovoltaics - solar active façades and lightweight structures. http://www.heliatek.com/en/applications/buildings.